1997

Interaction of acoustic beam with elastic structures

Han Zhang
Iowa State University

INFORMATION TO USERS

This manuscript has been reproduced from the microfilm master. UMI films the text directly from the original or copy submitted. Thus, some thesis and dissertation copies are in typewriter face, while others may be from any type of computer printer.

The quality of this reproduction is dependent upon the quality of the copy submitted. Broken or indistinct print, colored or poor quality illustrations and photographs, print bleedthrough, substandard margins, and improper alignment can adversely affect reproduction.

In the unlikely event that the author did not send UMI a complete manuscript and there are missing pages, these will be noted. Also, if unauthorized copyright material had to be removed, a note will indicate the deletion.

Oversize materials (e.g., maps, drawings, charts) are reproduced by sectioning the original, beginning at the upper left-hand corner and continuing from left to right in equal sections with small overlaps. Each original is also photographed in one exposure and is included in reduced form at the back of the book.

Photographs included in the original manuscript have been reproduced xerographically in this copy. Higher quality 6" x 9" black and white photographic prints are available for any photographs or illustrations appearing in this copy for an additional charge. Contact UMI directly to order.

UMI

A Bell & Howell Information Company
300 North Zeeb Road, Ann Arbor MI 48106-1346 USA
313/761-4700 800/521-0600

Interaction of acoustic beam with elastic structures

by

Han Zhang

A dissertation submitted to the graduate faculty

in partial fulfillment of the requirements for the degree of

DOCTOR OF PHILOSOPHY

Major: Engineering Mechanics

Major Professor: Dale E. Chimenti

Iowa State University

Ames, Iowa

1997

Graduate College
Iowa State University

This is to certify that the Doctoral dissertation of

Han Zhang

has met the dissertation requirements of Iowa State University

Signature was redacted for privacy.

Committee Member

Signature was redacted for privacy.

Committee Member

Signature was redacted for privacy.

Committee Member

Signature was redacted for privacy.

Committee Member

Signature was redacted for privacy.

Major Professor

Signature was redacted for privacy.

For the Major Program

Signature was redacted for privacy.

For the Graduate College

TABLE OF CONTENTS

LIST OF TABLES

LIST OF FIGURES

GENERAL INTRODUCTION

Modeling of the interaction of finite acoustic beams with elastic structures is important in ultrasonic NDE for two reasons: one, because beams are so often employed in routine NDE measurements, and two, because the effect of the finite beam can be as large as, or larger than, intrinsic material effects. This dissertation is aimed at meeting this need. When a finite acoustic beam is incident on an elastic structure, interesting phenomena occur. A simple and attractive mathematical description of a finite acoustic beam is the Gaussian profile, because the beam it is in some respects close to that of a real transducer. But there are important differences between real piston fields and Gaussian beams that we discuss below. The convenient mathematical properties of the Gaussian beam have made it a popular idealization in the acoustical literature of the past 25 years. Moreover, Gaussian beams can be constructed mathematically by simple artifice.

Finite Acoustic Beams

When the central ray of an incident finite beam is at, or near, the phase-match angle of a structure-borne wave mode, an anomalous reflection occurs. Such a topic has been an active research area over the past 40 years. Schoch predicted in 1950 [1] and verified [2] in 1952 that the reflected beam is displaced laterally from the position prescribed by geometrical acoustics on a liquid-solid interface. Later experiments [3] observed more phenomena than just a simple beam shift: there is also a null region in the reflected

beam which is not present in the incident beam. Furthermore, the main portion of the reflected beam is accompanied by a sound field that extends along the interface far from the point of incidence. This phenomenon is called the "trailing field".

Schoch's original theory, based on a Fresnel approximation, could not explain all the observed phenomena, so in 1973 Bertoni and Tamir [4] presented a unified theory of nonspecular reflection that accurately describes all observations. In their model they assume a finite well collimated incident Gaussian beam, and they decompose it into a wavenumber spectrum of plane waves. The reflected field is then synthesized from the wavenumber (or angular) spectrum multiplied by the halfspace plane-wave reflection coefficient. Their results show that the reflected field consists of two parts: a geometrically reflected field (the specular reflection) and a decaying leaky wave field excited by the incident beam. The leaky wave reradiates into the surrounding medium as it propagates along the interface. The interference of the specular reflection and the reradiated leaky wave lead to a null region near the point of incidence. The theoretical frame work of Bertoni and Tamir was extended to immersed plates by Pitts *et al.* [5] and was later employed to explain similar effects in plate-like structures [6] and in layered halfspaces [7].

In 1980 Ngoc [8] used numerical integration of the spectral integrals to study the effects of the incident beam width, incident angle and the characteristic mode of the plate on the nonspecular reflection. Claeys and Leroy [9] took the approach of building the incident bounded beam with inhomogeneous waves and derived an analytical expression for reflected and transmitted field in 1982. Norris [10] studied geometric backscattering during the finite beam incidence by modifying the reflection integral used by Bertoni and Tamir to include the backward-traveling leaky Rayleigh-wave pole in 1983. Pott and Harris [11] studied all effects observed so far during critical angle incidence by constructing the incident Gaussian beam with a complex source point. They also calculated the beam field inside the solid. Schmidt and Jensen [12] also employed a purely

numerical. but full-field. method to calculate the incident and reflected fields and their superposition in the fluid and in multilayered solids in 1985.

Rousseau and Gatignol presented a short-wave asymptotic analysis to calculate the reflected fields from a halfspace in 1985 [13] and from a plate in 1986 [14]: these too were not restricted to the fluid-solid interface. A purely numerical method was employed by Kundu [15] to study bounded beam reflection effects on several different layered structures. especially the case where the bottom surface of the solid is traction-free. This case was also studied using asymptotic analysis by Chimenti and Nayfeh [16]. So far. all the work cited is limited to interaction of the highly collimated Gaussian beams with plane structures. Zeroug and Felson [17. 18] and Chimenti. *et al.* [19] extended the interaction of diverging Gaussian beams with planar structures and collimated Gaussian beams with cylindrical structures. both theoretically and experimentally. They found that similar nonspecular reflection effects occur on curved structures and that the interaction of collimated Gaussian beams with curved structures is analogous to the interaction of diverging Gaussian beams with planar structures.

In the experimental arena most early studies of bounded beam reflection is carried out using Schlieren visualization methods [2. 3]. Chimenti *et al.*[19] used transducers to detect the reflected field in a pitch-catch setup. This arrangement certainly is a better approach from the NDE point. In fact. the reflected beam measurement has remained important and continues to attract attention in NDE because the reflected beam carries critical elastic property information.

The study of bounded beam reflection is not limited to the phenomenology of nonspecular reflection. In addition, it is widely used to assess the quality of elastic structures and to invert data to infer elastic properties. especially for composites. This issue is well addressed by Chimenti and Nayfeh [20]–[24] in a series of papers on bounded beam reflection measurements from composite materials. Significant contributions have also been made by Rokhlin [25] and by Mal [26]. The reader can find more detail in a recent

review paper by Chimenti [27]. Strictly speaking, in such a beam reflection measurement, what we measure is not the reflected field, because of the finite aperture of the receiver: instead we obtain the receiver voltage, which is modeled by a further integration of the reflected field over the aperture of the receiver. We take up this point again below.

Gaussian Beams and Complex Source Points

The choice of the simple Gaussian function to replace the Bessel function of a real piston radiator is mathematically attractive, as noted above. In fact, however, there exists an even simpler method to construct Gaussian beams, by using the so-called complex source point. It originates from an observation made by Deschamps [28]. He noted that if complex values are assigned to the coordinates of a monopole source, the resulting wavefield is, in the paraxial approximation, a Gaussian beam. Unlike the Gaussian beam field, however, which is only an approximate solution of the field equations that fails outside the paraxial region surrounding the beam axis, the complex-source-point field yields a valid solution of the field equations at arbitrary observation point. By displacing the real point source into the complex plane in the presence of a scatterer, one converts an incident spherical wave (three-dimensional case) or cylindrical wave (two-dimensional case) into a rotationally symmetric Gaussian beam or Gaussian sheet beam.

This is exactly the approach used by Ra *et al.* [29] to calculate the scattering of a two-dimensional electromagnetic Gaussian beam from a dielectric interface. They first assume an incident cylindrical wave and use plane-wave spectral methods to convert the cylindrical wave into a Gaussian sheet beam. The same approach is used by Norris [10], Pott [11] and Zeroug [17, 18] to calculate the reflected field of an incident Gaussian beam. The essence of the complex source point is that it is an analytic continuation

of an existing Green's function solution for application in solving beam problems. This approach is especially convenient for the study the reflection and diffraction of Gaussian beams because the reflection and diffraction of spherical waves is solved in detail in classic acoustics books. such as the monograph by Brekhovskikh [30] and the review paper by Felsen [31]. We can obtain the field of a dissipative medium from the field of a non-dissipative medium through an analytic continuation procedure by simply allowing the constitutive equation to be complex. We also note that the Gaussian beam is used to analyze the optical mode in the laser resonator cavities and in light waveguides [32]. where a complex radius of curvature is used to describe the propagation of Gaussian beams. similar to the same idea of a the complex source point. In fact both the complex source point and the complex radius of curvature give the same results.

For ultrasonic experiments the reflected field is detected by the receiver. The fact that the receiver has a finite aperture invalidates the simple CSP field calculation. as we have already discussed. The generalization to a finite receiver can be easily accomplished. however. by a similar procedure [33]. We displace the real observation point into the complex plane: the result may be called a complex receiver point . Then. exploiting reciprocal theorems of Kino [34] and Auld [35]. one can construct an expression in which the diffraction effects of both transducers are properly accounted for [33]. The result is an exact representation of the voltage of a sending probe as measured by a receiving probe. The combination of the complex source and receiver points has been termed the "complex transducer point" (CTP). Recently, in an extension of the study cited above [19]. Lobkis. *et al.* [36] have demonstrated that although a piston field is very different from a Gaussian beam. particularly in the near field. the voltage integral over the combined directivity functions of two Gaussians is almost identical to the sum over a product of piston radiator Bessel functions. This valuable result permits the well justified replacement of the complicated piston with the simple Gaussian functions and supports the validity of the subsequent asymptotic analysis.

In real experiments and in the calculation the imaginary part of the complex transducer point determines the width and divergence of the Gaussian beam. A small imaginary part yields a highly diverging beam, where a larger imaginary source point gives a collimated Gaussian beam. In Chapters 3 and 4 of this thesis is contained a further development of the complex transducer point and its application to real reflected and transmitted beam measurement and related NDE tasks.

Four problems are addressed in this work, and they can be separated into two categories. One is the Gaussian beam at a single frequency, the other studies the Gaussian beam characteristics when the frequency varies and is applied to the receiver voltage spectrum measurement. The central issues are materials characterization and component quality assessment.

Narrowband Gaussian beams are employed first to study ultrasonic reflection from layered cylinders, in this case a sheet of rubber bonded to the surface of a steel shell. A Gaussian sheet beam (2-D) is constructed by displacing the source and observation points into the complex plane, as in the two-dimensional case mentioned earlier. This problem poses new challenges because, for one thing, the rubber has a very high material damping; we study the influence of rubber damping on the leaky wave and on the total reflected field. Second, we also study the influence of bond rigidity on the leaky wave and on the received signal. The reflected signal carries information to evaluate the bond rigidity between rubber and steel.

Narrowband Gaussian beams are then applied to the study of transducer misalignment effects in beam reflection measurements. "Misalignment" means that the receiver angle is slightly different from transmitter incident angle. In most ultrasonic pitch-catch inspection setups, transmitter incident angle is equal to the receiver incident angle in order to detect the reflected signal efficiently. Here, we evaluate quantitatively the effect resulting from the misalignment with the aid of the complex transducer point. The analysis performed here is very important for precise materials characterization. Here,

too. the Gaussian sheet beam is constructed from incident cylinder wave functions.

The third narrowband Gaussian beam analysis in this dissertation is used to reconstruct the air-coupled ultrasound transmission coefficient and to invert the data to obtain material constants. First. the analysis of reflection case is extended to transmission. Second. the previously measured spatial field distribution in the reflected field is processed further. We perform a spatial Fourier transform on the result of a coordinate scan with the receiver. The transform permits us to extract information on a particular Lamb mode. The sum of such transforms on data at many incident angles is a close approximation to the plane-wave transmission coefficient. Here. both the rotationally symmetric Gaussian beam and the Gaussian sheet beam are used and compared. We find that the reconstructed transmission coefficient is different for the 2-D or 3-D treatments.

The narrowband experiments and analysis are extended in the final part of this dissertation to study wideband spectral features of the reflected signal. By assuming a linear frequency dependence on the Fresnel length for Gaussian beams the previous narrowband results can be applied to calculate the frequency spectrum of the wideband receiver signal without any fundamental change. Only the computational strategy is a bit different. As in the case of the third problem. both the rotationally symmetric Gaussian beam and the 2-D sheet beam are used here. The difference between the 2-D and 3-D beams over a broad frequency spectrum are compared.

Dissertation Organization

The dissertation consists of four main chapters. preceded by a general introduction and followed by a general conclusion: it includes two appendices. The four problems discussed above form the four main chapters of the dissertation and are related by the common theme of ultrasonic wave propagation in finite structures and wave mode conversion between guided and bulk acoustic waves.

The first chapter deals with the reflection of acoustic beams from rubber-coated cylindrical steel shells and the detection of disbond defects at the rubber-steel interface. Preliminary results from this work have been reported in the *Review of Progress in Quantitative of Nondestructive Evaluation* . Vol 16A. 91-98 (1997). A full-length journal article based on these findings and analysis has been accepted for publication in the journal Ultrasonics.

The second chapter reports analysis and measurements of the effects of transducer misalignment on leaky wave experiments: this delicate effect could only be resolved with improved measurement methods and accurate transducer positioning. Preliminary results of these studies have also been reported at the *Review of Progress in QNDE* in the summer of 1997 and will appear in the corresponding proceedings to be published in 1998. An extended journal article on this topic has been submitted to Journal of the Acoustic Society of America. where it is currently under review.

The third chapter applies the CTP to the air-coupled ultrasonic geometry and discusses the reconstruction of the acoustic transmission coefficient from air-coupled ultrasonic measurements and the subsequent inversion of material elastic stiffnesses. The fourth chapter is principally analytical in nature and extends the CTP formalism to the leaky wave reflection frequency spectrum. including related material characterization issues. In addition. original experimental results are reported and compared to the analysis.

The first two chapters stand as they were originally submitted for publication. Additional results are included in Appendices A and B. Appendix A provides the transfer matrix which is used to calculate the reflection coefficient of multilayers in the first chapter and includes further experimental results. especially in the time domain. Appendix B presents the calculation of the saddle point and pole. which is extremely useful for understanding the development in Chapter 2.

References

[1] A. Schoch. "Schallreflexion. Schallbrechung and Schallbeugung. [Sound reflection. refraction. and bending]". Ergeb. Exakten Naturwiss.. **23** 127–234 (1950).

[2] A. Schoch. "Der Schalldurchgang and Schallbeugung [Sound transmisson through plates]". Acustica. **2**. 1-18 (1952).

[3] W. G. Neubauer. "Ultrasonic reflection of a bounded beam at Rayleigh and critical angles for a plane liquid-solid interface". J. Appl. Phys.. **44**. 48-55 (1973).

[4] H. L. Bertoni and T. Tamir. "Unified theory of Rayleigh-angle phenomena for acoustic beams at liquid-solid interfaces." Appl. Phys. (1973) **2** 157–172.

[5] L. E. Pitts. T. J. Plona and W. G. Mayer. "Theory of nonspecular reflection effects for an ultrasonic beam incident on a solid plate in a liquid. IEEE Trans. Sonics Ultrason.. **SU-24** 101–9 (1977).

[6] T. J. Plona. L. E. Pitts and W. G. Mayer. "Ultrasonic bounded beam reflection and transmission effects at a liquid/solid-plate/liquid interface." J. Acoust. Soc. Am. (1976) **59** 1324–1329.

[7] D. E. Chimenti and A. H. Nayfeh. "Leaky Rayleigh waves on a layered halfspace". J. Appl. Phys. **53**. 170–76 (1982).

[8] T. K. Ngoc and W. G. Mayer. "A general description of ultrasonic nonspecular reflection and transmission effects for layered media." IEEE Trans. Sonics Ultrason., **SU-24** 101–9 (1977).

[9] J. M. Claeys and O. Leroy. "Reflection and transmission of bounded beams on half-spaces and through plates." J. Acoust. Soc. Am. **72** 585–590(1982).

[10] A. N. Norris. "Back reflection of ultrasonic waves from a liquid-solid interface." J. Acoust. Soc. Am., **73** 427–434(1983).

[11] J. Pott and J. G. Harris. "Scattering of an acoustic Gaussian beam from a fluid-solid interface." J. Acoust. Soc. Am., **76** 427–434 (1983).

[12] H. Schmidt and F. B. Jensen. "A full wave solution for propagation in multi layered viscoelastic media with application to Gaussian beam reflection at fluid-solid interfaces."J. Acoust. Soc. Am., **77** 813–825(1985) .

[13] M. Rousseau and Ph. Gatignol. "Short wave analysis for the reflection of bounded acoustic beams onto liquid-solid interface at the Rayleigh incidence."J. Acoust. Soc. Am., **78** 1859–1867 (1985).

[14] M. Rousseau and Ph. Gatignol."Asymptotic analysis of nonspecular effects for the reflection and the transmission of a Gaussian acoustic beam incident on a solid plate."J. Acoust. Soc. Am., **80** 325–332 (1986) .

[15] T. Kundu. "On the nonspecular reflection of bounded acoustic beams."J. Acoust. Soc. Am., **83** 18–24 (1988).

[16] D. E. Chimenti and A. H. Nayfeh. "Ultrasonic leaky waves in a solid plate separating a fluid and vacuum". J. Acoust. Soc. Am., **85** 555–60 (1988).

[17] S. Zeroug and L. B. Felsen. Nonspecular reflection of two- and three-dimensional acoustic beams from fluid-immersed plane-layered elastic structures. J. Acoust. Soc. Am. (1994) **95** 3075–98.

[18] S. Zeroug and L. B. Felsen. Nonspecular reflection of two- and three-dimensional acoustic beams from fluid-immersed cylindrically layered elastic structures. J. Acoust. Soc. Am. (1995) **98** 584–98.

[19] D. E. Chimenti. J. Zhang. S. Zeroug. and L. B. Felsen. Interaction of acoustic beams with fluid-loaded elastic structures. J. Acoust. Soc. Am. (1994) **95** 45–59.

[20] D. E. Chimenti. A. H. Nayfeh. "Leaky Lamb waves in fibrous composite laminates."J. Acoust. Soc. Am.. **58** 4531–8 (1985).

[21] A. H. Nayfeh. D. E. Chimenti. "Propagation of guided waves in fluid-coupled plates of fiber-reinforced composite." J. Acoust. Soc. Am.. **58** 1736–43 (1988).

[22] A. H. Nayfeh. D. E. Chimenti. "Ultrasonic wave reflection from liquid-coupled orthotropic plates with application to fibrous composites." J. Appl. Mech. .**55**. 863-70 (1988).

[23] D. E. Chimenti. A. H. Nayfeh. "Ultrasonic reflection and guided wave propagation in biaxially laminated composite plates."J. Acoust. Soc. Am.. **87** 1409–15 (1990).

[24] A. H. Nayfeh and D. E. Chimenti. "Ultrasonic reflection and guided wave propagation in biaxially laminated composite plates." J. Acoust. Soc. Am.. **89** 542–9 (1991).

[25] S. I. Rokhlin and D. E. Chimenti. "Reconstruction of elastic constants from ultrasonic reflectivity data in a fluid coupled composite plate". *Review of Progress in Quantitative NDE*. **9**. Eds. D. O. Thompson and D. E. Chimenti. (Plenum. New York. 1990). 1411-1418.

[26] M. R. Karim and A. K. Mal. "Inversion of leaky Lamb wave by simplex algorithm". J. Acoust. Soc. Am. **88**. 482–491 (1990).

[27] D. E. Chimenti. "Guided waves in plates and their use in materials characterization." Appl. Mech. Rev. **50**. 247-284 (1997).

[28] G. A. Deschamps. "Gaussian beam as a bundle of complex rays". Electron. Lett. (1971) **7** 684–85.

[29] J. W. Ra. H. L. Bertoni and L. B. Felsen. "Reflection and transmission of beams at a dielectric field."SIAM J. Appl. Math. .**24**. 396-413(1973).

[30] L.M.Brekhovskikh. *Waves in Layered Media*(Academic. New York. 1960). Chapt 4.

[31] L. B. Felsen. "Complex source point solutions of the field equations and their relation to the propagation and scattering of Gaussian beams." Symp. Math. .**18**. 39-56 (1976).

[32] A. E. Siegman. *An introduction to lasers and masers*. McGraw-Hill. New York. Page 304. 1971.

[33] S. Zeroug. F. E. Stanke. and R. Burridge. "A complex-transducer-point model for emitting and receiving ultrasonic transducers." Wave Motion **24** (1996). 21-40.

[34] G. S. Kino. "The application of reciprocal theory to scattering of acoustic waves by flews."J. Appl. Phys..**49**. 3190-99(1978).

[35] B. A. Auld. General electro mechanical reciprocity relations applied to the calculation of elastic wave scattering coefficients. Wave Motion (1979) **1** 3–10.

[36] O. I. Lobkis. A. Safaeinili. D. E. Chimenti. "Precision ultrasonic reflection studies in fluid-coupled plates". J. Acoust. Soc. Am. **99**. 2727–2736 (1996).

CHAPTER 1 ULTRASONIC BEAM REFLECTION FROM LOSSY LAYERED CYLINDRICAL SHELLS

A paper accepted for publication in the Journal of Ultrasonics

Han Zhang and Dale E. Chimenti

Abstract

Nonspecular reflection from a two-layer curved elastic structure consisting of rubber bonded to the outer surface of a steel shell has been studied experimentally and theoretically. The reflected field, in a two-transducer experiment, is measured as a function of azimuthal scan angle. The bond rigidity between the rubber and steel is accounted for by a spring model. This model is incorporated into an asymptotic evaluation of the spectral reflection integrals, accounting for the receiver characteristics by electromechanical reciprocity. Decreasing bond rigidity acts to weaken the leaky wave excited in the underlying steel shell and provides a method to assess bond integrity, while the damping loss of the rubber is found to be only a scale factor. A disbond completely suppresses the leaky wave. In comparisons between experimental data and predictions, good agreement is generally seen, also at incident angles different from phase-matched Lamb mode coupling.

PACS Codes: 43.20Fn, 43.20Mv, 43.30Dr, 43.35Zc

Keywords: Nonspecular reflection; cylinders; guided waves; damping

Introduction

Investigations of nonspecular ultrasonic reflection have been pursued since Schoch [1] and Bertoni and Tamir [2] gave an accurate description of collimated beam reflection from a halfspace at the Rayleigh critical angle. Later research concentrated on effects at planar surfaces [3]–[5]. Our previous studies, which contain extensive reviews of the literature, extended this analysis to the case of divergent Gaussian beams interacting with planar structures (halfspace and plate) and well collimated beams interacting with curved structures (solid cylinders and shells) [6, 7].

In this article we consider two-layer, lossy cylindrical shells, namely, rubber and steel bonded together. The reflection from lossy halfspaces has been studied experimentally by Becker [8] for low-loss materials, and theoretically by Bertoni and Tamir [2]. In our case, rubber is very lossy, and its virtually perfect acoustic impedance match to water means that it cannot support leaky guided waves when water-loaded. However, when it is bonded to a steel shell, we find the leaky guided wave in steel can still be excited. The coherent sum of the specular and non-specular components produces characteristic oscillations in the receiver signal as a function of scan angle: in debond regions the leaky guided modes are not excited, and the oscillatory part of the received signal is suppressed. Extensive experimental results in this paper show that the reflected field from the bond region of rubber-steel is similar to that from a single steel shell under the same experimental conditions, with the exception of the amplitude of the received signal. In this paper we study the effects of bond rigidity, the damping of rubber and the incident angle deviation from the phase-matched Lamb mode angle on the leaky wave. In the following section, we will briefly review the complex transducer point approach to beam generation and the asymptotic evaluation of the spectral integrals used to calculate the transducer voltage. Primary emphasis is placed on the discussion of the reflection coefficient and on the analysis of the experimental results.

Theoretical Summary

Nonspecular reflection can be well accounted for by asymptotic evaluation of the spectral integrals, using the complex source point (CSP) formalism to generate Gaussian sheet beams [9]–[11]. By this method, a simple line source field can be converted into a two-dimensional Gaussian beam field by an analytic continuation of the real source coordinate into the complex plane.

$$\tilde{x}' = x' + ib\sin\alpha': \quad \tilde{y}' = y' + ib\cos\alpha': \tag{1.1}$$

$$\tilde{r}' = \sqrt{\tilde{x}'^2 + \tilde{y}'^2}, \quad \tilde{\phi}' = \tan^{-1}\left(\frac{\tilde{x}'}{\tilde{y}'}\right): \tag{1.2}$$

where x', y' are the transmitter real coordinates, $\tilde{x}', \tilde{y}'$ are complex coordinates, α' is the launch angle of the transmitter (see Fig. 1.1), and b is the transducer's Fresnel length, related to the beam width at its waist by $w = \sqrt{2b/k_f}$. Using reciprocity [12], this method is also extended to account for the finite receiver aperture by a similar manipulation of the receiver coordinates [13]. In a two-transducer experiment the combination has been referred to as the complex transducer point (CTP) method [13], which yields a result directly comparable to experiment.

With the aid of electromechanical reciprocity, we find for the receiver voltage integral [10, 13],

$$\begin{aligned} V_R(\tilde{r}; \tilde{r}') &= \frac{-1}{16\pi} \mathcal{J}(\omega)\omega\rho_f A_T A_R \int_{-\infty}^{+\infty} R(\nu) \frac{H_\nu^{(2)}(k_f a)}{H_\nu^{(1)}(k_f a)} \\ &\quad \times H_\nu^{(1)}(k_f \tilde{r}') H_\nu^{(1)}(k_f \tilde{r}) \exp\left\{i\nu\left[\tilde{\phi} - \tilde{\phi}'\right]\right\} d\nu, \end{aligned} \tag{1.3}$$

where R is the reflection coefficient (RC), ν is the angular spectral wavenumber, ω is the angular frequency, A_T and A_R represent the strength of the transmitter and receiver areas, a is the shell radius, $H_\nu^{(n)}$ is the nth-order Hankel function; the term $\mathcal{J}(\omega)$ is a frequency response spectrum of the transducers and associated electronics.

To evaluate this integral the Hankel functions are approximated by their Debye decompositions, the integration parameter ν is generalized to a complex variable $\tilde{\nu}$, and

the integration path along the real ν axis is deformed into a steepest descent contour. The integral is then evaluated at the saddle point. The integration along the steepest descent contour must be augmented with the contributions from the reflection coefficient poles intercepted by the deformed contour [14]. The result of this analysis is a uniform asymptotic expression for the voltage.

$$\begin{aligned} V_{\mathcal{R}}(\underline{\tilde{r}};\underline{\tilde{r}}') \sim\ & \frac{i}{2\pi}\mathcal{J}(\omega)\omega\rho_f A_{\mathcal{T}} A_{\mathcal{R}} \\ & \times R(\nu_s)\frac{\exp\{i\pi/4\}}{2\sqrt{2\pi}}\frac{\exp\left\{ik_f\left(\tilde{L}'+\tilde{L}\right)\right\}}{\sqrt{k_f\left(\tilde{L}'+\tilde{L}\right)}}\sqrt{\left.\frac{a\left(\tilde{L}'+\tilde{L}\right)\sin\gamma_a}{2\tilde{L}'\tilde{L}+a\left(\tilde{L}'+\tilde{L}\right)\sin\gamma_a}\right|_{\tilde{\nu}_s}} \\ & -\frac{1}{2}\sum_{j=1}^{M}\frac{\mathrm{Res}\left\{R(\nu_{p_j})\right\}}{k_f(r\tilde{r}'\sin\gamma\sin\tilde{\gamma}'|_{\nu_{p_j}})^{1/2}}\exp\left\{i\tilde{P}^r(\nu_{p_j})\right\}\tau(-i\tilde{s}_{p_j}). \end{aligned} \tag{1.4}$$

where

$$\tilde{P}^r(\nu) = k_f\left(\tilde{r}\sin\gamma+\tilde{r}'\sin\tilde{\gamma}'-2a\sin\gamma_a\right)-\nu\left(\gamma+\tilde{\gamma}'-2\gamma_a-\left[\tilde{\phi}-\tilde{\phi}'\right]\right) \tag{1.5}$$

$$\tilde{L}' = \tilde{r}'\sin\tilde{\gamma}'-a\sin\gamma_a|_{\tilde{\nu}_s} \qquad \tilde{L}=\tilde{r}\sin\gamma-a\sin\gamma_a|_{\tilde{\nu}_s}. \tag{1.6}$$

and

$$\gamma=\cos^{-1}\left(\frac{\nu}{k_f\tilde{r}}\right), \quad \tilde{\gamma}'=\cos^{-1}\left(\frac{\nu}{k_f\tilde{r}'}\right), \quad \gamma_a=\cos^{-1}\left(\frac{\nu}{k_f a}\right). \tag{1.7}$$

Here, τ is the transition function, $\tilde{\nu}_{p_j}$ is the jth RC pole, and $\tilde{\nu}_s$ is the saddle point. A more complete description of the analysis can be found in [10].

Reflection Coefficient

The conventional boundary conditions for the interface of two solids are welded and slip boundary conditions. The welded boundary condition is an idealization of perfect bonding of structures. All dissimilar real materials deviate from this idealization in some way. One widely used description of imperfect boundary conditions is the spring model [15]-[18], which allows for displacement discontinuities. The continuity of stress and its linearity with the displacement jump are based on the assumption that vibrations are

instantaneously transferred from one medium to another (neglecting inertia) and that the amplitude of the displacement is very small compared to the wavelength. Interface inertia effects are introduced in [15]. As demonstrated by Rokhlin and Wang [18], however, the interface inertia effects can be neglected if the interface is a soft layer, which is the case treated here. Therefore, in the following we will use the spring model to describe the bond rigidity between the rubber and steel, and we will apply the transfer matrix to calculate the reflection coefficient of the whole layered structure.

Transfer Matrices

As a result of multiple wave reflections from the boundary, a system of longitudinal and transverse waves will exist in the layer, where the waves in the layer can be described by a displacement potential.

$$\phi = A_l^+ e^{i(kx+\kappa_l z)} + A_l^- e^{i(kx-\kappa_l z)} \tag{1.8}$$

$$\psi = A_t^+ e^{i(kx+\kappa_t z)} + A_t^- e^{i(kx-\kappa_t z)}. \tag{1.9}$$

where $k_l = \omega/c_l$ and $k_t = \omega/c_t$, with c_l and c_t the longitudinal and transverse wave speeds. Then, $\kappa_l^2 = k_l^2 - k^2$ and $\kappa_t^2 = k_t^2 - k^2$ are the longitudinal and transverse wavevector components in the z direction. The superscript $^+$ refers to waves that propagate in the positive z direction, and $^-$ refers to the opposite. The displacements and stresses are then calculated from gradients of displacement potentials and the linear constitutive relation.

Eventually, we obtain a relation between the displacement-stress vector $\{b_i^-\}$ and $\{b_i^+\}$ at the lower and upper interface of the layer.

$$\{b_i^+\} = [C_{ij}]\{b_j^-\}. \tag{1.10}$$

where

$$[C_{ij}] = [D_{ij}^+][D_{ij}^-]^{-1}. \tag{1.11}$$

Equation (1.10) forms the basic unit for transferring displacement and stress from the upper to the lower interface for each layer. A more complete derivation of this formalism can be found in [17]: here, we use displacement potential and express transfer matrices as a function of wavevector k in order to incorporate the result into our voltage calculation.

Spring Model

The sample geometry used in our experiments is shown in Fig. 1.2: we deal with a four-layer structure where layer 1 is steel, layer 2 is rubber, media 0 and 3 are both water and are infinite in extent. From Eq. (1.10) $\{b_i^{+(n)}\}$ at the upper interface of layer $n(n = 1, 2)$ is related to the displacement-stress vector $\{b_i^{-n}\}$ at the lower interface of layer n by

$$\{b_i^{+(n)}\} = [C_{ij}^{(n)}]\{b_j^{-(n)}\} \qquad n = 1, 2. \tag{1.12}$$

The boundary rigidity between layer 2 and layer 1 can be accounted for by the spring model mentioned above. When the inertia effects of the interface are neglected, the traction at the interface is continuous. The linear relation between the stress and the displacement can be written as [17, 18].

$$\sigma_{xz}^{-(2)} = \sigma_{xz}^{+(1)} = \sigma_{xz}, \qquad \sigma_{zz}^{-(2)} = \sigma_{zz}^{+(1)} = \sigma_{zz}. \tag{1.13}$$

$$\sigma_{xz} = kkt * (u^{-(1)} - u^{+(2)}), \qquad \sigma_{zz} = kkn * (w^{-(1)} - w^{+(2)}), \tag{1.14}$$

where kkt and kkn are the tangential and normal boundary stiffness constants. As kkt and kkn increase, so does the boundary rigidity. By using Eqs. (1.13) and (1.14) we can relate $\{b_i^{(-2)}\}$ to $\{b_i^{(+1)}\}$ through

$$\{b_i^{-(2)}\} = [K_{ij}]\{b_j^{+(1)}\} \tag{1.15}$$

where $[K_{ij}]$ is a matrix defined by

$$K = \begin{bmatrix} 1 & 0 & kkt^{-1} & 0 \\ 0 & 1 & 0 & kkn^{-1} \\ 0 & 0 & 1 & 0 \\ 0 & 0 & 0 & 1 \end{bmatrix}. \tag{1.16}$$

Combining Eqs. (1.12) and (1.15), we obtain a relation between $\{b_i^{+(2)}\}$ of the upper interface of layer 2 and $\{b_i^{-(1)}\}$ of the lower interface of layer 1.

$$\{b_i^{+(2)}\} = [\Gamma_{ij}]\{b_j^{-(1)}\}. \tag{1.17}$$

where $[\Gamma_{ij}] = [C_{im}^{(2)}][K_{mn}][C_{nj}^{(1)}]$. Now, $\{b_i^{+(2)}\}$ and $\{b_i^{-(1)}\}$ can be further related to the pressure and displacement at the upper and lower liquid/solid interfaces by the continuity of normal displacements and surface tractions.

$$\begin{aligned} w^{+(2),-(1)} &= w^{(3),(0)}|_{z=0,d_1+d_2} \\ \sigma_{zz}^{+(2),-(1)} &= p^{(3),(0)}|_{z=0,d_1+d_2} \\ \sigma_{xz}^{+(2),-(1)}|_{z=0,d_1+d_2} &= 0. \end{aligned} \tag{1.18}$$

where $w^{(0),(3)}$ and $p^{(0),(3)}$ are the normal displacements and excess pressure in the lower liquid medium 0 and upper liquid medium 3.

Denoting the velocity and density of upper liquid medium 3 as $c_f^{(3)}$ and $\rho_f^{(3)}$ and those of the lower liquid medium 0 as $c_f^{(0)}$ and $\rho_f^{(0)}$, then the displacement potentials in medium 0 and medium 3 can be given as $o^{(0)} = Te^{i(kx+\kappa_f^{(0)}z)}$ and $o^{(3)} = e^{i(kx+\kappa_f^{(3)}z)} + Re^{i(kx-\kappa_f^{(3)}z)}$, where $k_f^{(0),(3)} = \omega/c_f^{(0),(3)}$ are the wavevectors in liquid media 0 and 3. Then, $\kappa_{f(0),(3)}^2 = k_{f(0),(3)}^2 - k^2$ are the corresponding wavevector components in the z direction. R is the desired reflection coefficient, and T is the transmission coefficient. ¿From the potential relation for $o^{(3)}$ and $o^{(0)}$, $w^{(0),(3)}$, $p^{(0),(3)}$, are readily obtained. Substituting these expressions and the boundary conditions of Eq. (1.18) into Eq. (1.17), we finally

get the RC.

$$R = \frac{-\kappa_f^{(3)}\kappa_f^{(0)}T_1 - i\kappa_f^{(3)}\rho_f^{(0)}\omega^2 T_2 + i\kappa_f^{(0)}\rho_f^{(3)}\omega^2 T_3 - \rho_f^{(0)}\rho_f^{(3)}\omega^4 T_4}{-\kappa_f^{(3)}\kappa_f^{(0)}T_1 - i\kappa_f^{(3)}\rho_f^{(0)}\omega^2 T_2 - i\kappa_f^{(0)}\rho_f^{(3)}\omega^2 T_3 + \rho_f^{(0)}\rho_f^{(3)}\omega^4 T_4}. \qquad (1.19)$$

where $T_i = \Gamma_{31}\Gamma_{42i} - \Gamma_{41}\Gamma_{32i}\,(i = 1,2)$ and $T_j = \Gamma_{31}\Gamma_{22j-4} - \Gamma_{21}\Gamma_{32j-4}\,(j = 3,4)$.

Liquid Interface

By changing the stiffness constant the spring model can approach either welded or slip boundary conditions. Real slip boundary conditions can be implemented by assuming a thin liquid layer of infinitesimal thickness. In the following we will derive the reflection coefficient for slip boundary conditions and show that it confirms the reflection coefficient derived in Eq. (1.19). Let us assume there is a very thin layer of liquid between layer 2 and layer 1. A transfer matrix for this liquid layer must also be provided in order to calculate the RC by the transfer matrix method. Following the same procedure as previously for the solid layer, we readily obtain

$$\begin{bmatrix} w^+ \\ p^+ \end{bmatrix} = \begin{bmatrix} \cos(\kappa_f d) & -\kappa_f/(\rho_f\omega^2)\sin(\kappa_f d) \\ \rho_f\omega^2/\kappa_f \sin(\kappa_f d) & \cos(\kappa_f d) \end{bmatrix} \begin{bmatrix} w^- \\ p^- \end{bmatrix} \qquad (1.20)$$

where w^+, p^+, w^- and p^- are normal displacement and excess pressure at the upper and lower interface of the liquid layer and d is the thickness of the liquid layer. Applying transfer matrices from layer to layer and with consideration of the appropriate boundary conditions, we derive the RC in this case.

$$R = \frac{i\kappa_f^{(3)}(i\kappa_f^{(0)}S_{21} - \rho_f^{(0)}\omega^2 S_{22}) + \rho_f^{(3)}\omega^2(i\kappa_f^{(0)}S_{11} - \rho_f^{(0)}\omega^2 S_{12})}{i\kappa_f^{(3)}(i\kappa_f^{(0)}S_{21} - \rho_f^{(0)}\omega^2 S_{22}) - \rho_f^{(3)}\omega^2(i\kappa_f^{(0)}S_{11} - \rho_f^{(0)}\omega^2 S_{12})}. \qquad (1.21)$$

where $[S_{ij}]$ is given by $[S_{ij}] = [TN_{im}^{(2)}][LT_{mn}][TN_{nj}^{(1)}]$, where $[LT_{ij}]$ is the liquid transfer matrices defined in Eq. (1.20), and $[TN_{ij}]$ is calculated using the $[C_{ij}]$ matrix defined in Eq. (1.11) from the following expression.

$$TN_{ij}^{(n)} = C_{2i2j}^{(n)} - C_{2i1}^{(n)}C_{32j}^{(n)}/C_{31}^{(n)}. \qquad i = 1,2, \qquad j = 1,2. \qquad (1.22)$$

Figure 1.3 shows the calculated RC in different cases. The acoustic constants used in the calculation are listed in [19]. Figure 1.3a) is the RC from a single steel plate with thickness 1.98 mm and frequency 1 MHz. Three modes can be excited. A_0. S_0. and A_1. which correspond to incident angles of 34.8°. 18.3°. 9.7° respectively. To test our method. we have calculated the RC for this case by two different means. one using the well known plate RC expression [6]. the other employing Eq. (1.19). In the second case we treat the 1.98-mm steel plate as two 0.99-mm steel plates bonded together with large boundary stiffness constants *kkt* and *kkn*: the results are identical. suggesting the validity of our approach. Plotted in Fig. 1.3b) is the RC of a rubber-steel bilayer modeled by assuming three different boundary stiffnesses *kkt* and *kkn*. The units of *kkt* and *kkn* are 10^{12} N/m^3 or TPa/m. We also assume the damping of the rubber varies linearly with frequency. Following a similar treatment in [20]. we define γ_l and γ_t as the longitudinal and transverse damping per unit frequency. yielding the following complex longitudinal and shear wavespeeds.

$$c_l^* = c_l(1 + i\gamma_l c_l/2\pi)\,. \tag{1.23}$$

$$c_t^* = c_t(1 + i\gamma_t c_t/2\pi)\,. \tag{1.24}$$

For the rubber layer in our experiment we have measured γ_l = and find a value of 0.16 Neper/(MHz·mm): we then assume γ_t = 0.32 Neper/(MHz·mm). Our measured value for γ_l is consistent with the results of Nolle and Mowry [21]. assuming a linear frequency dependence. With these boundary stiffnesses it can be seen that there are still three modes. and the corresponding angles are the same as for a single steel plate. The boundary stiffnesses affect only the amplitude of the RC. but have little influence on the position of the modes. The minimum at 60° corresponds to the critical angle of rubber and is not a Lamb mode angle. As *kkt* and *kkn* continue to decrease. however. the RC shows some different behavior. We see this effect in Fig. 1.3c). When *kkt* = 1 and *kkn* = 2 (solid curve). there are traces of minima in $|R|$ at 34.8°. 18.3°. and 9.7°.

indicating a very weak Lamb wave. When $kkt = 0.1$ and $kkt = 0.2$, corresponding to a total debond, no mode can be seen. In Fig. 1.3d) we compare the RC calculated from Eq. (1.19) assuming a large normal stiffness and a small tangential stiffness (solid curve) with that obtained by assuming a thin layer of water (dashed curve) between the rubber and steel (Eq. (1.21)). The two cases in Fig. 1.3d) approach each other closely. By adjusting kkt and kkn, the spring model can be used to simulate a full range of boundary rigidity.

Experimental Procedure

Several stainless steel shells 1.98 mm in thickness and 76.2 mm in radius with machined and polished surfaces have been prepared for these experiments. A 2.45-mm thick sheet of Buna-N rubber is adhered to the outer shell surface by room-temperature vulcanizing silicone sealant. The acoustic properties of the steel and rubber are collected in [19]. The shear properties of the rubber require some explanation. Because of the difficulty in measuring the shear velocity of rubber owing to its high acoustic loss, some assumptions have been made to infer a reasonable value. By assuming the bulk modulus of rubber is equal to that of water [22], we can calculate the shear velocity of rubber from $c_t^{rb} = [3(B^{fl} - \rho^{rb}(c_l^{rb})^2)/(2\rho^{rb})]^{1/2}$, where rb and fl stand for rubber and fluid. To prepare the surfaces for bonding both rubber and steel are thoroughly cleaned using mild organic solvents. A simulated debond is produced by omitting adhesive from a small area. The acoustic impedance of the silicone is very similar to that of the rubber, so it is unnecessary to consider the adhesive as a separate layer.

A multi-axis positioning system manufactured by Panametrics is used for all measurements reported here. The scanning system provides a total of five degrees of freedom for each independently controllable transducer: translation along the x, y and z axes, as well as rotation in the horizontal and vertical planes. Figure 1.1 shows a schematic dia-

gram of the experimental geometry. Acoustic beams from the transmitter and receiver are directed at the shell at equal angles of incidence from the surface normal. $\theta_{in} = \theta_{re}$. During an angle scan, the transmitter is held fixed, while the receiver is scanned around the circumference of the shell, maintaining the same incident angle and distance from the transducer surface to the interface. The observation angle θ is defined as the angle measured from the center of the shell between rays that pass through the intersection points of each transducer beam axis with the shell surface.

The transducers employed in these experiments are Ultran W575-1 flat piston transducers 19 mm in diameter and having a center frequency of 1 MHz. These transducers produce the acoustic beams approximated in the theoretical model. It has recently been demonstrated [23] that at any distance, including the near field, the combined directivity function of planar piston devices is essentially identical to that of the combined Gaussian beams employed in the theoretical model. Therefore, the voltage calculated in Eq. (1.4) using Gaussian beams is an accurate representation of the experimental signal using piston transducers. By fitting the central lobe of the piston transducer in the far field with a Gaussian beam, the Gaussian beam width at its waist can be obtained according to $w = 0.7517r$ [24], where r is the radius of transducer. This formula is used to estimate the Fresnel length b in the theoretical calculation.

Data collection is computerized and completely automated. The entire waveform is digitized at 8-bit resolution, and the data stream is sampled at a rate of 20 Msamples/s. The experimental results can be analyzed either in the time domain or frequency domain after performing a fast Fourier transform (FFT) on the acquired time-domain signal and extracting the component of interest.

Results and Discussion

In this section we present the results of experimental measurements and compare these to calculations for uncoated and coated steel shells having well and poorly bonded regions. Similarities and differences of each case, together with the prediction of the theoretical model, are analyzed and discussed. Since all the experiments are performed in the time domain, a sample of these results is presented first. A typical time domain waveform from a well bonded region in a layered shell is shown in Fig. 1.4. These waveforms are sampled at an observation angle of 25° after ten averages when the incident angle is 35°. The signal consists of two components: a leaky wave and a specular reflection. The specular reflection and leaky part travel different paths and have different velocities. The path of the specular reflection is confined entirely in the fluid, so this component travels with the fluid velocity. The leaky wave travels in the solid during its existence as a guided wave mode. From the transducer to the shell and back the propagation path is also in the fluid. The leaky wave velocity, however, will be a combination of both the fluid wavespeed and that of the Lamb mode excited by phase matching. Because of the higher Lamb wavespeed, the leaky wave arrives earlier than does the specular reflection, as shown in Fig. 1.4. This effect is especially pronounced at large observation angles.

We have also analyzed these experimental data in the frequency domain, where we have extracted only the 1-MHz component by performing a discrete transform on the data of Fig. 1.4. In Fig. 1.5 the amplitude of the 1-MHz component is plotted versus the observation scan angle θ at $\theta_{in} = 35°$, just at the phase-matching angle for the A_0 mode. Fig. 1.5a) shows the received voltage from a bare steel shell. The total field consists of a main lobe (essentially the specular reflection) followed by an oscillating trailing field signal. In the main lobe, interference of the specular and leaky wave components produces a dip around 5°, after which the two components sum in phase, producing

a second peak near 10°. Past this scan angle the leaky wave, decreasing by radiation damping, and the diffracted specular component continue to interfere, resulting in the characteristic oscillations seen between 20° and 40° in Fig. 1.5a), as predicted by theory. Similar results have been noted in earlier work [6].

For comparison, Fig. 1.5b) shows the received voltage from the bonded region of a rubber/steel layered shell. The signal is similar to that in Fig. 1.5a), except that the dip in the main lobe shifts to the right. Since the leaky wave is weaker in this case, the apparent interference of it and specular component is delayed until a higher observation angle, where the specular reflection is sufficiently small, illustrated by the second peak near $\theta = 15°$. Again, the comparison with calculation is quite good. Contrasting the trailing field in Fig. 1.5b) with that of the bare shell, we observe that changes in the total signal are largely the result of a reduction in leaky wave amplitude.

We have investigated the reasons why the leaky wave in the rubber-steel case is smaller than that for the bare steel shell. We speculate that two factors, the damping losses in the rubber and the bond rigidity conditions, contribute to the smaller leaky wave. First we consider the bond rigidity. Plotted in Fig. 1.6a) is the calculated transducer voltage by assuming different bond rigidities, while all other conditions are held constant. In Fig. 1.6b) are the corresponding experimental results, which are taken from different samples believed to have different bond rigidities. The calculation predicts our observations quite well. A visual comparison shows that the solid curve (kkt=100, kkn=200 TPa/m) is almost identical to the voltage in Fig. 1.5a). If the bond rigidity is one order of magnitude smaller (kkt=10, kkn=20 TPa/m, dashed curve), we can see the first peak increases while the second peak decreases, which indicates the specular part has gotten larger, and the leaky part is diminished.

This behavior can also be seen in the theoretical curve in Fig. 1.5b). As the bond rigidity is further reduced to $kkt = 5$, $kkn = 10$ (dash-dot curve), the first peak increases, and the second peak degenerates into a flat plateau. These curves show that the bond

rigidity strongly influences the leaky wave. The higher the bond rigidity, the smaller the influence of the rubber layer on the leaky wave. The theoretical calculation indicates that the imaginary part of the pole increases with boundary stiffness, which is shown in Fig. 1.6c). In this figure, the imaginary parts of the A_0 pole (solid curve) and its corresponding zero (dashed curve) are plotted as a function of the bond rigidity kkn with $kkt = kkn/2$. At large values of kkn the structure behaves as though the layers are in welded contact. The rubber, however, contributes little to the pole-zero pair, and for $kkn = 200$ TPa/m the A_0 mode in the steel layer alone has almost the same complex parameters. As kkn decreases the acoustic coupling between the layers is less, and we observe that the imaginary part of the pole decreases to a finite value and that of the zero increases, until $kkn \to 0$ where $\mathsf{Im}(\mathsf{k_p})$ approaches $\mathsf{Re}(\mathsf{k_p})$. In fact, vanishing kkn implies complete decoupling between the rubber and steel layers, so that the steel layer is not excited at all. The remnant imaginary parts of the pole-zero pair in Fig. 1.6c) arise from the hypothetical possibility of wave energy reradiation of into the lower fluid medium. Since their real parts are already almost identical, the effect on guided wave propagation in the layered structure of the A_0 pole-zero pair tends to vanish as the boundary stiffness decreases to small values.

Following [3, 23], the RC from a plate can be approximated by

$$R(k) = \frac{\Pi_{j=1}^{n}(k - k_0)}{\Pi_{j=1}^{n}(k - k_p)}. \tag{1.25}$$

¿From Eq. (1.4) we know that the RC pole residue determines the strength of the leaky wave, where the residue is proportional to $k_p - k_0$ from the approximate RC above. Since $\mathsf{Re}(\mathsf{k_p}) \approx \mathsf{Re}(\mathsf{k_0})$, $k_p - k_0 \approx \mathsf{Im}(\mathsf{k_p}) - \mathsf{Im}(\mathsf{k_0})$. Then, $\mathsf{Im}(\mathsf{k_p}) - \mathsf{Im}(\mathsf{k_0})$ as a function of kkn is plotted in Fig. 1.6c) as a dash-dot curve. It shows that the higher boundary rigidity leads to a stronger leaky wave. We can also expect that $\mathsf{Im}(\mathsf{k_p})$, $\mathsf{Im}(\mathsf{k_0})$ and $\mathsf{Im}(\mathsf{k_p}) - \mathsf{Im}(\mathsf{k_0})$ will not change very much as kkt and kkn continue to increase beyond the scale of the figure. From the RC in Fig. 1.3b) we can see that for $kkt = 100$ Tpa/m

and $kkn = 200$. R is almost identical with that for $kkt = 10^4$ TPa/m and $kkn = 10^4$ TPa/m. implying the bond with boundary rigidity of $kkt = 100$ and $kkn = 200$ TPa/m is already a very good bond. while $kkt = 10$ and $kkn = 20$ TPa/m is only slightly worse.

Second. we consider the influence of the rubber damping on the leaky wave. Signal voltages with different damping constants are shown in Fig. 1.7. Plotted in Fig. 1.7a is the amplitude of the receiver voltage calculated from Eq. (1.4). For all the curves in this figure the boundary rigidity is constant at $kkt = 10$ TPa/m. $kkn = 20$ TPa/m. To illustrate the effect of damping. we portray the calculated voltage signal for several values of γ_l and γ_t. chosen to bracket the values appropriate for buna-N rubber used in the experiments. The solid curve denotes $\gamma_l = 0.08$ Neper/(MHz·mm) and $\gamma_t = 0.16$ Neper/(MHz·mm). The γ_t value only is doubled in the dashed curve. and both γ_l and γ_t are doubled in the dash-dotted curves in Fig. 1.7a. As the damping of the rubber increases. the measured receiver voltage amplitude is observed to decrease. We have compensated experimentally. however. by employing higher gain in the receiver circuit and by increasing the transmitter voltage. The amplitude of each experimental curve in Fig. 1.7 is scaled and matched to a single point on the theoretical curves. In calculations of guided wave dispersion. the rubber damping loss is found to have essentially no effect on the poles or zeroes of the two-layer structure.

The signal voltage at an incident angle of 33°. 2° below the A_0 mode angle. is shown for a bare and layered shell in Fig. 1.8. Compared with Fig. 1.5a). the first minimum after 0° scan angle in Fig. 1.8a) shifts to the right. and the amplitude of the second peak decreases. Below the phase-match angle for the A_0 mode. behavior is observed that is reciprocal to that seen above 35°. namely. that the leaky wave maximum shifts to the right and correspondingly the point of phase cancellation (the first minimum) shifts right. The diffraction-related decrease in the specular reflection at large observation angles and the lower leaky wave amplitude owing to the incident angle deviation from the A_0 mode phase-match angle together produce a smaller constructive interference

peak around 15°. Meanwhile, the agreement between theory and experiment is also very good for the bare plate. For the bonded region of the layered steel in Fig. 1.8b), a similar effect on the receiver voltage can be observed. The difference between these two cases is explained in the same manner as the difference observed at 35°. Those comments apply here also.

Plotted in Fig. 1.9 is the signal voltage at an incident angle 18.5°, corresponding to the S_0 mode. For the bare steel shell case in Fig. 1.9a), the theory predicts the experiment result fairly well. For the rubber-steel case in Fig. 1.9b) the experiment is well modeled by theory in the specular and trailing field regions. Only at larger scan angles are some differences observed. The weaker leaky wave can be observed here also, as indicated by the disappearance of the minimum in the main lobe and the second in-phase constructive interference peak, which are clearly defined in the bare steel case, but not so with the rubber layer.

Finally, we present results from the rubber-steel debond region. A typical time-domain signal from this region is shown in Fig. 1.10. As in Fig. 1.4, this signal is also acquired at an observation angle 25° when the incident angle is 35°. There is only a specular reflection, however, and the leaky wave is no longer generated. A plot of the corresponding 1-MHz signal voltage component from the debond region as a function of scan angle is shown in Fig. 1.11. The incident angles are 35° for Fig. 1.11a) and 18.5° for Fig. 1.11b). Without the leaky wave, the field loses its oscillatory nature and decreases monotonically from 0° scan angle, since there is no longer a secondary field to cause interference. Only the specular reflection remains, as confirmed in the time-domain signal in Fig. 1.10. The prediction is quite close to the experiment. The signal voltage from the debond region at other incident angles has also been measured with similar results.

Conclusions

The extensive experimental results and theoretical calculations reported here indicate that leaky guided modes in the steel dominate in rubber-steel layered shells, and the rubber contributes no detectable leaky guided modes. The leaky wave modes are smaller, however, with a rubber layer present. We find that the bond rigidity determines the relative strength of the leaky wave. The greater the bond rigidity, the stronger is the leaky wave excitation. Debond totally suppresses leaky wave modes in the steel and results in only a specular reflection, where the damping in the rubber has little influence on the leaky wave. The model developed in this paper is not limited to two-layer elastic structures and could be extended to any layer geometry and to different kinds of imperfect boundary conditions.

Acknowledgment

The authors would like to thank Smaine Zeroug for helpful discussions. This work was performed with partial support from the Naval Surface Warfare Center (Carderock Div.) under project number N61533-95-K-0012.

References

[1] A. Schoch. Schallreflexion. Schallbrechung and Schallbeugung. [Sound reflection, refraction, and bending]. Ergeb. Exakten Naturwiss. (1950) **23** 127–234.

[2] H. L. Bertoni and T. Tamir. Unified theory of Rayleigh-angle phenomena for acoustic beams at liquid-solid interfaces. Appl. Phys. (1973) **2** 157–172.

[3] L. E. Pitts. T. J. Plona and W. G. Mayer. Theory of Nonspecular Reflection Effects for an Ultrasonic Beam Incident on a Solid Plate in a Liquid. IEEE Trans. Sonics Ultrason. (1977) **SU-24** 101–9.

[4] J. Pott and J. G. Harris. Scattering of an acoustic Gaussian beam from a fluid-solid interface. J. Acoust. Soc. Am. (1984) **76** 1829–38.

[5] J. G. Harris and J. Pott. Further studies of the scattering of an acoustic Gaussian beam from a fluid-solid interface. J. Acoust. Soc. Am. (1985) **78** 1072–80.

[6] D. E. Chimenti. J. Zhang. S. Zeroug. and L. B. Felsen. Interaction of acoustic beams with fluid-loaded elastic structures. J. Acoust. Soc. Am. (1994) **95** 45–59.

[7] T. J. Cloutier. A. Safaeinili. S. Zeroug. and D. E. Chimenti. An experimental study of ultrasonic beam reflection from fluid-loaded cylindrical shells. in *Review of Progress in Quantitative NDE* vol. 14. eds D. O. Thompson and D. E. Chimenti. (Plenum Press. New York. 1995). p. 131–37.

[8] F. L. Becker and R. L. Richardson. Ultrasonic Critical Angle Reflectivity. in *Research Techniques in Nondestructive Testing*. ed R. S. Sharpe. (Academic Press. London. 1970). Chap. 4.

[9] S. Zeroug and L. B. Felsen. Nonspecular reflection of two- and three-dimensional acoustic beams from fluid-immersed plane-layered elastic structures. J. Acoust. Soc. Am. (1994) **95** 3075–98.

[10] S. Zeroug and L. B. Felsen. Nonspecular reflection of two- and three-dimensional acoustic beams from fluid-immersed cylindrically layered elastic structures. J. Acoust. Soc. Am. (1995) **98** 584–98.

[11] G. A. Deschamps. Gaussian beam as a bundle of complex rays. Electron. Lett. (1971) **7** 684–85.

[12] B. A. Auld. General electromechanical reciprocity relations applied to the calculation of elastic wave scattering coefficients. Wave Motion (1979) **1** 3–10.

[13] S. Zeroug and F. E. Stanke. Ultrasonic pulsed beam interaction with a fluid-loaded elastic plate: Theory. J. Acoust. Soc. Am. (1996) **100** 1339–48.

[14] L. B. Felsen and N. Marcuvitz. *Radiation and Scattering of* Waves (Prentice Hall. Englewood Cliffs. 1973).

[15] Jai-Man Baik and R. B. Thompson. Ultrasonic scattering from imperfect interface: a quasi-static model. J. Nondestruct. Eval. (1984) **4** 177–196.

[16] F. J. Margetan. R. B. Thompson. T. A. Gray. Interfacial spring model for ultrasonic interaction with imperfect interface: theory of oblique incidence and application to diffusion-bonded butt joints. J. Nondestruct. Eval. (1988) **7** 131–152.

[17] A. Pilarski. J. L. Rose. K. Balasubramaniam. The angular and frequency characteristics of reflectivity from a solid layer embedded between two solids with imperfect boundary conditions. J. Acoust. Soc. Am. (1990) **87** 532–42.

[18] S. I. Rokhlin and Y. J. Wang. Analysis of boundary conditions for elastic wave interaction with an interface between two solids. J. Acoust. Soc. Am. (1991) **89** 503–15.

[19] Material properties of rubber: v_l(1.66km/s). v_t(0.78km/s). ρ(1.18g/cc): steel: v_l(5.66km/s). v_t(3.12km/s). ρ(7.9g/cc).

[20] D. E. Chimenti and A. H. Nayfeh. Ultrasonic leaky waves in a solid plate separating a fluid and vacuum. J. Acoust. Soc. Am. (1989) **85** 555–60.

[21] A. W. Nolle and S. C. Mowry. Measurement of ultrasonic bulk wave propagation in high polymers. J. Acoust. Soc. Am. (1948) **20** 432–39.

[22] A. W. Nolle. Dynamic mechanical properties of rubberlike materials. J. Polymer Science (1948)**5** 1–54.

[23] O. I. Lobkis. A. Safaeinili. D. E. Chimenti. Precision ultrasonic reflection studies in fluid-coupled plates. J. Acoust. Soc. Am. (1996) **99** 2727–36.

[24] R. B. Thompson and E. F. Lopes. The effects of focusing and refraction on Gaussian ultrasonic beams. J. Nondestruct. Eval. (1984) **4** 107–23.

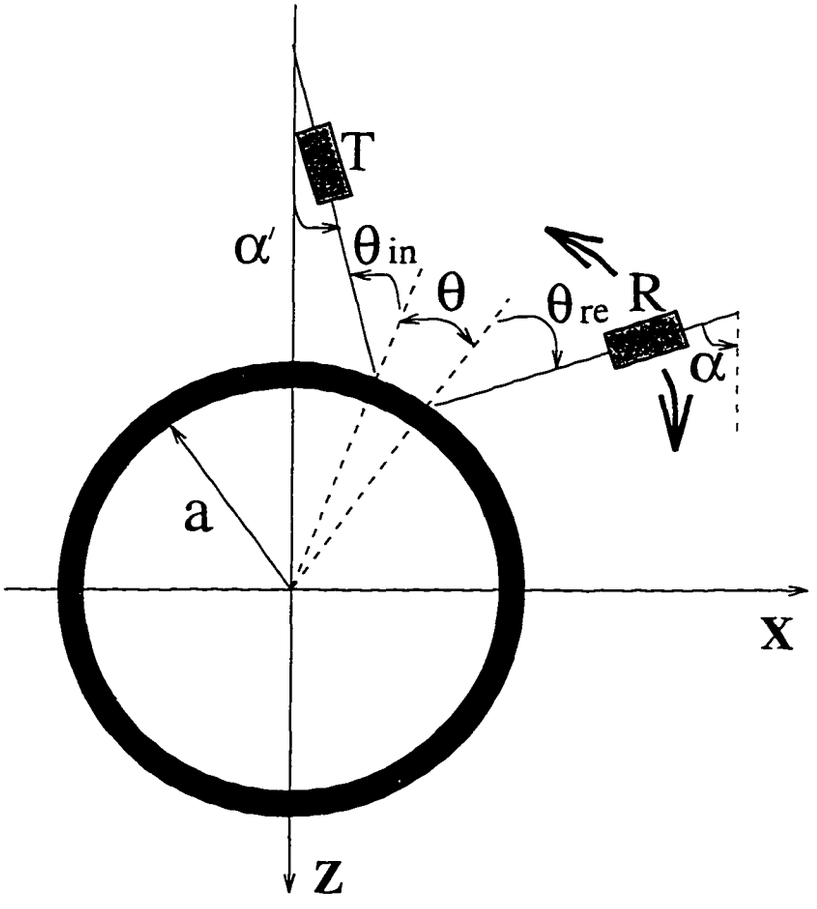

Figure 1.1 Schematic illustration of acoustic beam interaction with cylindrical elastic structures. T: transmitter, R: receiver, α': transmitter launch angle, α: receiver launch angle, θ_{in}: transmitter incident angle, θ_{re}: receiver incident angle, θ: observation scan angle.

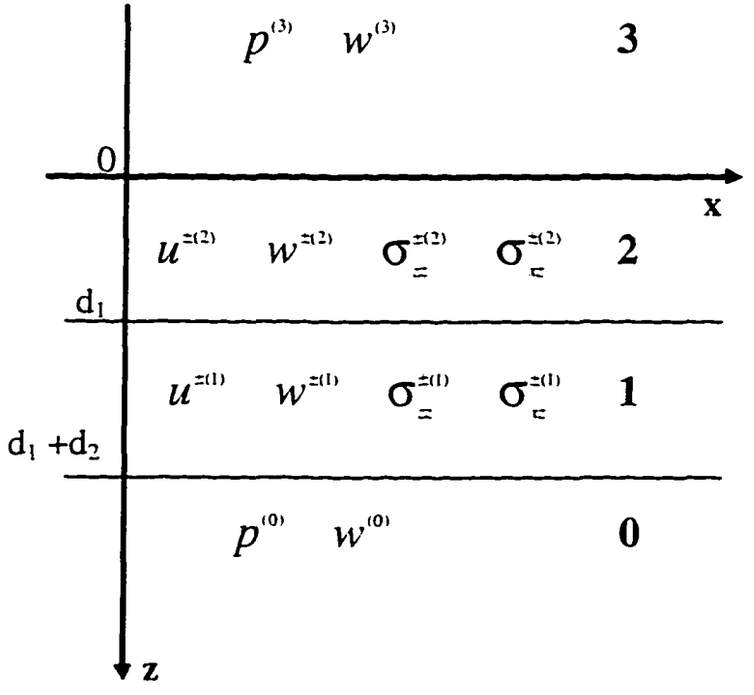

Figure 1.2 Four-layer structure used in the calculation of the reflection coefficient. In our experiments media 0 and 3 are liquid halfspaces. layer 1 is steel, and layer 2 is rubber.

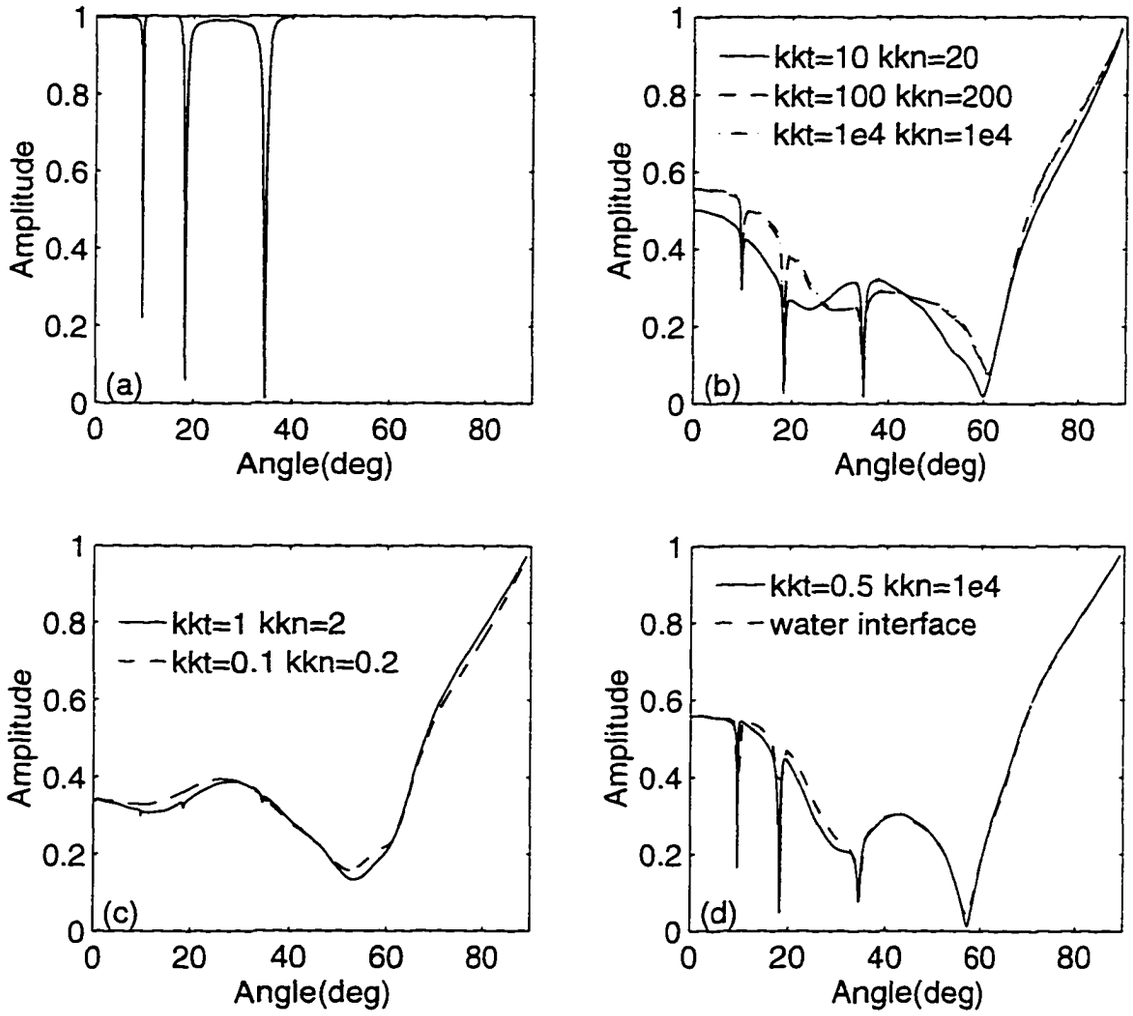

Figure 1.3 Reflection coefficient versus incident angle in several cases: a) single steel shell: b) good bond supports leaky modes: c)bad bond results no leaky mode: d) comparison of spring model and water interface.

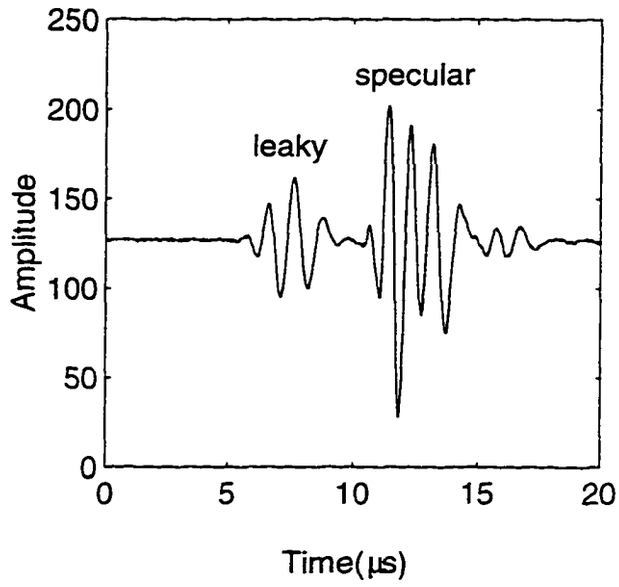

Figure 1.4 Typical time waveform from the bond region of the rubber-steel.

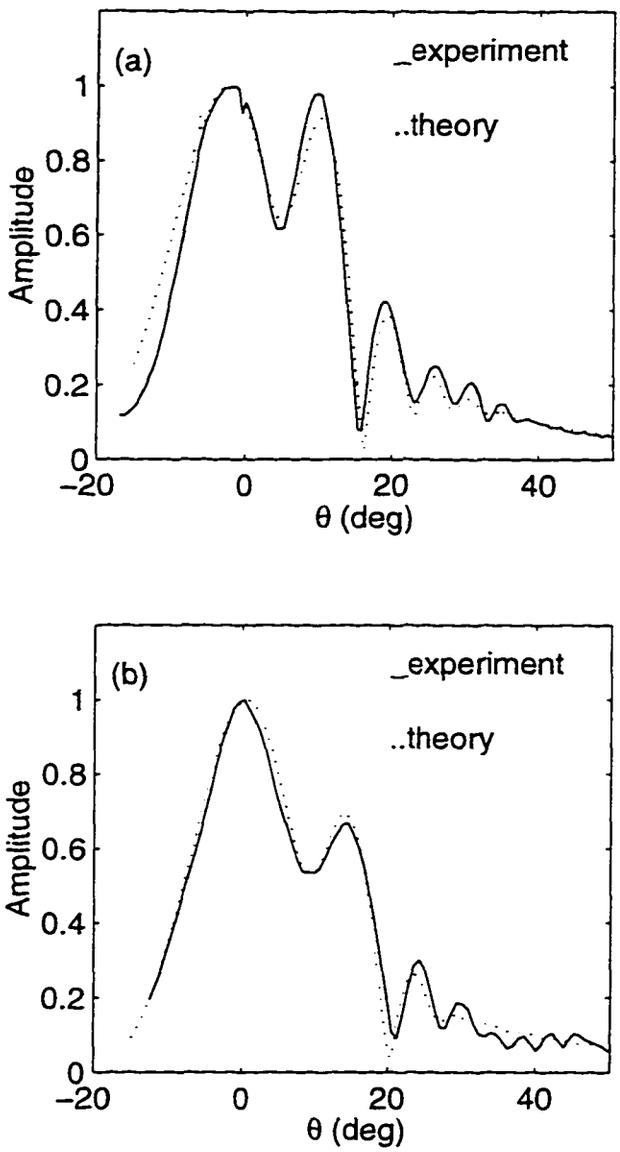

Figure 1.5 Reflected field from a) single steel shell: b) bond region of rubber-steel at incident angle 35° (A_0 mode).

Figure 1.6 Comparison of signal voltages from rubber-steel with different bond rigidity at an incident angle 35°. shows how the bond rigidity strongly influences the leaky wave. Frame a) shows the theoretical amplitude of the voltage. b) the experimental voltage. c) the imaginary part of the A_0 pole $\mathrm{Im}(k_p)$ (solid curve). A_0 reflection coefficient zero k_0 (dashed line). and their difference $\mathrm{Im}(k_p) - \mathrm{Im}(k_0)$ as a function of boundary stiffness (kkn=2kkt).

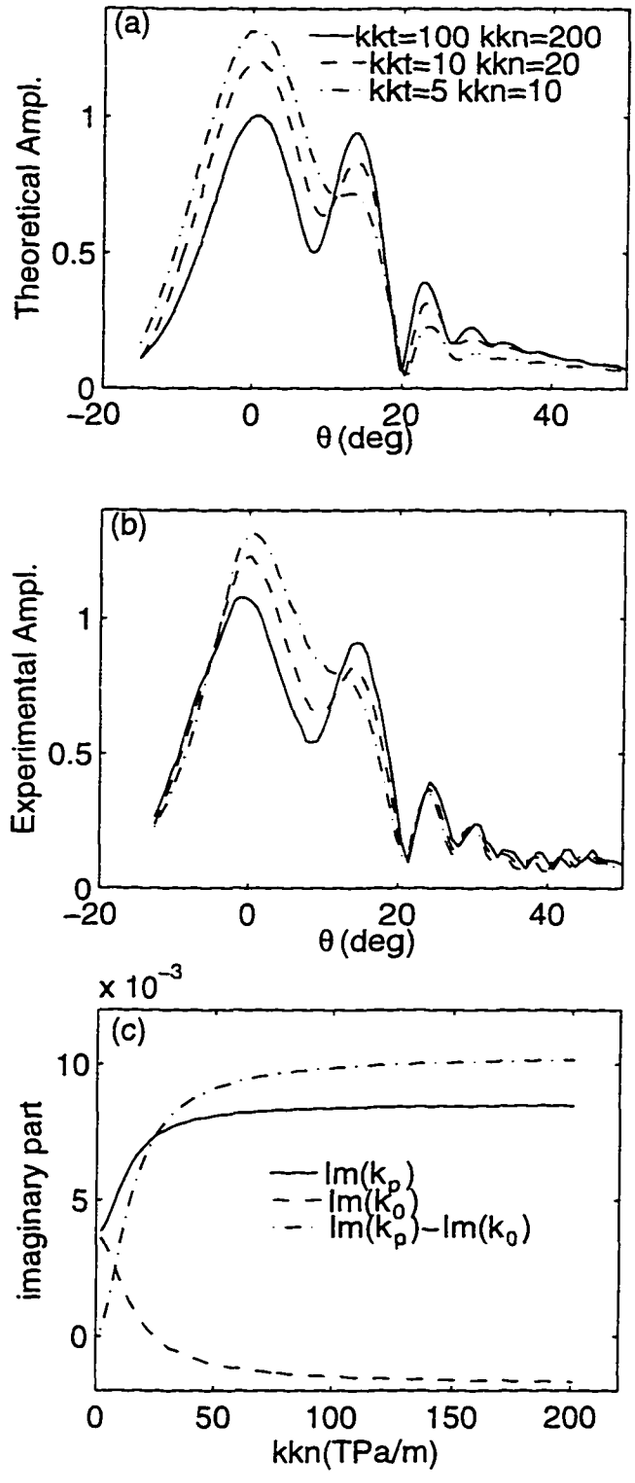
(a)
kkt=100 kkn=200
kkt=10 kkn=20
kkt=5 kkn=10
Theoretical Ampl.
θ (deg)
(b)
Experimental Ampl.
θ (deg)
x 10^-3
(c)
imaginary part
Im(k_p)
Im(k_0)
Im(k_p)−Im(k_0)
kkn(TPa/m)

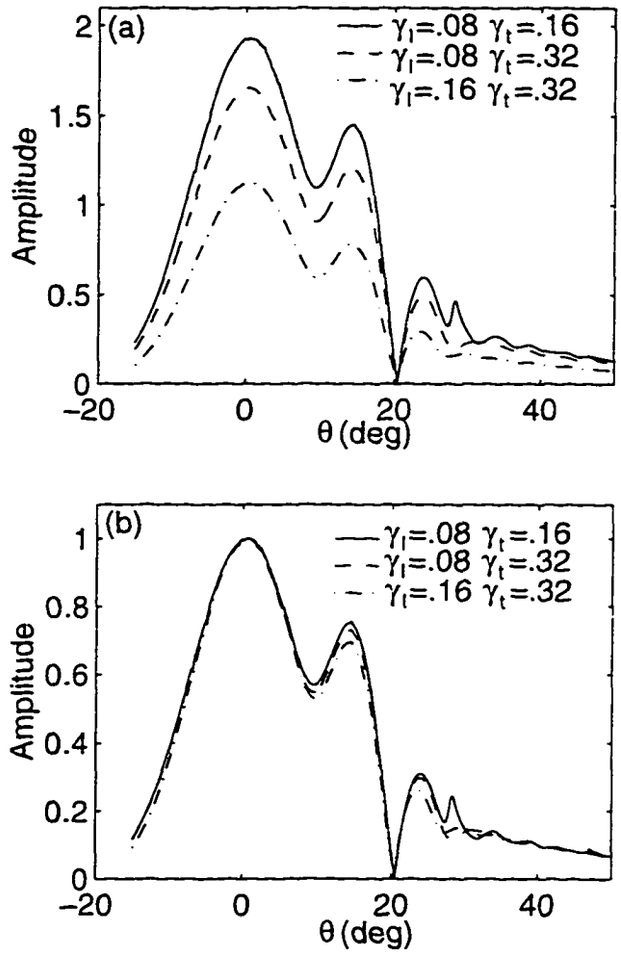

Figure 1.7 Comparison of calculated voltage with different rubber damping at an incident angle of 35°. In a) are the absolute results; b) normalized result.

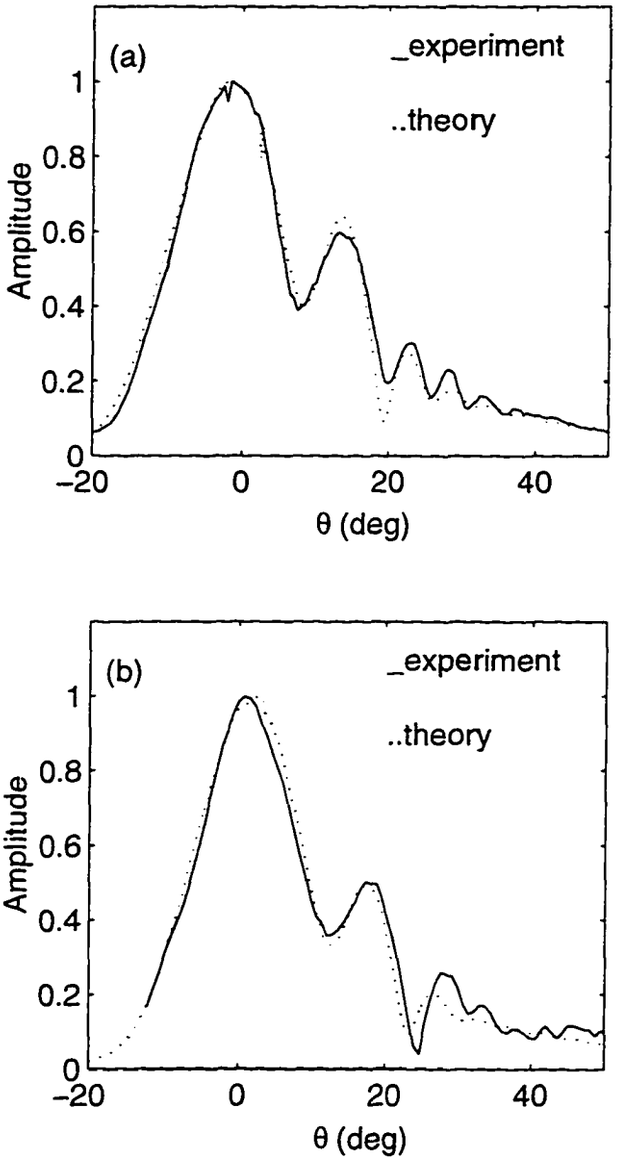

Figure 1.8 Receiver voltage from a) bare steel shell: b) bond region of rubber-steel at incident angle 33°.

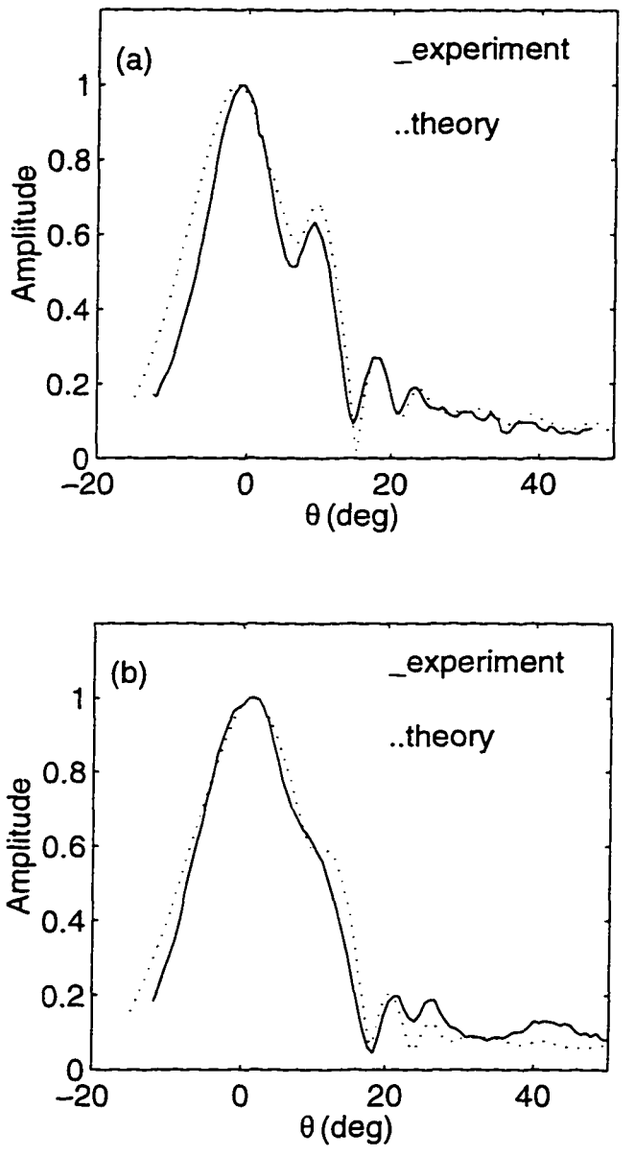

Figure 1.9 Receiver voltage from a) single steel shell; b) bond region of rubber-steel at incident angle 18.5°.

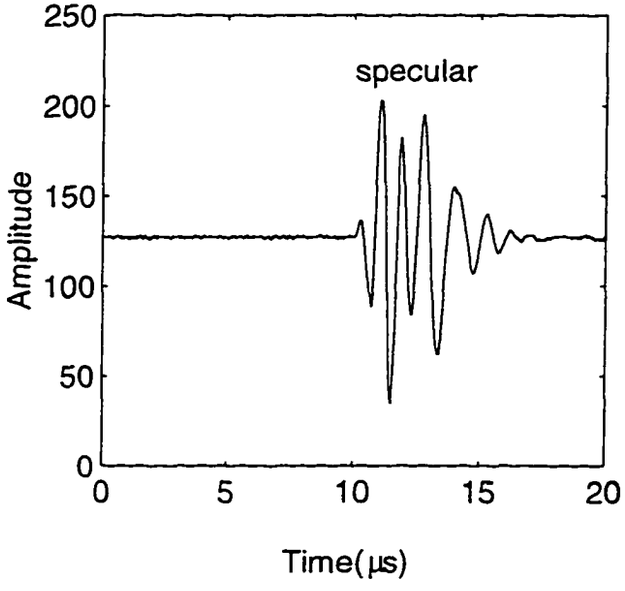

Figure 1.10 Typical time-domain waveform from the debond region of the rubber-steel.

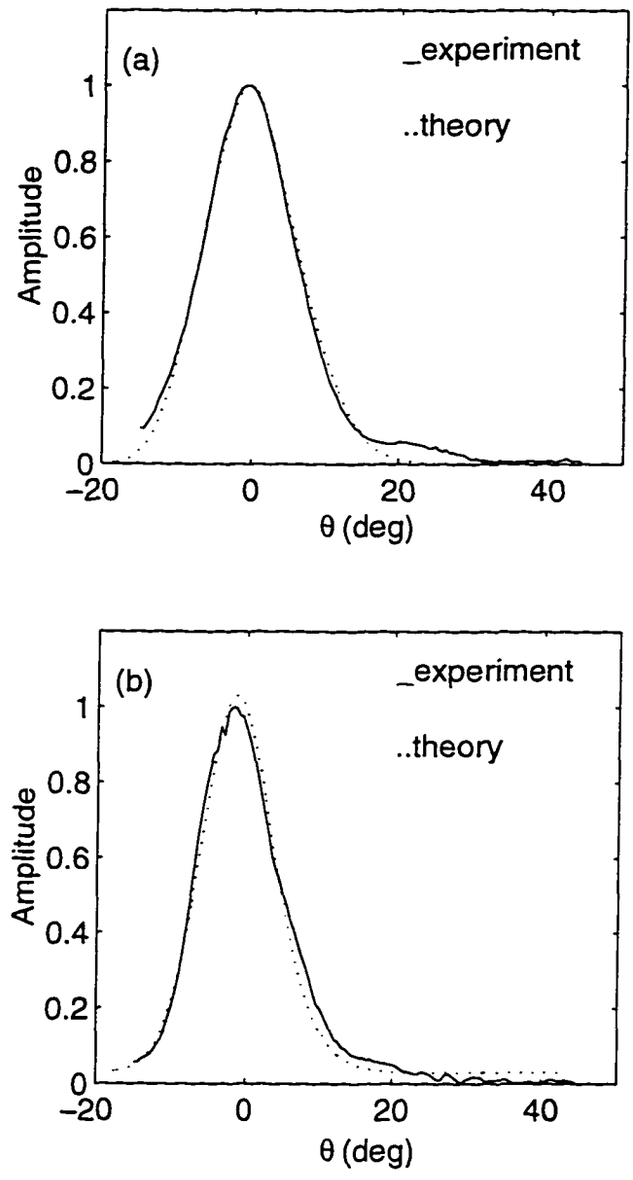

Figure 1.11 Signal voltage from debond region of the rubber-steel at an incident angle of a) 35°. and b) 18.5°.

CHAPTER 2 TRANSDUCER MISALIGNMENT EFFECTS IN BEAM REFLECTION FROM ELASTIC STRUCTURES

A paper submitted to the Journal of Acoustical Society of America

Han Zhang, Dale E. Chimenti and S. Zeroug

Abstract

In two-transducer, fluid-coupled ultrasonic reflection measurements phase-matched to guided modes of elastic solid structures, differences between the receiver angle and the incident beam angle on the receiver voltage have been studied. The received voltage is typically due to contributions from the specular reflection and any of the several possible guided wave modes excited by the incident wave field. It is found that misalignment leads to changes in the relative amplitudes of the various contributions. Further, the more highly collimated the beam (or the contributor), the more pronounced are the effects. It is shown that the signal maximum is not a reliable indicator of receiver alignment. These conclusions are based on measurements and calculations that have been performed at incident angles selected both close to, or far from, phase-matching angles to guided wave modes on plates, curved surfaces, and cylindrical shells. Receiver voltage coordinate scans have been performed with receiver angles misaligned from the incident beam axis by 1° to 4°. The receiver voltage versus scan parameter in planar and curved structures is calculated by employing complex transducer points to synthesize

transducers with Gaussian apertures, spectral analysis to formulate the beam-structure interaction problem, and asymptotic methods to evaluate the resulting spectral integrals. The model predictions are generally in good agreement with the experiments.

Introduction

Ultrasonic pitch-catch measurements performed with a pair of acoustic transducers, especially when critical angle phenomena play a role, represent a common characterization method in nondestructive evaluation [2]–[10]. One application of this technology is to near-field leaky wave (LW) measurements where material properties of immersed layered elastic structures can be determined. In LW measurements the acoustic transducer beams are aligned at phase-matching angles to excite efficiently one or more of the structure's propagating wave modes. The amplitude and phase of the scattered acoustic energy, collected and converted to an electrical voltage by the phase-sensitive receiving transducer, depends not only on the properties of the structure but also on those of the transducers. Their apertures and alignment angles are particularly significant parameters. Alignment issues are especially important for wide transducers that radiate or receive over a narrow angular range.

While transducer alignment in a pitch-catch geometry has been recognized as a potential problem among workers in ultrasonic materials characterization, there remain difficulties in the quantitative assessment of its effect on measurements. The reasons lie in the challenge of making high-resolution voltage measurements with the required transducer alignment precision in the incident and reflected angles. Yet, the importance of misalignment effect is clear. In an experimental arrangement where the receiver voltage is a function of both extrinsic experimental parameters, such as the transducer aperture size, alignment angle, transducer beam shape, and position, and of intrinsic parameters such as the elastic properties of the structure, systematic errors in the extrinsic

parameters could be misinterpreted as the result of differing intrinsic parameters.

In near-field LW measurements, the option of relying on some attribute of the scattered signal (e.g., amplitude maximum of the specularly-reflected component) to deduce the alignment accuracy is neither an unequivocal, nor independent measure of the effect. This is so because several acoustic components may impinge on the receiving transducer aperture, each with a ray bundle having a different average angle and with a different phase. To help assess quantitatively these issues, we have used a computationally efficient computer code built on an analytical model. The model is versatile enough to handle transducers with arbitrary apertures and alignments and interacting with planar and cylindrical fluid-immersed elastic structures.

In our own previous research we have employed two transducers in a pitch-catch geometry to study nonspecular reflection of diverging acoustic beams from a planar interface and of collimated beams from a curved interface [9, 10]. We measure the receiver voltage as a function of scan distance or scan angle, and we have found that the experimental results are generally well predicted by an asymptotic complex-ray model [11, 12, 16]. In this article we investigate the influence of transducer misalignment in reflected acoustic beam measurements, where the transducer acoustic beams are incident at, or near, phase-matching angles to couple to one or to several of the structure's guided wave modes (Rayleigh or Lamb). In this circumstance the alignment of the transducers proves to be quite important. It is our purpose in this study to discover what effects small transducer misalignment will have on the receiver signal. We analyze the misalignment effects on the scattered beam both at and near the critical incidence for phase-matched coupling to structure-borne guided waves.

In the next section we present a brief summary of the asymptotic complex-ray model, followed by the detailed experimental results analyzed in the light of the model calculation.

Theoretical Summary

The configurations assumed and depicted in Fig. 2.1 are composed of isotropic and homogeneous fluid-elastic layers excited by ultrasonic acoustic transducers in a pitch-catch mode. The transmitting and receiving transducers, denoted by $\mathcal{T}$ and $\mathcal{R}$ respectively, are considered to be passive, linear, and electro-acoustically reciprocal. $\mathcal{T}$ is aligned at angle $\alpha_{\mathcal{T}}$ with respect to the y axis and insonifies the uppermost (outermost) fluid-solid interface at angle $\theta_{\mathcal{T}}$ with respect to the interface local normal. $\theta_{\mathcal{T}}$ is selected so as to excite one or more of the leaky waves that can be supported by the elastic structure. Similarly, $\mathcal{R}$ is aligned at angle $\alpha_{\mathcal{R}}$ and its beam axis defines the angle $\theta_{\mathcal{R}}$ with respect to the local normal of the interface. In a scan of the scattered pressure field, the receiver is displaced parallel to the interface maintaining a fixed angle $\theta_{\mathcal{R}}$.

The numerical code developed to simulate this measurement is based on an extension of a theoretical model that has been presented elsewhere [9]-[16]. The solution relies on a spectral integral representation of the receiving transducer voltage and the beam-structure interaction. Within this representation, transducer beams are specified in terms of Gaussian beams generated through the complex-transducer-point (CTP) technique [14]. Asymptotic treatment of the spectral integrals involved leads to closed-form solutions for the dominant contributions to the scattered signal, namely, the specularly-reflected (SR) field and the leaky waves excited. In the following, we restrict the presentation to the CTP procedure that is pertinent to our study. Detailed development of the approach is given in refs. [9]-[16].

When piston transducers are employed experimentally in matched pairs, as they are here, their combined effect on the receiver signal voltage is nearly identical to the effect of a pair of transducers producing Gaussian beams. Demonstration of this correspondence and discussion of the reasons for its validity have recently been presented by Lobkis, *et al.* [17]. We note that, if necessary, a collection of coaxial Gaussian beams for

each transducer may be used to achieve higher accuracy [14]. In the CTP technique, each transducer ($\mathcal{T}$ or $\mathcal{R}$) aperture and alignment angle are specified through complex coordinates that are conveniently given in terms of Cartesian forms $(x_{\mathcal{T}}, y_{\mathcal{T}})$ or $(x_{\mathcal{R}}, y_{\mathcal{R}})$. These forms can be used directly in the planar geometry. For the cylindrical geometry, they have to be adapted through the usual transformation from Cartesian to polar coordinates $(m_{\mathcal{T}}, o_{\mathcal{T}})$ and $(r_{\mathcal{R}}, o_{\mathcal{R}})$. [14]

$$r_{\mathcal{T},\mathcal{R}} = \sqrt{x_{\mathcal{T},\mathcal{R}}^2 + y_{\mathcal{T},\mathcal{R}}^2}\,. \qquad \mathrm{Re}\{r_{\mathcal{T}}, r_{\mathcal{R}}\} \geq 0: \qquad o_{\mathcal{T},\mathcal{R}} = \tan^{-1}\{x_{\mathcal{T},\mathcal{R}}/y_{\mathcal{T},\mathcal{R}}\}\,. \quad (2.1)$$

where,

$$x_{\mathcal{T}} = x' + ib_{\mathcal{T}} \sin\alpha_{\mathcal{T}}\,. \qquad x_{\mathcal{R}} = x - ib_{\mathcal{R}} \sin\alpha_{\mathcal{R}}\,. \qquad b_{\mathcal{T},\mathcal{R}} \geq 0\,.$$

$$y_{\mathcal{T}} = y' + ib_{\mathcal{T}} \cos\alpha_{\mathcal{T}}\,. \qquad y_{\mathcal{R}} = y + ib_{\mathcal{R}} \cos\alpha_{\mathcal{R}} \qquad \alpha_{\mathcal{T},\mathcal{R}} \geq 0\,. \quad (2.2)$$

The real positive parameters $b_{\mathcal{T}}$ and $b_{\mathcal{R}}$ specify the CTP beam Fresnel lengths, respectively. They are related to the $1/e$ widths, $W_{\mathcal{T}}$ and $W_{\mathcal{R}}$, of the distribution profiles of $\mathcal{T}$ and $\mathcal{R}$, through $W_{\mathcal{T}} = \sqrt{2b_{\mathcal{T}}/k_f}$ and $W_{\mathcal{R}} = \sqrt{2b_{\mathcal{R}}/k_f}$, respectively ($k_f = \omega/v_f$, v_f is the sound speed in the fluid). The beam waists of $\mathcal{T}$ and $\mathcal{R}$ are centered at (x', y') and (x, y), respectively. The CTP beams attain maximum amplitude along lines at angles $\alpha_{\mathcal{T}}$ and $\alpha_{\mathcal{R}}$, which are therefore defined as their alignment angles.

As mentioned above, for an angle (o) scan along a circular arc of radius r as shown in Fig. 1, the Cartesian coordinates of the receiving aperture center (x, y) are varied such that $x = r\sin o$ and $y = r\cos(\pi - o)$. The receiver angle $\alpha_{\mathcal{R}}$ is also updated, keeping the receiver incidence angle $\theta_{\mathcal{R}}$ on the shell surface constant, where $\alpha_{\mathcal{R}} = \arcsin[a/r\sin\theta_{\mathcal{R}}] - o$, and a is the radius of the outermost interface. In the actual experiment and in Sect. III, the observation angle is measured more conveniently as the angular spread θ_0 between the intersection points of the transducer beam axes with the shell surface (see Fig. 1(b)). We note that θ_0 is linearly proportional to o [13].

II. EXPERIMENTAL PROCEDURE

Stainless steel plates, solid cylinders, and cylindrical shells of various dimensions have been measured to test the limitations of the theoretical model. The geometrical and acoustic properties of the samples are listed in [18]. The surfaces of the specimens are carefully machined, but not ground, and their flatness and parallelism are checked to assure these aspects do not contribute to significant systematic errors. All measurements are conducted using ULTRAN W575-1 19-mm diameter, 1-MHz, flat piston transducers.

Two scanning systems have been used in the experiments. A Parker-Daedel system with precision linear control is used for the experiments of planar structures. The scanning axes have a resolution of 0.01 mm and a position repeatability of of 0.03 mm. The transducer and receiver are mounted on precision rotary stages with a usable angular resolution of 0.01°. The mechanical system and the data acquisition electronics are described in detail elsewhere [19]. The transducer is excited with radio-frequency (rf) tone bursts of 1 MHz center frequency. The entire received signal is amplified by a high-gain broadband receiver and averaged using a Lecroy 9340 digitizing oscilloscope. Off-line Fourier transforms are performed on the received data, and the complex 1-MHz component is extracted and plotted as a function of scan coordinate.

The scanning system used for the cylindrical structures is a multi-axis positioning system manufactured by the Panametrics Company. The system provides five degrees of freedom for each transducer: translation along the x, y, and z axes, as well as rotation in the horizontal and vertical planes. Fig. 2.1(b) shows a schematic of the experimental geometry. The transmitter and receiver are directed at the cylindrical sample at angles of θ_T and θ_R with respect to the surface normal. During an angular scan, the transmitter remains fixed while the receiver is scanned through an arc centered on the cylinder axis, maintaining the same incident angle. Both transducers remain at a constant distance from the interface throughout the scan. The observation angle (θ_0) is the angle on the cylinder surface between the intersection points of the central rays of the two transducers with the surface (see Fig. 1(b)). The receiver beam axis denotes the axis of maximum

far-field sensitivity or the center of the beam directivity function were the transducer to operate as a transmitter.

The entire waveform is digitized at 8 bits at each measurement point with a sampling rate of 20 MHz. We extract the 1-MHz component (the transducer center frequency) via an FFT, and plot it as a function of observation angle θ_0. In the plots, the zero position is defined as the intersection of the two transducer central rays at the surface of the solid. Each plot contains the magnitude of the voltage for several receiver angular alignments. More complete descriptions of the apparatus and method can be found in [9, 17, 20].

Results and Discussion

Since the misalignment effects in planar and curved geometries display rather different characteristics, we discuss the results in these two cases separately. First, we address the planar structures, followed by the cylindrical ones.

Planar Structures

For the 19-mm diameter transducer and at the 1-MHz transducer center frequency, four guided wave modes can be excited with varying efficiency in the 3.04 mm-thick steel plate used in this experiment, depending on the incident angle. These are the A_0, S_0, A_1 and S_1 modes, corresponding to phase-match angles of 32.8°, 27.9°, 14.98°, and 14.15°, respectively.

Our experimental incident angle is chosen to be either at, or distant from, one of these Lamb mode angles, while the receiver angle is intentionally misaligned from the incident angle in a range from -2° to 2°, usually at 1° increments. In a manner similar to the cylindrical geometry, the zero of scan coordinate in the following plots is defined as the intersection of the transducer central rays at the sample surface. The receiver

voltages at different receiver angles are recorded in a single plot in order to enhance direct comparison of the misalignment effects. When the receiver angle is misaligned from the incident angle, the amplitude of the received voltage decreases, since the position of the maximum shifts away from the transducer axis ($x = 0$ mm). This situation is illustrated in Fig 2.2. When the receiver angle decreases a small amount, the receiver voltage maximum will lie along the chain-dashed line, with the receiver pointing at the center of the incident beam reflection. The voltage maximum occurs at the position for which the receiver aperture is in closest alignment with the scattered pressure wavefront.

We report first an experiment at an incident angle of $\theta_T = 20°$. Since 20° is far from the phase-match angle for both the S_0 and A_1 modes, we can use this choice to isolate the effects of misalignment on the specular reflection. The experimental results and theoretical calculation at different receiver angles ($\theta_R = 20°$, 19°, and 21°) are shown in Figs. 2.3(a) and (b). The voltage is dominated by the specularly-reflected acoustic pressure, which has a nearly Gaussian profile [17]. The voltage maximum amplitude is smaller for the misalignment case because less acoustic energy impinges on the receiver aperture at the position where a maximum occurs. These results are similar to the theoretical pitch-catch calculations presented for the scanned field amplitude voltage at fixed range of Gaussian transducers [14]. The shift in the voltage maximum is not symmetric with respect to the receiver misalignment angle because of the asymmetry introduced by the reflection process, especially when there is an incident diverging beam. This asymmetry can be seen more clearly in the theoretical results of Fig. 2.3(b) than in the experimental results of Fig. 2.3(a).

The A_0 mode is excited at a phase-match angle of 32.8°: these data are plotted as a function of scan coordinate in Fig. 2.4(a) for the measured and 4(b) for the predicted receiver voltages. The voltage is a coherent sum of the specular reflection and the strongly excited leaky Lamb wave. At 32.8° incidence angle we expect that the A_0 mode will be the dominant contribution to the leaky wave signal. From Fig. 2.4 it can

be seen that as the receiver angle is increased from 30.8° to 34.8°, the minimum at $x = 20$ mm becomes less pronounced, indicating that the ratio of leaky wave to specular reflection decreases. At perfect alignment $\theta_R = \theta_T$, the SR voltage contributes a larger amplitude than the A_0 wavefield, and because they are out-of-phase (in this region), their interference leads to a mild dip as shown by the solid curve in Fig. 2.4 (a) and (b). When the receiver angle decreases to 30.8° the leaky wave is strengthened at the expense of the specular reflection, and the two components become comparable in amplitude to each other, leading to a very pronounced minimum near $x = 20$ mm. On the other hand, when the receiver angle increases to 34.8°, the leaky wave decreases faster than does the specular component, and the minimum can hardly be seen.

We also note that in the SR region ($x \approx 0$) the strength of the received voltage becomes larger as θ_R decreases, as can be observed for the $\theta_R = 31.8°$ curve. The increase, which is seemingly inconsistent with the conclusions obtained from Fig. 2.3, is ascribed to the effect of the S_0 mode which is excited in this region by the steep rays of the misaligned incident beam. A separate calculation of the S_0 leaky wave shows that it is in phase with the specular part in this region.

The misalignment effects at incident angle of 30° are shown in Fig. 2.5 with experimental results in 5(a) and theoretical calculation in Fig. 2.5(b). With an incident angle of 30°, between A_0 and S_0 mode angles, weaker coupling to the leaky waves is seen when compared with Fig. 2.4. The Gaussian-like shape of the SR (near $x = 0$ mm) is almost unperturbed, unlike the data of Fig. 2.4, except near $\theta_R = 28°$. Here, the contribution of the S_0 mode is important enough to lead to an increase of the total voltage in the region $x < -10$ mm, whereas the decrease in the contribution of the A_0 mode leads to a decrease in the leaky wave amplitude beyond $x = 25$ mm.

Investigating misalignment for S_0-mode phase matching at an incidence angle of 28°, the experimental receiver voltages as a function of scan distance are plotted in Fig. 2.6(a). In frame (b) the theoretical amplitudes are recorded for the same conditions. For the

aligned case. $\theta_T = \theta_R = 28°$. and for the misaligned cases. $\theta_R = 26°$. $27°$. $29°$. and $30°$. The curve for the aligned cases in either plot is shown in solid. and the others are indicated on the legend. For this incidence angle the S_0 mode dominates. but the A_0 mode is also excited. This hypothesis is confirmed by the plots in Fig. 2.6c) and (d) for the calculated contributions of the A_0 and S_0 leaky modes. respectively. Similar to the case of $30°$ incidence above. the degree of excitation of these two modes depends on the receiver (mis)alignment. It can be seen that for $\theta_R = 26°$. the excitation and detection of the S_0 mode is the strongest. while that for the A_0 is the weakest.

The situation reverses itself for $\theta_R = 30°$. Quantifying the isolated contributions of these two modes helps explain some of the features seen in the receiver voltage. The amplitude of the voltage dip near $x \approx 0$ follows the S_0 mode strength. that is. the S_0 mode interferes with the specularly reflected field to yield a minimum there. while the second peak after the dip correlates with the strength of the A_0 mode. Furthermore. the smooth decay of the voltage amplitude in the LW region ($x > 40\,\text{mm}$) for $\theta_R = 26°$ and $27°$ owes to the fact that among the three components (S_0. A_0. and SR) only the S_0 is non-negligible in that region. For $\theta_R = 30°$. however. the voltage decay in this region is oscillatory owing to the interference between the S_0 mode and the A_0 mode. whose mode strength is clearly not negligible. as shown in Fig. 2.6(c).

Finally. we investigate misalignment effect at an incident angle of $16°$. close to the A_1 mode and S_1 mode phase matching angles. The experimental results and theoretical calculations at this incidence angle are shown in Fig. 2.7. Here. too. we see the transducer misalignment effects on the receiver voltage. In this case. however. since the phase matching angles are close ($14.98°$ and $14.15°$) and both smaller than the incident beam angle ($16°$). the decrease in the receiver angle favors both A_1 and S_1 modes. resulting in a strongly perturbed specular beam shape and a large. undifferentiated trailing field ($x > 50\,\text{mm}$) amplitude in the receiver voltage. When the receiver angle is as low as $14°$. the specular reflection is also highly distorted.

It should be noted that in all of the plots in Figs. 3–7. the agreement between theory and experiment is quite satisfactory. especially considering some of the intricate structure of the voltage owing to the interference phenomena operative here. The agreement encourages confidence in the model predictions.

Cylindrical Interfaces

The misalignment effects on reflection from curved structures are investigated using steel solid cylinders and steel shells. Since only Rayleigh modes propagate in solid cylinders. the simpler case of the solid cylinder is presented first. To assess the misalignment effects on a specular beam reflected from a solid cylinder. we select an incidence angle that is far from the Rayleigh critical angle.

With a Rayleigh angle for the water-steel interface of 31°. a 20° incidence angle would mostly avoid Rayleigh wave excitation and permit us to examine the effect on the specular component. This assumption is confirmed by the experimental results and theoretical calculations shown in Fig. 2.8(a) and (b). For the SR region. we can see that when the receiver angle deviates from the incidence angle by 2°. either above or below. the specular reflected beam peak decreases very little. and its shape changes almost not at all. At a deviation angle of 4° the beam amplitude begins to weaken. Compared with planar structures. in which 1° of misalignment results in much larger amplitude decreases. the effect of misalignment on the specular reflection is really rather small here. This fact suggests that the curvature-induced divergence of the SR beam. as captured within the extent of the receiving aperture. is larger than few degrees. such that there always are rays that are aligned with the receiving aperture axis even when this latter is misaligned with respect to the incident beam axis. This situation results in a smaller sensitivity of the receiving aperture for the curved interface than from a planar interface. in which upon reflection a collimated incident beam remains collimated. We recall from our previous work [9. 5] that the reflection of a collimated beam from a curved surface

is equivalent to the reflection of a diverging beam from a planar surface.

As the misalignment angles exceed 20°, the leaky Rayleigh wave contribution becomes less negligible. Here we see a distinct increase in receiver voltage in the scan angle range beyond 25°, where the Rayleigh wave, because of its constant-angle leakage, radiates an angularly-collimated beam (*i.e.*, rays depart from the surface at a constant angle, regardless of scan angle coordinate [9, 12]). The averaging effect of the receiver aperture is much more sensitive to the leaky Rayleigh wave than to the specular contribution.

On the basis of the above analysis we examine the misalignment effects for incidence at the Rayleigh critical angle 31°. The experimental results and theoretical calculations for the receiver voltage are shown in Fig. 2.9 for various receiver misalignment angles. Here, too, there is a good agreement between theory and experiment. The curves for the aligned case are shown in dark solid. The Rayleigh wave is efficiently excited, and the minimum close to 0° follows the strength of the leaky Rayleigh wave, as verified in separate calculations. Separated by this minimum, the two main lobes show a decrease of one peak simultaneous with the increase in the other. This effect is mainly a result of the receiver aperture averaging process. For the specular peak (below 0° scan angle) the steep ray favors a receiver aperture with small receiver angle θ_R, while for the leaky wave (above 0° scan angle), the slant ray favors a receiver aperture with a larger receiver angle.

Moving to the case of cylindrical shells, we investigate misalignment effects on a 57.3-mm radius steel shell of thickness 2.28mm. We approximate the reflection coefficient of the curved shell by that of a planar structure having the same thickness. As shown in Viktorov [21], this replacement is still very accurate for our shell thickness and radius. At 1 MHz, the shell supports three principal Lamb modes, A_0, S_0 and A_1, with corresponding phase-match angles 33.3°, 20.5°, and 11.8°.

In Fig. 2.10(a) and (b) we study misalignment from an incidence angle of 26°, lying between the A_0 and S_0 modes. The experimental results, together with the theoretical

prediction. are shown in frame (a) of this figure. At this incidence angle. we expect both modes to be efficiently excited. and the calculated leaky wave mode analyses for the two candidate modes are shown in Fig. 2.10(c) and (d). The changing receiver scan angle will favor one mode or the other. From -20° to 0° scan angle. the misalignment effects on the S_0 are most prominent at any receiver misalignment angle from $-4°$ to $+4°$ with respect to 26°. The gradual increase in the predicted S_0 mode amplitude yields the receiver voltage increase shown in Fig. 2.10(a) and (b) at a scan angle less than 0°.

Above 10°. the misalignment has a more pronounced influence on the A_0 mode. but the situation is reversed here. The decrease of the receiver angle weakens the leaky wave and thus the total receiver voltage. It can also be seen that the largest peak in the receiver voltage. occurring around 5° scan angle in Fig. 2.10(a) and (b). for the case when the receiver angle is 26° is almost the same as that for the case when the receiver angle is 28°. In this particular case. the S_0 mode leaky wave and the specular contribution are out-of-phase. The lower amplitude of the S_0 leaky wave mode at a receiver angle of 28° appears to compensate for the decrease in the specular component because of misalignment. This observation strongly reinforces the assertion made in the Introduction that a simple amplitude test alone is an insufficient basis for a transducer alignment decision.

The experimental and theoretical results of transducer misalignment at an incident angle of 35°. 5° above the Rayleigh angle. on the steel shell in water are shown in Fig. 2.11 frames (a) and (b). At this incident angle the A_0 mode leaky makes the dominant contribution to the signal. The misalignment effects observed earlier with the solid steel cylinder at Rayleigh angle incidence can be seen here also. As the receiver angle decreases. the excitation and reception strength of the A_0 pole increases resulting in a larger total voltage for scan angles below about $-10°$ and in a more pronounced minimum near 0° in the total receiver voltage.

Conclusion

In this article we have investigated the effects of receiver misalignment in leaky wave near-field measurements. We have, in particular, experimentally tested a computationally efficient and approximate (2D) modeling code for piston transducers interacting with plates and cylinders in fluid. We have found that the effects of receiver misalignment are most pronounced (*i.e.*, a drastic change in the voltage amplitude occurs) for cases where the signal is composed of more than one component. The effect is particularly strong when one, or more than one, of these components are collimated (linearly for the plane geometry and angularly for the cylindrical geometry) and impinges on the receiver at angles differing from each other. It is shown that misalignment effects lead to an enhancement of one or more components (specular reflection and/or leaky wave) at the expense of the other contributions. Having thus gained confidence in our model predictions, we propose to extend this study to the effects of transducer aperture size on the voltage amplitude and phase, and to the ramifications of these issues on material parameter characterization.

Acknowledgment

This work has been supported in part by the Naval Surface Weapons Center under contract N615339-K-0012. S.Z. acknowledges support from Schlumberger-Doll Research.

References

[1] A. Schoch, "Schallreflexion, Schallbrechung and Schallbeugung", [Sound reflection, refraction, and bending], Ergeb. Exakten Naturwiss **23**, 127–34 (1950).

[2] H. L. Bertoni and T. Tamir, "Unified theory of Rayleigh-angle phenomena for acoustic beams at liquid-solid interfaces", Appl. Phys. **2**, 157–72 (1973).

[3] L. E. Pitts, T. J. Plona, and W. G. Mayer, "Theory of Nonspecular Reflection Effects for an Ultrasonic Beam Incident on a Solid Plate in a Liquid," IEEE Trans. Sonics. Ultrason. **SU-24**, 101–09 (1977).

[4] T. J. Plona, L. E. Pitts, and W. G. Mayer, "Ultrasonic bounded beam reflection and transmission effects at liquid/solid-plate/liquid interface," J. Acoust. Soc. Am. **6**, 1324–1328 (1976).

[5] J. Pott and J. G. Harris, "Scattering of an acoustic Gaussian beam from a fluid-solid interface," J. Acoust. Soc. Am. **76**, 1829–1838 (1984).

[6] J. G. Harris and J. Pott, "Further studies of the scattering of an acoustic Gaussian beam from a fluid-solid interface," J. Acoust. Soc. Am. **78**, 1072–1080 (1985).

[7] W. G. Neubauer, "Observation of acoustic radiation from plane and curved surfaces", in *Physical Acoustics*, vol. 10, eds. W. P. Mason and R. N. Thurston, (Academic Press, New York, 1973), p. 85.

[8] F. L. Becker, R. L. Richardson, "Ultrasonic Critical Angle Reflectivity," in *Research Techniques in Nondestructive Testing*, ed R. S. Sharpe, (London and New York, 1970) Chap 4.

[9] D. E. Chimenti, J. Zhang, S. Zeroug and L. B. Felsen, "Interaction of acoustic beams with fluid-loaded elastic structures", J. Acoust. Soc. Am. **95**, 45–59 (1994).

[10] T. J. Cloutier, A. Safaeinili, D. E. Chimenti, S. Zeroug, and L. B. Felsen, "An Experimental Study of Ultrasonic Beam Reflection From Fluids Loaded Cylindrical Shells," Review of Progress in Quantitative NDE, **14**, eds. D. O. Thompson and D. E. Chimenti, (Plenum, New York, 1995), 131–138.

[11] S. Zeroug. L. B. Felsen. "Nonspecular reflection of two- and three-dimensional acoustic beams from fluid-immersed plane-layered elastic structures". J. Acoust. Soc. Am. **95**. 3075–3098 (1994).

[12] S. Zeroug. L. B. Felsen. "Nonspecular reflection of two- and three-dimensional acoustic beams from fluid-immersed cylindrically layered elastic structures". J. Acoust. Soc. Am. **98**. 584–598 (1995).

[13] T. J. Cloutier. A. Safaeinili. D. E. Chimenti.Smaine Zeroug. and L. B. Felsen. "Ultrasonic beam reflection from fluid-loaded cylindrical shells." submitted to J. Applied Physics.

[14] S. Zeroug. F. E. Stanke. and R. Burridge. "A complex-transducer-point model for emitting and receiving ultrasonic transducers." Wave Motion **24** (1996). 21–40.

[15] S. Zeroug "Efficient modeling of finite acoustic beam excitation and detection of interface and bulk waves on planar and cylindrical fluid-solid structures." *Review of Progress in Quantitative NDE*. **15**. Eds. D. O. Thompson and D. E. Chimenti. (Plenum. New York. 1996). .

[16] S. Zeroug. "Spectral integral formulae for the response of acoustic transducers in cylindrically curved configurations". submitted to IEEE Trans. on Ultras. Ferro-electr. Freq. Contr.

[17] O. I. Lobkis. A. Safaeinili. D. E. Chimenti. "Precision ultrasonic reflection studies in fluid-coupled plates". J. Acoust. Soc. Am. **99**. 2727–2736 (1996).

[18] Plate: thickness=3.04 mm. $v_l = 5.64$ km/s. $v_t = 3.07$ km/s. $\rho = 7900$ kg m^{-3}: Cylinder: radius=76.2 mm. $v_l = 5.66$ km/s. $v_t = 3.12$ km/s. $\rho = 7900$ kg m^{-3}: Shell: radius=57.3 mm. thickness=2.28 mm. $v_l = 5.66$ km/s. $v_t = 3.12$ km/s. $\rho = 7900$ kg m^{-3}.

[19] P. J. Shull. D. E. Chimenti. and S. K. Datta. "Elastic guided waves and the Floquet concept in periodically layered plates". J. Acoust. Soc. Am. **95**. 99 (1994).

[20] T. J. Cloutier. "Acoustic Beam Reflection from Curved. Layered Media". MS Thesis. Iowa State University (1995).

[21] I. A. Viktorov. *Rayleigh and Lamb Waves: Physical Theory and Applications.* (Plenum Press. New York. 1967). 113–16.

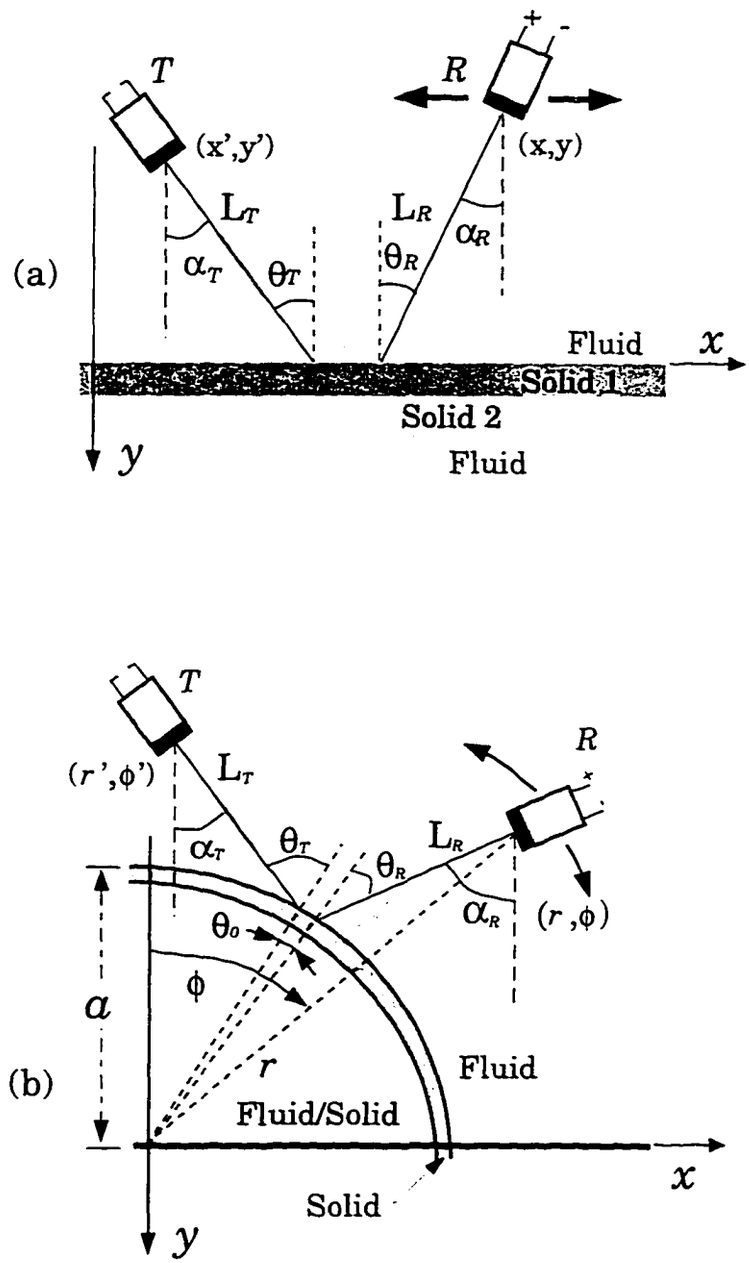

Figure 2.1 Geometries for plane and cylindrically layered fluid-immersed elastic configurations excited by acoustic transducers. $\mathcal{T}$: transmitter. $\mathcal{R}$: receiver. Note that only a quadrant of the cylindrical structure is shown.

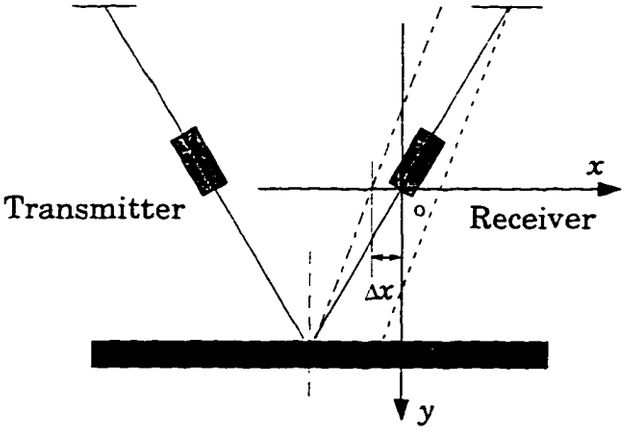

Figure 2.2 Schematic illustrating the shift of maximum receiver voltage owing to its misalignment. Solid line denotes the aligned beam axis. the dashed and dotted lines the misaligned beam axis. and Δx is the shift distance of the maximum voltage when the receiver is misaligned.

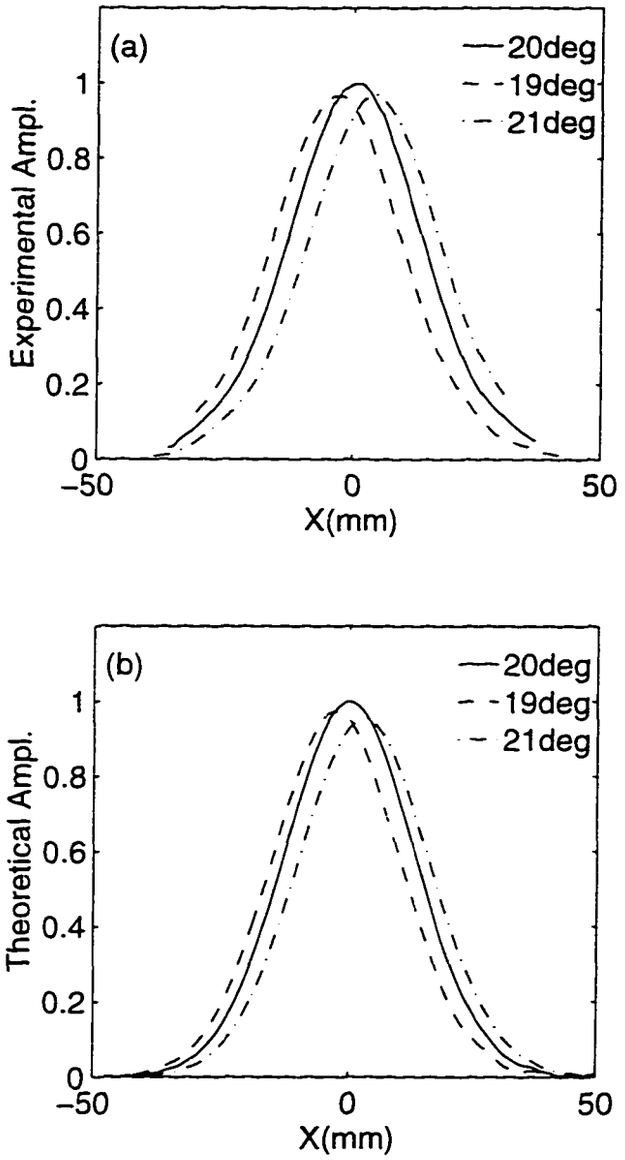

Figure 2.3 Transducer voltage with pitch-catch geometry for sound beam interaction with a plate in water. Experimental data are in frame (a) and theoretical receiver voltage in (b) as a function of scan distance when $\mathcal{R}$ is aligned: $\theta_{\mathcal{R}} = \theta_{\mathcal{T}} = 20°$. and when it is misaligned: $\theta_{\mathcal{R}} = 19°$ and $\theta_{\mathcal{R}} = 21°$.

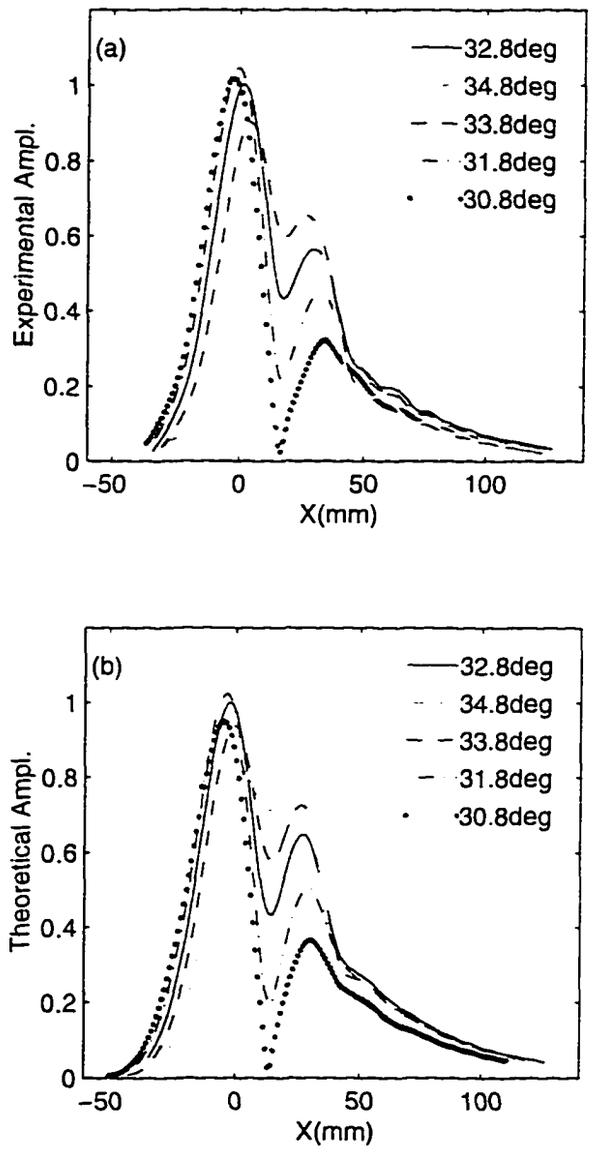

Figure 2.4 Transducer voltage for a plate in water. Experimental data are in frame (a), and theoretical receiver voltage in (b) as a function of scan distance when $\mathcal{R}$ is aligned: $\theta_{\mathcal{R}} = \theta_{\mathcal{T}} = 32.8°$, and when it is misaligned: $32.8° \pm 1°$, and $32.8° \pm 2°$. For all plots, $\theta_{\mathcal{T}} = 32.8°$.

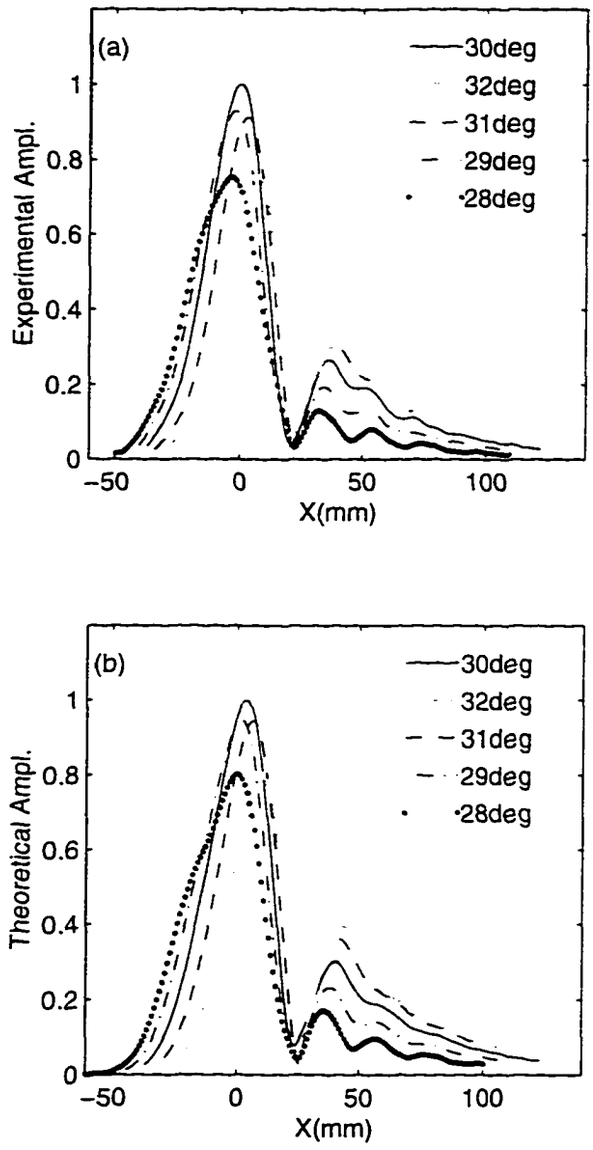

Figure 2.5 Transducer voltage for sound beam interaction with a plate in water: experimental data are in (a). and theoretical receiver voltage in (b) as a function of scan distance when $\mathcal{R}$ is aligned: $\theta_{\mathcal{R}} = \theta_{\mathcal{T}} = 30°$. and when it is misaligned: $30° \pm 1°$. and $30° \pm 2°$. For all plots. $\theta_{\mathcal{T}} = 30°$.

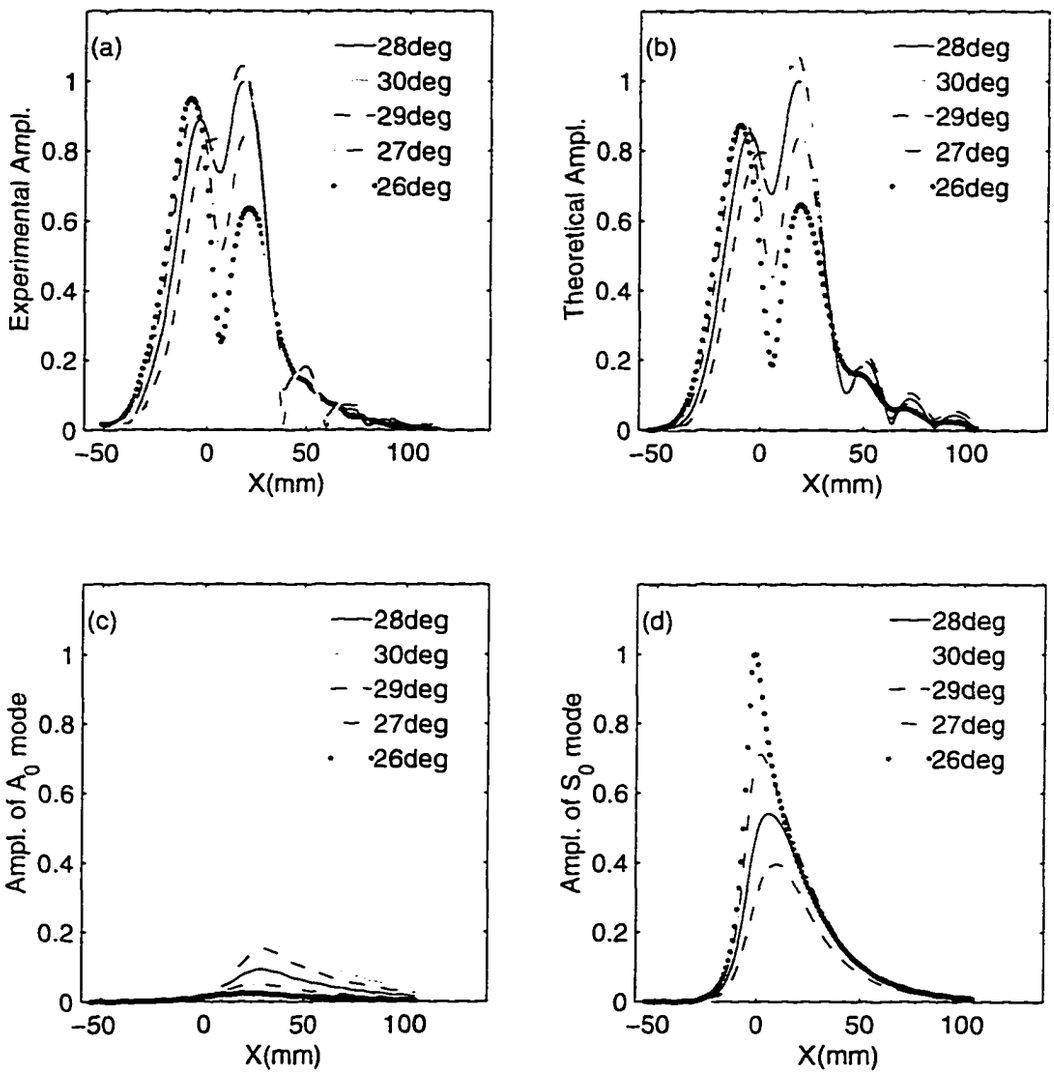

Figure 2.6 Transducer voltage for sound beam interaction with a plate in water: experimental data are in (a), and theoretical receiver voltage in (b) as a function of scan distance when $\mathcal{R}$ is aligned: $\theta_{\mathcal{R}} = \theta_{\mathcal{T}} = 28°$, and when it is misaligned: $28° \pm 1°$, and $28° \pm 2°$. For all plots, $\theta_{\mathcal{T}} = 28°$. The corresponding calculated profiles of the leaky A_0 mode (c) and S_0 mode (d) are shown for reference.

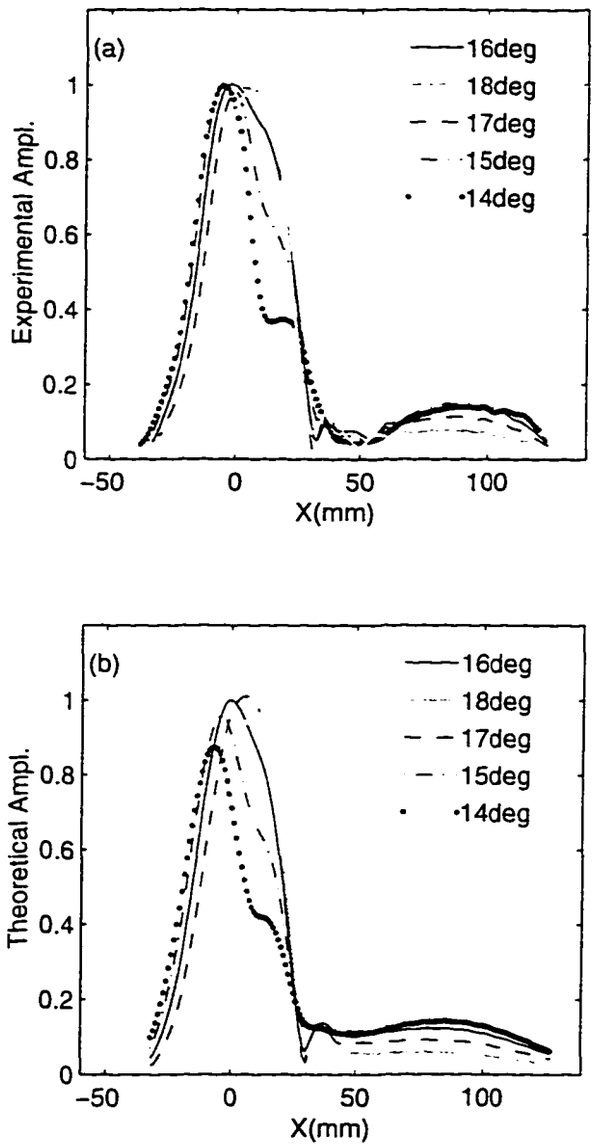

Figure 2.7 Transducer voltage for sound beam interaction with a plate in water: experimental data are in (a), and theoretical receiver voltage in (b) as a function of scan distance when $\mathcal{R}$ is aligned: $\theta_{\mathcal{R}} = \theta_{\mathcal{T}} = 16°$, and when it is misaligned: $16° \pm 1°$, and $16° \pm 2°$. For all plots, $\theta_{\mathcal{T}} = 16°$.

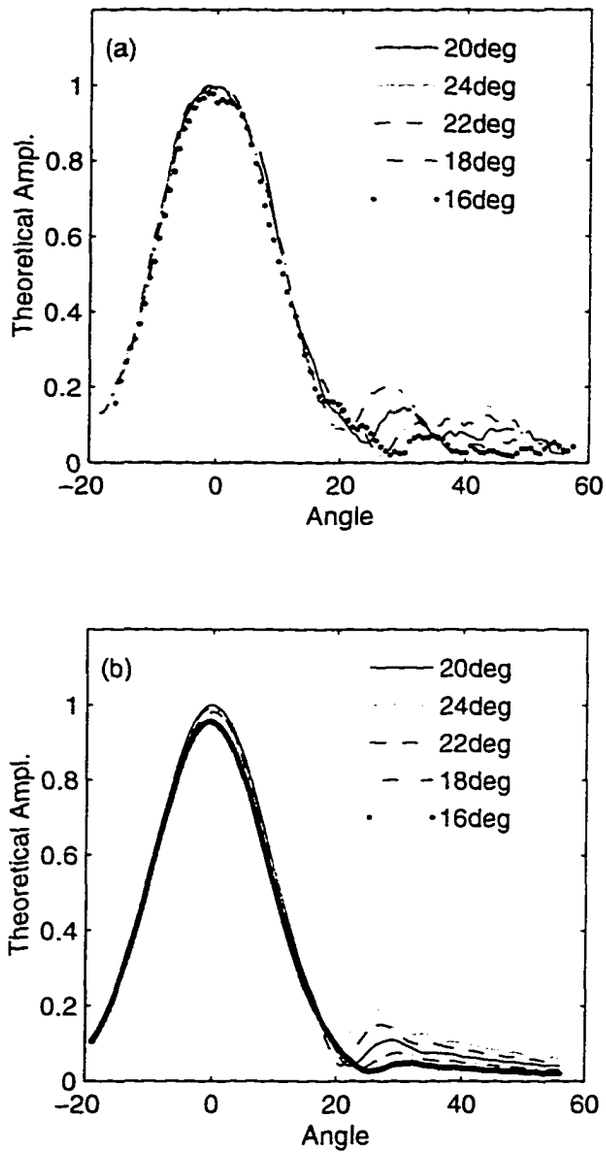

Figure 2.8 Transducer voltage for a solid cylinder in water: experimental data are in (a), and theoretical voltage in (b) as a function of scan angle for $\mathcal{R}$ aligned: $\theta_{\mathcal{R}} = \theta_{\mathcal{T}} = 20°$, and when it is misaligned: $20° \pm 2°$, and $20° \pm 4°$. For all plots, $\theta_{\mathcal{T}} = 20°$. The voltage is established primarily by the specularly-reflected field except in the region above 20°, where the leaky Rayleigh wave dominates.

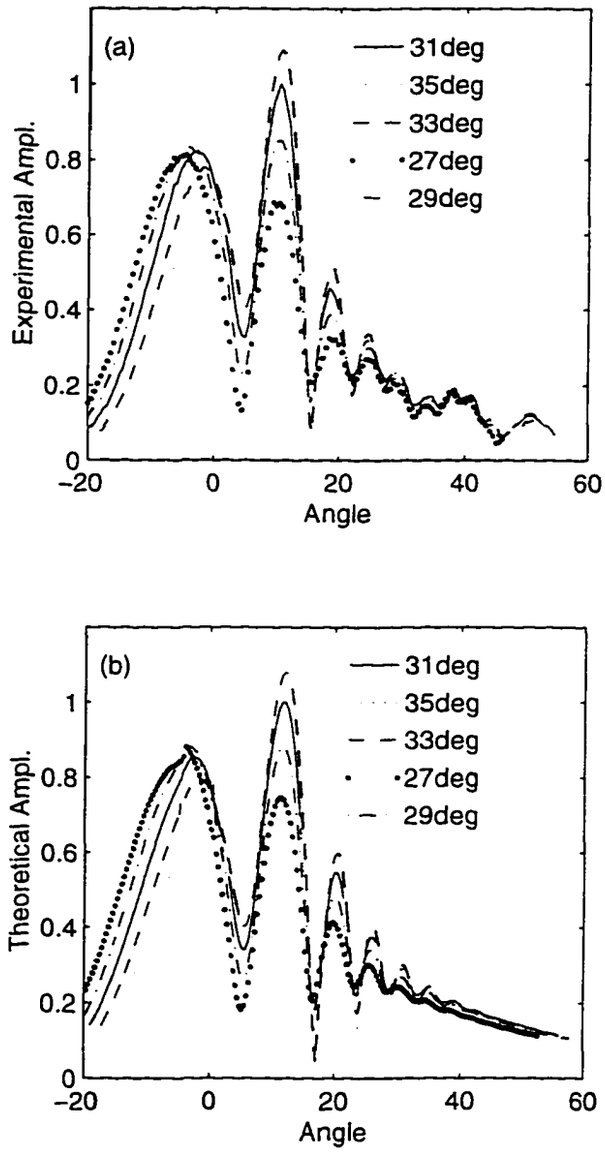

Figure 2.9 Transducer voltage for a solid cylinder in water: experimental data are in (a), and theoretical voltage in (b) as a function of scan angle when $\mathcal{R}$ is aligned: $\theta_{\mathcal{R}} = \theta_{\mathcal{T}} = 31°$, and when it is misaligned: $31° \pm 2°$, and $31° \pm 4°$. For all plots, $\theta_{\mathcal{T}} = 31°$.

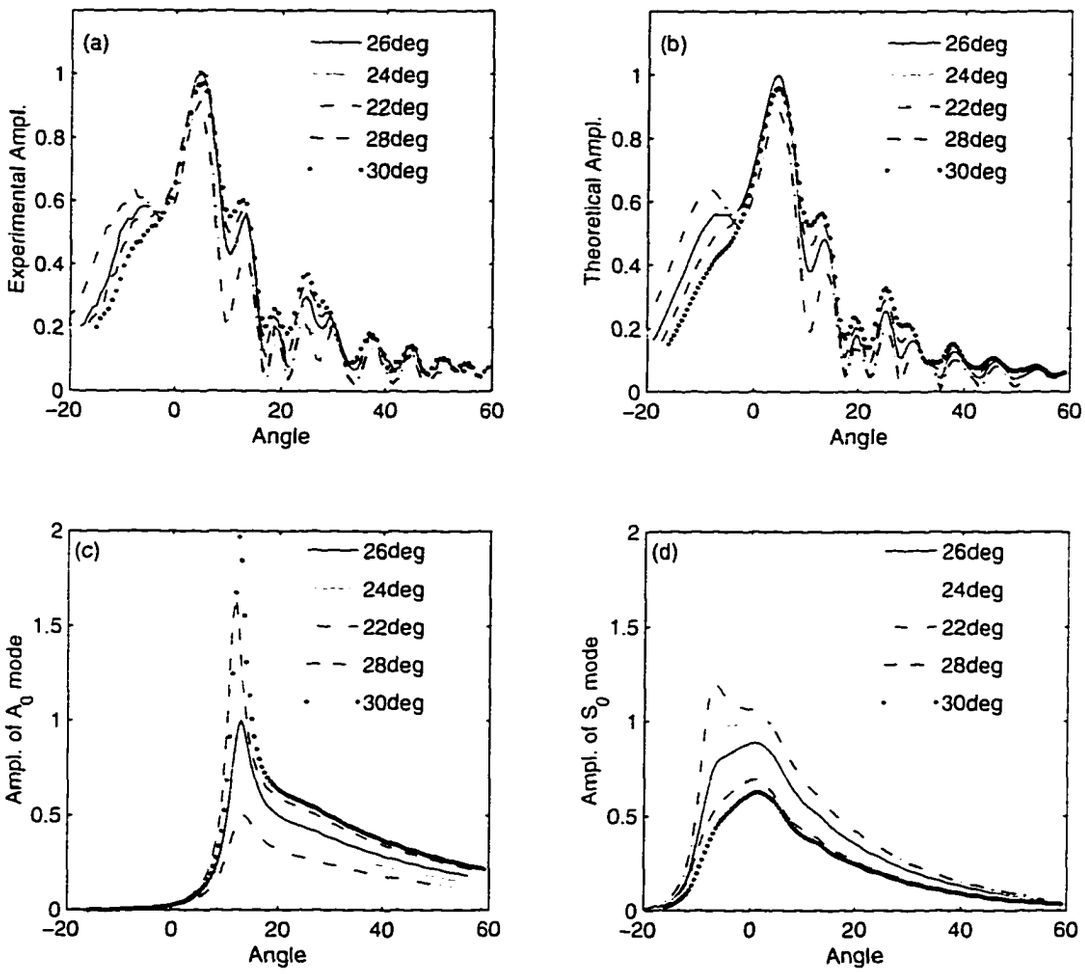

Figure 2.10 Transducer voltage for a steel shell in water: experimental data in (a), and theoretical voltage in (b) as a function of scan angle when $\mathcal{R}$ is aligned: $\theta_{\mathcal{R}} = \theta_{\mathcal{T}} = 26°$, and when it is misaligned: $26° \pm 2°$, and $26° \pm 4°$. For all plots, $\theta_{\mathcal{T}} = 26°$. The corresponding calculated profiles of the leaky A_0 mode (c) and S_0 mode (d) are shown for reference.

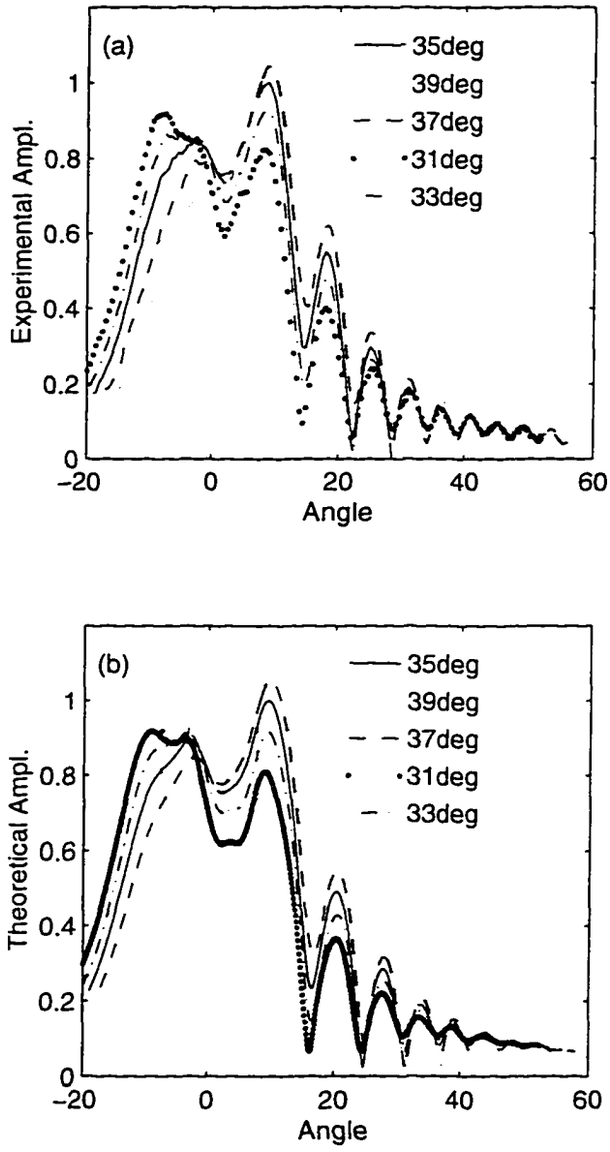

Figure 2.11 Transducer voltage for a steel shell in water: experimental data (a) and theoretical voltage (b) as a function of scan angle when $\mathcal{R}$ is aligned: $\theta_{\mathcal{R}} = \theta_{\mathcal{T}} = 35°$, and when it is misaligned: $35° \pm 2°$, and $35° \pm 4°$. For all plots, $\theta_{\mathcal{T}} = 35°$.

CHAPTER 3 TRANSMISSION COEFFICIENT RECONSTRUCTION BY USING AIR-COUPLED ULTRASOUND

A paper to be submitted to *IEEE Transactions on Ultrasonics, Ferroelectrics, and Frequency Control*

Han Zhang and D. E. Chimenti

Abstract

In this paper we present an air-coupled ultrasound transmission coefficient reconstruction strategy from a Gaussian sheet beam or from a rotationally symmetric Gaussian beam. The basic idea is to obtain the angular spectrum of the transmitted signal by performing a spatial Fourier transform on a narrowband experimental signal obtained from a scan of receiver coordinate. This operation reconstructs a function closely related to the transmission coefficient. It is shown using the complex transducer point that in the 2-D case, the function is exactly the plane-wave transmission coefficient. The sum of the angular spectra obtained at several incident angles forms a windowed reconstruction of the transmission coefficient. The transmission function reconstructed from a 3-D rotationally symmetric Gaussian beam is different from the plane wave transmission coefficient. As a demonstration elastic constants of isotropic and anisotropic materials are obtained from reconstructed transmission functions through an inversion algorithm operating on the experimental data.

Introduction

Lamb waves have been widely used in ultrasonic NDE to characterize material properties or assess material quality [1]. Of the previous work on materials using phase-matched fluid-loaded coupling, most has been performed in water-coupled testing [2]-[5]. With the development of efficient non-contacting ultrasonic air-coupled transducers [6]-[8], it has become feasible to apply air-coupled ultrasonic methods to NDE. Because of the low signal noise ratio resulting from the large impedance mismatch between the air and the solid object, most work of air-coupled (AC) ultrasound is qualitative, with defects in plates and C-scan imaging being the principal objects of study. As demonstrated by Safaeinili *et al* [9], however, it is possible to characterize elastic plates, both isotropic and anisotropic, by using AC ultrasound, despite the signal-to-noise ratio (SNR) penalty. Related to the present work are the measurements of Hosten, *et al.* [10] of the elastic constants of composites with bulk wave AC ultrasound. Nonetheless, there is little inversion of stiffensses in this concurrent work.

To characterize a material, we must be able to distinguish the effect on the experimental signal of the extrinsic conditions and intrinsic material properties.The former includes the geometry of the experimental setup, the size of the transducer, and its operating characteristics. The latter effect, the material properties, is what we are looking for. This task has motivated us to develop a theory that can model the entire experimental measurement and can be used to analyze all these factors. Beginning with an plane-wave decomposition of the incident beam and an application of the reciprocity theorem [13, 12], Lobkis *et al* [11] derived a formula for the receiving transducer voltage in a two-probe experimental setup. Through subsequent asymptotic evaluation of the resulting spectral integrals, a compact and convenient expression results.

It is possible, however, to simplify the construction of Gaussian acoustic beams by exploiting the advantages of the complex source point [14], or more generally the

complex transducer point (CTP) [15]-[19]. In this formalism the transducer beam is modeled as a quasi Gaussian beam simply by extending a real point source into the complex plane. This approach will be used here. Although the sidelobes characteristic of a piston radiator are not reproduced by a Gaussian beam, as demonstrated in [11], the combined directivity functions of two piston transducers is essentially identical to the product of two Gaussian beams, so the CTP provides an accurate model for the voltage calculation in a pitch-catch experimental setup.

The plane wave transmission or reflection coefficient is the physical parameter that carries information on the material properties. We can reconstruct the transmission coefficient either as a function of angle (alternatively, wavenumber) or as a function of frequency. Both allow for the inversion of the data to deduce properties of the plate. For most immersion testing the wideband nature of the piezoelectric transducer permits the simple measurement of reflection or transmission coefficients as a function of frequency [20]. Because of the inherent narrowband nature of the AC transducer, the method developed by Safaeinili *et al* [9], and extended in this paper, is to reconstruct the transmission coefficient as a function of angle at discrete frequencies by sampling the waveform in a quasi-infinite aperture. This method can be traced back to Sachse and Pao [21] who measured the group and phase velocity of dispersive Lamb wave by examining the phase spectrum, and it draws on the approach used by Alleyne and Cawley to characterize scattering from defects in plates [22]. The method employs a double Fourier transform of the received time-domain signal that leaks from the plate. Using it, we can determine the amplitude and velocity of any guided wave mode propagating in the plate.

In this chapter we will develop the extended model and demonstrate how it can be used with an efficient inversion scheme to reconstruct transmission coefficients with the framework of a 2-D and 3-D transmitter voltage calculation based on the CTP. The difference between results obtained from the 2-D and 3-D voltage calculations will be

shown. Extensive experiments, on both isotropic and anisotropic plates, together with a systematic theoretical analysis will be presented.

Theory

We begin the receiver voltage calculation with the Green's function in a unbounded medium, let us assume a point source is located at $\boldsymbol{r}' = (x', y', z')$, and a point receiver located at $\boldsymbol{r} = (x, y, z)$: then the Green's function is

$$G(\boldsymbol{r}) = \frac{e^{ik|\boldsymbol{r}-\boldsymbol{r}'|}}{4\pi|\boldsymbol{r}-\boldsymbol{r}'|} \tag{3.1}$$

and it satisfies the inhomogeneous Helmholtz equation

$$(\nabla^2 + k^2)G(\boldsymbol{r}) = -\delta(\boldsymbol{r}-\boldsymbol{r}'). \tag{3.2}$$

where $k = \omega/V$ is the wave vector and V is the acoustic velocity of the surrounding medium. Since the surrounding medium of our experiment is air, we will attach a subscript a to k and c to indicate that k_a and c_a are wavenumber and velocity in air.

The receiver voltage when the two transducers are facing each other can be obtained from the above Green's function by displacing the real point source and real point receiver into the complex plane.

$$\boldsymbol{r} \rightarrow \tilde{\boldsymbol{r}} = \boldsymbol{r} + i\boldsymbol{b} \tag{3.3}$$

$$\boldsymbol{r}' \rightarrow \tilde{\boldsymbol{r}}' = \boldsymbol{r}' + i\boldsymbol{b}' \tag{3.4}$$

where $\boldsymbol{b}$ and $\boldsymbol{b}'$ specify the transducer beam direction and the Fresnel length. b is related to the beam width w_0 at its waist by $w_0 = \sqrt{2b/k_a}$, similarly for b'. The voltage can be expressed as [19],

$$V_R(\tilde{\boldsymbol{r}};\tilde{\boldsymbol{r}}') = i\omega\rho\gamma(\omega)A_T A_R \frac{e^{ik_a|\tilde{\boldsymbol{r}}-\tilde{\boldsymbol{r}}|}}{4\pi|\tilde{\boldsymbol{r}}-\tilde{\boldsymbol{r}}|}. \tag{3.5}$$

where A_T and A_R specify the strength of the transmitter and receiver respectively. $\gamma(\omega)$ is a temporal spectrum of the transducer electronics. ρ is the density of the surrounding medium.

The interaction of the acoustic beam with the plate (shown in Fig. 3.1) can be synthesized from the spectral decomposition of the above complex Green's function weighted by the plane wave transmission coefficient

$$V_R(\alpha, x) = \frac{-1}{8\pi^2}\gamma(\omega)\omega\rho_f A_T A_R \int_{-\infty}^{\infty}\int_{-\infty}^{\infty} T(k_x, k_y) \times[\exp\{ik_x(\tilde{x}-\tilde{x}') + ik_y(\tilde{y}-\tilde{y}') + i\kappa_a(\tilde{z}-\tilde{z}')\}]/\kappa_a\, dk_x\, dk_y \tag{3.6}$$

where α is the transmitter and receiver angle, $\kappa_a = \sqrt{k_a^2 - k_x^2 - k_y^2}$. In the geometry shown in Fig. 3.1.

$$\boldsymbol{b} = (-b\sin\alpha, 0, -b\cos\alpha). \qquad \boldsymbol{b}' = (b\sin\alpha, 0, b\cos\alpha). \tag{3.7}$$

After substituting Eq. (3.7) into Eq. (3.4) we have for the complex receiver.

$$\tilde{x} = x - ib\sin\alpha. \quad \tilde{y} = y. \quad \tilde{z} = z - ib\cos\alpha. \tag{3.8}$$

and for the complex transmitter.

$$\tilde{x}' = x' + ib\sin\alpha. \quad \tilde{y}' = y'. \quad \tilde{z}' = z' + ib\cos\alpha. \tag{3.9}$$

To isolate the amplitude of the each Lamb mode, we treat the data by performing a spatial Fourier transform.

$$S(\theta, \alpha) = \frac{1}{2\pi}\int_{-\infty}^{\infty} V_R(x, \alpha)\exp(-ik_a\sin\theta\, x)\, dx \tag{3.10}$$

The transformed 2-D signal of the calculated voltage is different from that of a 3-D calculated voltage, so we will treat them separately.

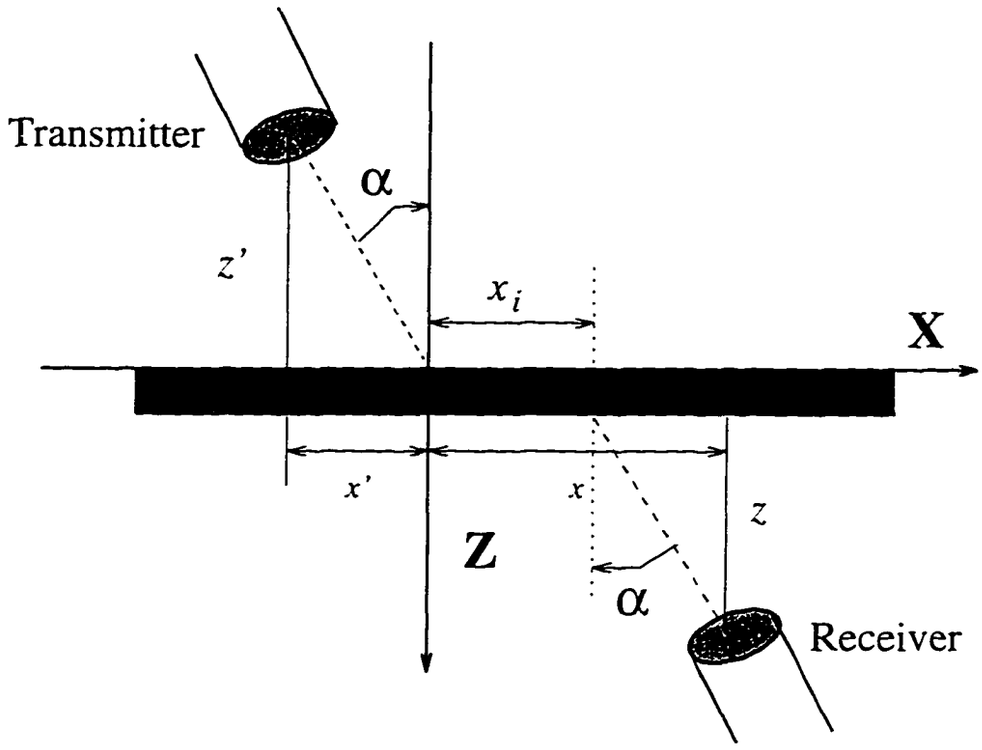

Figure 3.1 Schematic diagram of experimental transmission setup.

2-D Reconstruction

For the 2-D case, there is no dependence on y, so we let $k = k_x$ and $\kappa_a = \sqrt{k_a^2 - k^2}$, the voltage calculation formula Eq. (3.6) becomes

$$V_R(\alpha, x) = \frac{-1}{8\pi^2}\gamma(\omega)\omega\rho_f A_T A_R \int_{-\infty}^{\infty} T(k)\, \frac{\exp\{ik(\tilde{x} - \tilde{x}') + i\kappa_f(\tilde{z} - \tilde{z}')\}}{\kappa_f}\, dk\,. \qquad (3.11)$$

The transformed signal corresponding to Eq. (3.10) is

$$\begin{aligned} S(\theta, \alpha) &= \frac{1}{2\pi}\int_{-\infty}^{\infty} V_R(x, \alpha)\exp(-ik_a \sin\theta\, x)dx \\ &= \frac{-1}{16\pi^3}\gamma(\omega)\omega\rho_f A_T A_R \int_{-\infty}^{\infty} \exp(-ik_a \sin(\theta\, x)dx \\ &\quad \times \int_{-\infty}^{\infty} T(k)\frac{\exp\{ik(\tilde{x} - \tilde{x}') + i\kappa_f(\tilde{z} - \tilde{z}')\}}{\kappa_f}\, dk\,. \end{aligned} \qquad (3.12)$$

where the two integrals of the above equation can be performed as follows. Let I be the integral product

$$I = \int_{-\infty}^{\infty}\exp(-ik_a \sin\theta\, x)dx \int_{-\infty}^{\infty} T(k)\, \frac{\exp\{ik(\tilde{x} - \tilde{x}') + i\kappa_f(\tilde{z} - \tilde{z}')\}}{\kappa_f}\, dk. \qquad (3.13)$$

Then,

$$\begin{aligned} I &= \int_{-\infty}^{\infty} T(k)\, \frac{\exp\{-ik\tilde{x}' + i\kappa_f(\tilde{z} - \tilde{z}')\}}{\kappa_f}\int_{-\infty}^{\infty}\exp\{ik\tilde{x} - ik_a \sin\theta\, x\}\, dx \qquad (3.14) \\ &= \int_{-\infty}^{\infty} T(k)\, \frac{\exp\{-ik\tilde{x}' + i\kappa_f(\tilde{z} - \tilde{z}')\}}{\kappa_f} dk \int_{-\infty}^{\infty}\exp\{ik(x - ib\sin\alpha) - ik_a \sin\theta\, x\}\, dx \\ &= \int_{-\infty}^{\infty} T(k)\, \frac{\exp\{-ik\tilde{x}' + i\kappa_f(\tilde{z} - \tilde{z}') + kb\sin\alpha\}}{\kappa_f} dk \int_{-\infty}^{\infty}\exp\{ix(k - k_a \sin\theta)\}\, dx \\ &= \int_{-\infty}^{\infty} T(k)\frac{\exp\{-ik\tilde{x}' + i\kappa_f(\tilde{z} - \tilde{z}') + kb\sin\alpha\}}{\kappa_f}\, 2\pi\delta(k - k_a \sin\theta)dk \\ &= 2\pi\frac{T(k_a \sin\theta)}{k_a \cos\theta}\exp\{-ik_a \sin\theta\tilde{x}' + ik_a \cos\theta(\tilde{z} - \tilde{z}') + k_a b\sin\theta\sin\alpha\}\,. \end{aligned}$$

The final result is

$$\begin{aligned} S(\theta, \alpha) &= \frac{-1}{16\pi^3}\gamma(\omega)\omega\rho_f A_T A_R \frac{T(k_a \sin(\theta))}{k_a \cos\theta} \\ &\quad \times \exp\{-ik_a \sin\theta\tilde{x}' + ik_a \cos\theta(\tilde{z} - \tilde{z}') + k_a b\sin\theta\sin\alpha\}\,. \end{aligned} \qquad (3.15)$$

The expression in Eq. (3.15) is in fact a transmission coefficient weighted by the spatial Gaussian beam spectrum: to show this we will expand the exponential term of Eq. (3.15) below.

$$\begin{aligned}
& \exp\{-ik_a \sin\theta \tilde{x}' + ik_a \cos\theta(\tilde{z} - \tilde{z}') + k_a b \sin\theta \sin\alpha\}. \\
= \; & \exp\{-ik_a \sin\theta(x + ib\sin\alpha) + ik_a \cos\theta(z - ib\cos\alpha - z' - ib\cos\alpha) + k_a b \sin\theta \sin\alpha\}. \\
= \; & \exp\{-ik_a \sin\theta\, x + bk_a \sin\theta sin\alpha + ik_a \cos\theta(z - z') + 2k_a b \cos\theta \cos\alpha + k_a b \sin\theta \sin\alpha\}. \\
= \; & \exp\{-ik_a x \sin\theta + ik_a \cos\theta(z - z') + 2k_a bcos\theta \cos\alpha + 2k_a b \sin\theta \sin\alpha\}. \\
= \; & \exp\{-ik_a x \sin\theta + ik_a \cos\theta(z - z') + 2k_a b \cos(\theta - \alpha)\}. \qquad (3.16)
\end{aligned}$$

The amplitude of the above equation is

$$\begin{aligned}
\exp\{2k_a b\cos(\theta - \alpha)\} &= \exp\left\{2k_a b(1 - 2\sin^2(\frac{\theta - \alpha}{2}))\right\} && (3.17) \\
&\approx \exp(2k_a b)\exp\left\{-k_a b(\theta - \alpha)^2\right\} && (3.18)
\end{aligned}$$

Except for a constant term $e^{2k_a b}$. Eq. (3.15) is a plane wave transmission coefficient (expressed as a function of angle or wavenumber) multiplied by a Gaussian beam centered on the incident beam axis. Since the beam is well collimated. measurements at one incident angle recover only the part of the transmission spectrum which matches the incident beam spectrum. To recover the whole transmission spectrum. we must sum the spectra obtained at many incident angles. depending on the spectral width of the incident beam.

$$\begin{aligned}
T_s(\theta) &= \sum_{\alpha} S(\theta, \alpha) && (3.19) \\
&\approx \sum_{\alpha} 2\pi \frac{T(k_a \sin(\theta))}{k_a \cos\theta} \exp\{-ik_a \sin\theta \tilde{x}' + ik_a \cos\theta(\tilde{z} - \tilde{z}') + k_a b \sin\theta \sin\alpha\}.
\end{aligned}$$

where T_s is the sum of spectra at multiple values of α. and when T_s is normalized by the window function of the corresponding incident beams. it will be identical to the plane wave transmission coefficient. We will show this later.

If the scan over coordinate is finite, the integral in Eq. (3.10) is not equivalent to a Fourier transform with its infinite range of integration. Instead, an integration over a finite interval, such as from $-\xi$ to ξ, must be performed. Then, Eq. (3.12) becomes

$$\begin{aligned} S(\theta,\alpha) &= \frac{1}{2\pi}\int_{-\xi}^{\xi} V_{\mathcal{R}}(x,\alpha)\exp(-ik_a x\sin(\theta))dx \\ &= \frac{-1}{16\pi^3}\gamma(\omega)\omega\rho_f A_T A_{\mathcal{R}}\int_{-\xi}^{\xi}\exp(-ik_a x\sin(\theta))dx \\ &\quad\times\int_{-\infty}^{\infty}T(k)\,\frac{\exp\{ik(\tilde{x}-\tilde{x}')+i\kappa_f(\tilde{z}-\tilde{z}')\}}{\kappa_a}\,dk \\ &= \frac{-1}{16\pi^3}\gamma(\omega)\omega\rho_f A_T A_{\mathcal{R}} \\ &\quad\times\int_{-\infty}^{\infty}T(k)\frac{\exp\{-ik\tilde{x}'+i\kappa_f(\tilde{z}-\tilde{z}')+kb\sin\alpha\}\,[2\sin(\xi(k-k_a\sin\theta))]}{\kappa_a(k-k_a\sin\theta)}dk. \end{aligned} \tag{3.20}$$

In experiments the signal is weak enough beyond a certain scan range, so that we may regard the scan as infinite, and Eq. (3.15) gives very accurate results.

3-D Reconstruction

For a 3-D voltage calculation as suggested in Eq. (3.6), spherical coordinates would be more convenient, as in the Brekhovskikh's discussion on the reflection and refraction of spherical waves [23].

$$k_x = k_a\sin\theta_i\cos o_i,\quad k_y = k_a\sin\theta_i\sin o_i\quad k_z = \kappa_a = k_a\cos\theta_i, \tag{3.21}$$

and

$$\frac{1}{\kappa_a}dk_x\,dk_y = k_a\sin\theta_i d\theta_i do_i. \tag{3.22}$$

Also, we limit our study to the incident plane, so $\tilde{y}=\tilde{y}'=0$. Then Eq. (3.6) is modified to

$$\begin{aligned} V_{\mathcal{R}}(\alpha,x) &= \frac{-1}{8\pi^2}\gamma(\omega)\omega\rho_f A_T A_{\mathcal{R}}\int_0^{2\pi}\int_0^{\pi/2-i\infty}T(\theta_i,o_i) \\ &\quad\times\exp\{ik_a(\sin\theta_i\cos o_i(\tilde{x}-\tilde{x}')+\cos\theta_i(\tilde{z}-\tilde{z}'))\}\;k_a\sin\theta_i d\theta_i do_i \end{aligned} \tag{3.23}$$

Substituting Eq. (3.23) into Eq. (3.10) yields.

$$S(\alpha,\theta) = \frac{-1}{8\pi^2}\gamma(\omega)\omega\rho_f A_T A_R \frac{1}{2\pi}\int_{-\infty}^{\infty}\exp(-ik_a x\sin(\theta))\,dx\int_0^{2\pi}\int_0^{\pi/2-i\infty} T(\theta_i,o_i) \times \exp\{ik_a(\sin\theta_i\cos o_i(\tilde{x}-\tilde{x}')+\cos\theta_i(\tilde{z}-\tilde{z}'))\}\,k_a sin\theta_i d\theta_i do_i\,. \quad (3.24)$$

Similar to the 2-D case, the integration over x produces a Dirac δ function.

$$S(\alpha,\theta) = \frac{-1}{8\pi^2}\gamma(\omega)\omega\rho_f A_T A_R \int_0^{2\pi}\int_0^{\pi/2-i\infty} T(\theta_i,o_i) \times \exp\{-ik_a(\sin\theta_i\cos o_i\tilde{x}'+\sin\theta_i\cos o_i b\sin\alpha+\cos\theta_i(\tilde{z}-\tilde{z}'))\} \times\delta(k_a\sin\theta_i\cos o_i - k_a\sin\theta)k_a\sin\theta_i d\theta_i do_i\,. \quad (3.25)$$

We first perform the integration over o_i: in order to simplify our analysis, however, we assume for now that the transmission coefficient is independent of o_i. Then, the transformed signal reduces to

$$S(\alpha,\theta) = \frac{-1}{8\pi^2}\gamma(\omega)\omega\rho_f A_T A_R \exp\{-ik_a\sin\theta\tilde{x}'+k_a b\sin\theta\sin\alpha\} \times\int_\theta^{\pi/2-i\infty}\exp\{ik_a\cos\theta_i(\tilde{z}-\tilde{z}')\}\frac{T(\theta_i)\sin\theta_i}{\sqrt{(\sin^2\theta_i-\sin^2\theta)}}d\theta_i. \quad (3.26)$$

To remove the radical in the denominator of the above integral, we perform the following change of integration variables.

$$\cos\theta\cos\beta = \cos\theta_i\,. \quad (3.27)$$

Since $\theta_i : \theta\to\frac{\pi}{2}-i\infty$, $\beta : 0\to\frac{\pi}{2}-i\infty$, the integration over θ_i in Eq. (3.29) becomes an integration over β

$$S(\alpha,\theta) = \frac{-1}{8\pi^2}\gamma(\omega)\omega\rho_f A_T A_R \exp\{-ik_a\sin\theta\tilde{x}'+k_a b\sin\theta\sin\alpha\} \quad (3.28)$$
$$\times\int_0^{\pi/2-i\infty}\exp\{ik_a\cos\theta\cos\beta(\tilde{z}-\tilde{z}')\}\,T(\cos^{-1}(\cos\theta\cos\beta))d\beta\,.$$

The integration variable in the formula above can be generalized to a complex value, and the integration path can be deformed from the real axis into a steepest-descent path

(SDP) and evaluated at the saddle point of the integrand, with proper consideration of the pole along the new integration contour path [17, 19]. The radiation condition assures that the contribution on the contour at infinity will vanish. The result of these actions is a uniform asymptotic evaluation.

$$\begin{aligned} S(\alpha,\theta) &= \frac{-1}{8\pi^2}\gamma(\omega)\omega\rho_f A_T A_R \\ &\times \exp\{ik_a(\cos\theta(\xi-\xi')-\sin\theta\tilde{x}')+k_a b\sin\theta\sin\alpha\}\sqrt{\frac{2\pi}{ik_a\cos\theta(\xi-\xi')}} \\ &\times\left\{T(\theta)+\sum_{j=1}^{M} iRes[T(\theta_{p_j})]\frac{1}{2}\sqrt{\frac{\cos\theta}{\cos\theta-\cos\theta_{p_j}}}(1+i\sqrt{\pi}\tilde{S}_{p_j}\Omega(\tilde{S}_{p_j}))\right\}. \end{aligned} \tag{3.29}$$

where $\Omega(\tilde{S}_{p_j}) = \mathrm{erfc}(-i\tilde{S}_{p_j})\exp(-\tilde{S}_{p_j}^2)$ and $\tilde{S}_{p_j} = \sqrt{ik_a(\cos\theta-\cos\theta_{p_j})(\xi-\xi')}$ is the "numerical distance" between the saddle point and pole. The term in the curly brackets in Eq. (3.30) is the reconstructed transmission coefficient T_r. We have

$$T_r(\theta) = T(\theta)+\sum_{j=1}^{M} i\mathrm{Res}[T(\theta_{p_j})]\frac{1}{2}\sqrt{\frac{\cos\theta}{\cos\theta-cos\theta_{p_j}}}(1+i\sqrt{\pi}\tilde{S}_{p_j}\Omega(\tilde{S}_{p_j})). \tag{3.30}$$

If we now assume that the transmission coefficient depends on o_i, from the Dirac δ function in Eq. (3.25) we know that o_i is related to o_T through

$$\cos o_T = \frac{\sin\theta}{\sin\theta_i} = \frac{\sin\theta}{\sqrt{1-\cos^2\theta_i}} = \frac{\sin\theta}{\sqrt{1-\cos^2\theta\cos^2\beta}}. \tag{3.31}$$

The last step follows from the definition of the integration variable β in Eq. (3.27): after some simple algebraic manipulations, we have

$$\tan(o_T) = \pm\cot\theta\sin\beta. \tag{3.32}$$

With this change the integral in Eq. (3.29) becomes

$$\begin{aligned} S(\alpha,\theta) &= -\frac{1}{8\pi^2}\gamma(\omega)\omega\rho_f A_T A_R \exp\{-ik_a\sin\theta\tilde{x}'+k_a b\sin\theta\sin\alpha\} \\ &\times\int_0^{\frac{\pi}{2}-i\infty}\exp\{ik_a\cos\theta\cos\beta(\xi-\xi'))\} \\ &\times T(\arccos(\cos\theta\cos\beta),\pm\arctan(\cot\theta\sin\beta))\,d\beta. \end{aligned} \tag{3.33}$$

Here, we see that the integration becomes a symmetric sum of terms with $o_0 + o$ and $o_0 - o$. For most real solids examined in a fluid such as water the error incurred by ignoring this contribution to the integral will be negligible. For anisotropic composite materials, particularly uniaxial laminates tested in air, however, the difference from accounting for the integrations in $\pm\phi$ can be substantial [28].

Experimental Procedure

In this section we will describe our experimental apparatus, sample preparation, and data acquisition and processing.

Experimental Samples

Plexiglas, as an isotropic material on which to test our AC methods, is an ideal experimental material because of its low density and low acoustic velocity and thus low acoustic impedance. The experiment results with Plexiglas show a high signal noise ratio. The anisotropic plates used in our experiments are a uniaxial graphite-epoxy laminate, a biaxial graphite-epoxy laminate, and a quasi-isotropic graphite-epoxy plate. The 0.92-mm uniaxial graphite-epoxy plate is composed of Ciba-Geigy 914 epoxy and Thornel T300 high-modulus graphite fibers. The fiber volume fraction is 0.65 with an average fiber diameter about $7\mu m$. The density of the plate is 1.6 g/cm^3. The biaxial and quasi-isotropic plates are fabricated from Hercules AS/4 fibers and 3501 epoxy. Fiber volume fraction is between 0.64-0.67. The biaxial plate has a stacking sequence $[0,90]_{3s}$ with 12 plies. The overall thickness and density are 1.52 mm and 1.62 g/cm^3. The quasi-isotropic plate has a stacking sequence $[0/\pm 45,90]_{2s}$ with a total of eight plies. The overall density and thickness are 1.61 g/cm^3 and 2.08 mm.

Experimental Apparatus

Two capacitance transducers are used to excite and receive AC ultrasound. They have an effective radius of 5 mm and a center frequency of 0.7 MHz with a usable response from 0.1 MHz to about 1.5 MHz. A Parker-Daedel positioning system is used for the scans performed here. The scanning system has a resolution of 0.01 mm. The transducers are mounted on precision rotary stages with a usable angular resolution of 0.01°. Figure 3.2 is a schematic diagram of the experiment setup. The high voltage tone burst of 10 to 20 cycles with frequency from 0.2 MHz to 1.5 MHz produced by a RITEC tone burst generator model RAM 10000 is first sent to a capacitively coupled circuit that permits the establishment of a high voltage dc bias on the transmitter. A circuit diagram is shown in Fig. 3.3 that safely raises the rf ground to 350 V. The tone burst is then applied over this bias to the transmitter. The reflected or transmitted signal is detected by an identical capacitive foil receiver and fed to a Cooknell CA6/C charge preamplifier and bias circuit. The receiver signal is further amplified by a broadband RITEC amplifier, and the rf signal is sent to Lecroy 9304 oscilloscope to be digitized. The Lecroy is triggered by the RITEC high-power generator trigger signal after it has been delayed in a SRS DS352. The digital delay, scan system, and the Lecroy scope are under DEC workstation control through the IEEE instrument bus. The digitized waveform from the Lecroy is sent to the DEC work station for further processing.

Data Acquisition and Processing

The data acquisition is performed by Lecroy 9304, we also take advantage the sequence mode of data acquisition of Lecroy to speed up waveform averaging and acquisition. The sequence mode is 6 times faster than the normal averaging while getting the same signal noise ratio. After the digitized waveform is sent to the work station, we first perform a FFT on the time domain signal. Several selected frequency components are

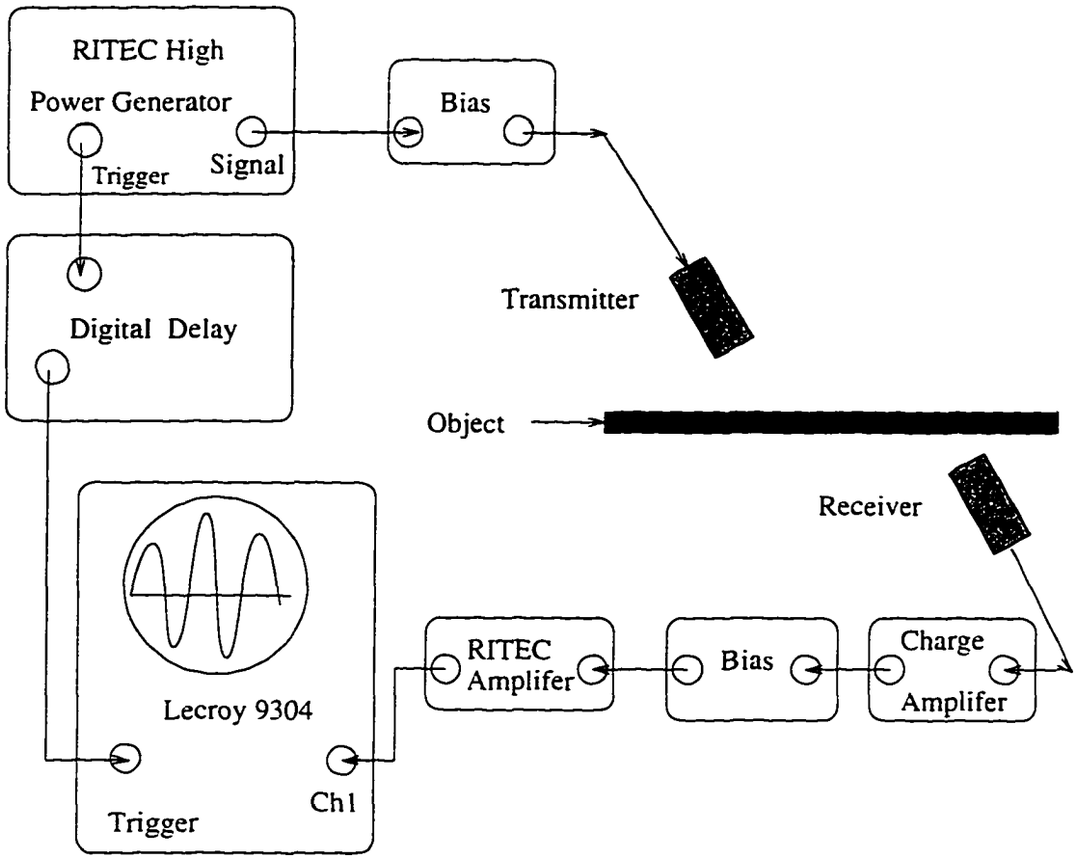

Figure 3.2 Block diagram of the experiment.

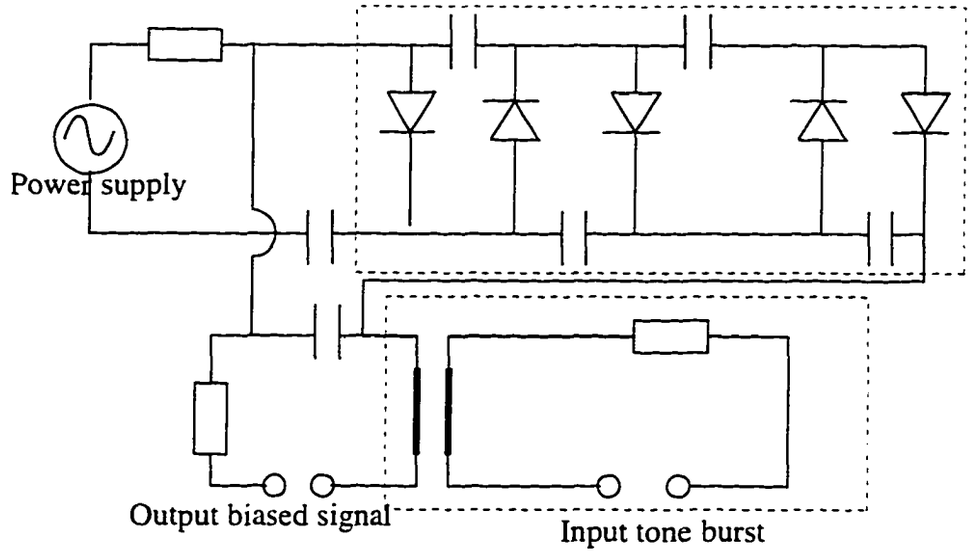

Figure 3.3 Diagram of capacitance foil bias circuit.

recorded at each scan position. A spatial Fourier transform is then performed to convert the selected frequency component to an angular spectrum. The sum of the spectrum of different incident angles is then normalized by the window function and we get the reconstructed transmission coefficient. The window function can be obtained under the same condition as the above experiment without the objects.

Results and Discussions

To verify our theoretical model, we have performed several experiments and compared these to the theoretical predictions. As mentioned earlier, in order to reconstruct the transmission coefficient the summed signal has to be normalized by a window function which can be obtained through the same procedure as the transmission experiment, except with no plate. This experiment is essentially a transducer voltage measurement. Shown in Fig. 3.4(a) is x-scan data with an incident angle 0°, *i.e.* the transducers are normal to the scan direction. The solid curve is the experiment, and the dashed curve is the calculated result from Eq. (3.5): the theoretical curve can also be calculated from Eq. (3.6) with a transmission coefficient of unity, either evaluated asymptotically [17] or by direct integration. All predictions lead to the same calculated results. Shown in Fig. 3.4(b) is the transformed signal of (a) using Eq. (3.10). The solid curve is obtained by performing a numerical Fourier transform on the experimental results shown in (a), while the theoretical curve is calculated from Eq. (3.15) with a unity transmission coefficient. As we can see the voltage in the spatial domain and in wavenumber space (or equivalently the angular spectrum), both have Gaussian characteristics, and they are reciprocal to each other. That means the increase of beam width in the spatial domain results in the decrease of beam width in wavenumber space (or a narrower angular spectrum).

Shown in Fig. 3.4(c) and (d) are the same results as above, but obtained at an incident

angle of 15°. Note in (c) that the origin is defined as the intersection of transmitter beam axis with the receiver scan line, so we see no change in (c) compared with (a), while the center of the angular spectrum moves to 15°. This behavior is consistent with Eq. (3.18). As the incident angle increases, the angular spectrum shifts and is always centered on the incident beam axis defined by the incident angle. We also find no side lobes in the x-scan data, which can be verified by the monotonic decrease of the voltage amplitude away from the center beam axis. This observation further supports our original assumption that the combined Gaussian directivity function is an accurate representation of the combined piston transducer directivity function, when identical devices are used in a pitch-catch setup, even for the capacitance transducers used here. The transformed experiment data in Fig. 3.4(b) and (d), however, show some oscillations. We believe these result from either the rectangular aperture window or the finite x scan performed in the experiment with sharp cutoff of the data. The theoretical curves in Fig. 3.4(b) and (d) do not predict sidelobes because they are calculated from Eq. (3.10), which assumes an infinite scan range and an infinite aperture window. Certainly, if we perform a numerical Fourier transform on the theoretical data shown in Fig. 3.4(a) and (c), we would obtain the same behavior as in the experimental data. These same effects are also observed in the theoretical curves if we perform the Fourier transform according to Eq. (3.21).

To construct the window function, we sum the spectra of several incident angles, as shown in Fig. 3.5. The solid curve is the theoretical calculation, and the dashed curve is the experiment. The window function rises slightly with increasing incident angle, as expected according to the term $k_a \cos\theta$ in the denominator of Eq. (3.15).

The experimental data are obtained by inserting the plate between the two transducers, as shown in Fig. 3.1 and performing the coordinate scans as described above. Shown in Fig. 3.6 is the transmitted signal of a Plexiglas plate calculated from Eq. (3.11). For solid curve, the incident angle of 15° lies between two lamb-mode phase matching angles.

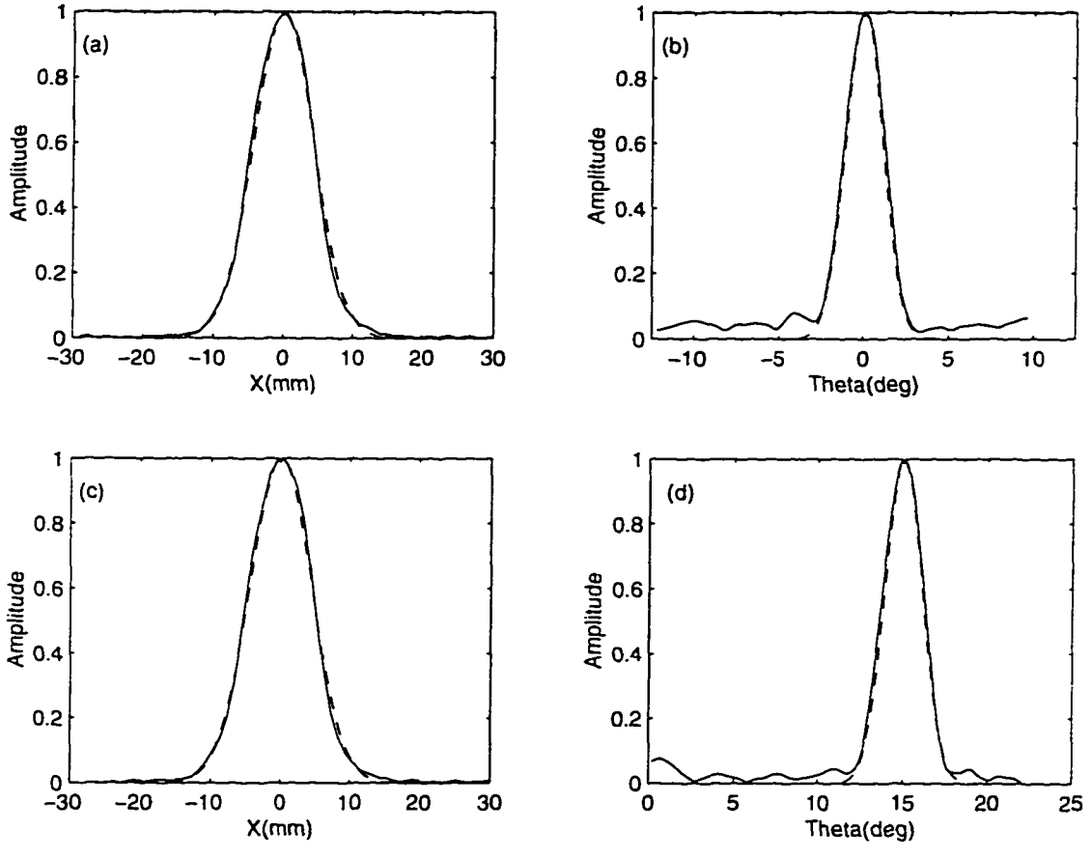

Figure 3.4 Experimental beam scans in coordinate and angle. (a) and (b) are x-scan data at an incident angle of 0° and 15°, respectively. (c) and (d) are the corresponding angular spectra. In all these graphs the solid curves are the experimental data, and the dashed curves are the theoretical calculations.

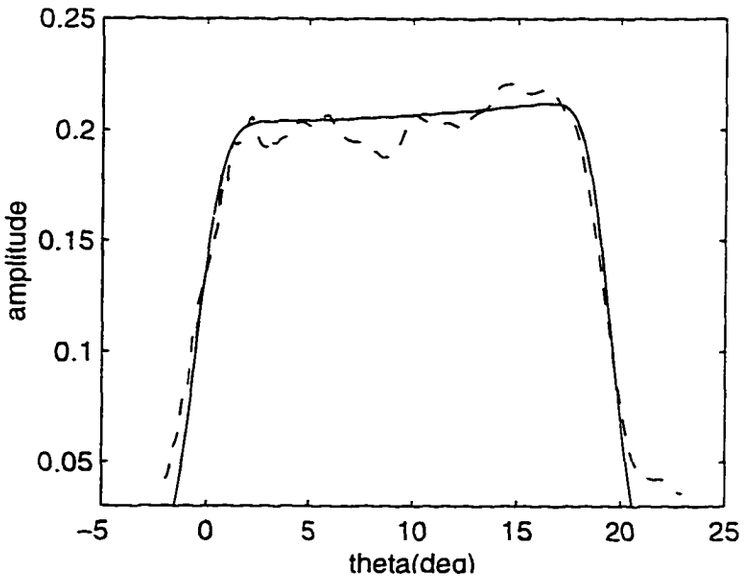

Figure 3.5 Window produced by summing the angular spectra of several incident angles with no plates. Solid curve is theoretical calculation, and dashed curve is experiment.

so both modes are excited, as can be confirmed by observing the interference beyond $x = 20$ mm. For an incident angle of 8.5°, only one mode is excited, and a monotonic decrease beyond $x = 20$ mm is observed. This feature reminds us of our previous study on nonspecular reflection in planar structures [25]. Unlike the reflection case, however, where the receiver voltage is an interference of the specular reflection and one or two Lamb wave modes, what we observe here in transmission is the pure Lamb wave, where the voltage shown in Fig. 3.6 is similar to the leaky wave calculation in [25].

The angular spectra calculated from synthetic data for the scans detailed above are shown in Fig. 3.7(a). The solid curve is the Fourier transform of the theoretical finite scan shown in Fig. 3.6, while the dashed line is the result calculated from Eq. (3.15) which assumes an infinite scan. A careful examination of the plots shows that the solid curve has some very small oscillations in the tails of the distribution. The dip between the two modes is also slightly deeper. These differences arise from the finite nature of the

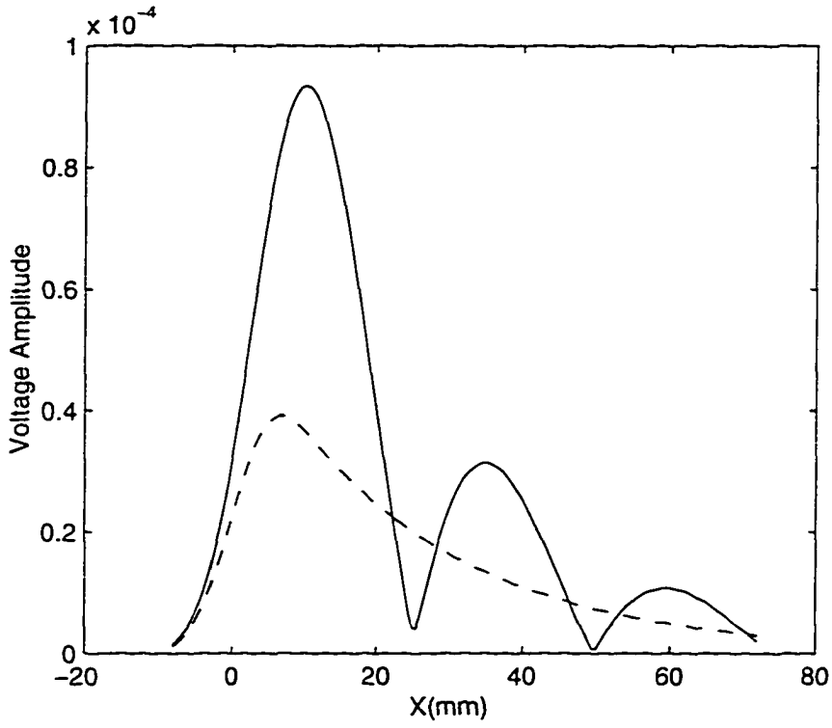

Figure 3.6 Synthetic transmitted signal calculated from Eq. (3.11) (using the plane-wave transmission coefficient) for a Plexiglas plate at an incident angle of 15° (solid curve) and 8.5° (dashed curve) as a function of scan coordinate x.

scan, similar in origin to the oscillation observed in Fig. 3.4. The Fourier transform of the finite scan yields a sinc function (Eq. (3.21)) instead of a Dirac δ function. Figure 3.7 illustrates the physical significance of Eq. (3.15). The angular spectrum of incident beam around the incident angles is superimposed on the plane-wave transmission coefficient, and the two scans with incident angles of 8.5° and 15.5° recover only the portion of the transmission coefficient which is subtended by the incident beam angular spectrum.

We now combine the spectra at several incident angles by summing to recover a function related to the transmission coefficient. Such a verification is shown in Fig. 3.8. The sum of 20 spectra at different incident angles from 1° to 20° calculated from Eq. (3.20) is shown in Fig. 3.8(b) as dash-dotted curve, while the solid curve is the plane wave transmission coefficient. In order to make a direct comparison, both of them are normalized by their maximum value. A small difference appears at lower phase matching angles and can be explained by the effect of the aperture window shown in Fig. 3.5. The slope of the window at the lower phase matching angle reduces slightly the amplitude of the transmitted signal. In order to reconstruct the plane-wave transmission coefficient completely, the transmitted signal must be normalized by the corresponding aperture window under the same experimental conditions. This conclusion is confirmed by the results shown in Fig. 3.8(a). The solid curve is the transmission coefficient. The dashed line is the transmitted signal normalized by the window in Fig. 3.5, and it corresponds exactly to the plane-wave transmission coefficient.

Although the sum of 2-D calculated voltage spectra for an infinite, window-normalized coordinate scan is identical to the plane-wave transmission, the 3-D voltage calculation shows this equality no longer holds, even for an infinite scan. Shown in Fig. 3.9 is a comparison between a 3-D normalized spectral sum and the plane-wave transmission coefficient. The difference is obvious, especially at low phase matching angles. The origin of the disparity can be explained by an examination of the wavevector geometry. According to Eq. (3.25) it is the wavevector satisfying $k_a \sin\theta_i \cos o_i = k_z \sin\theta$ or

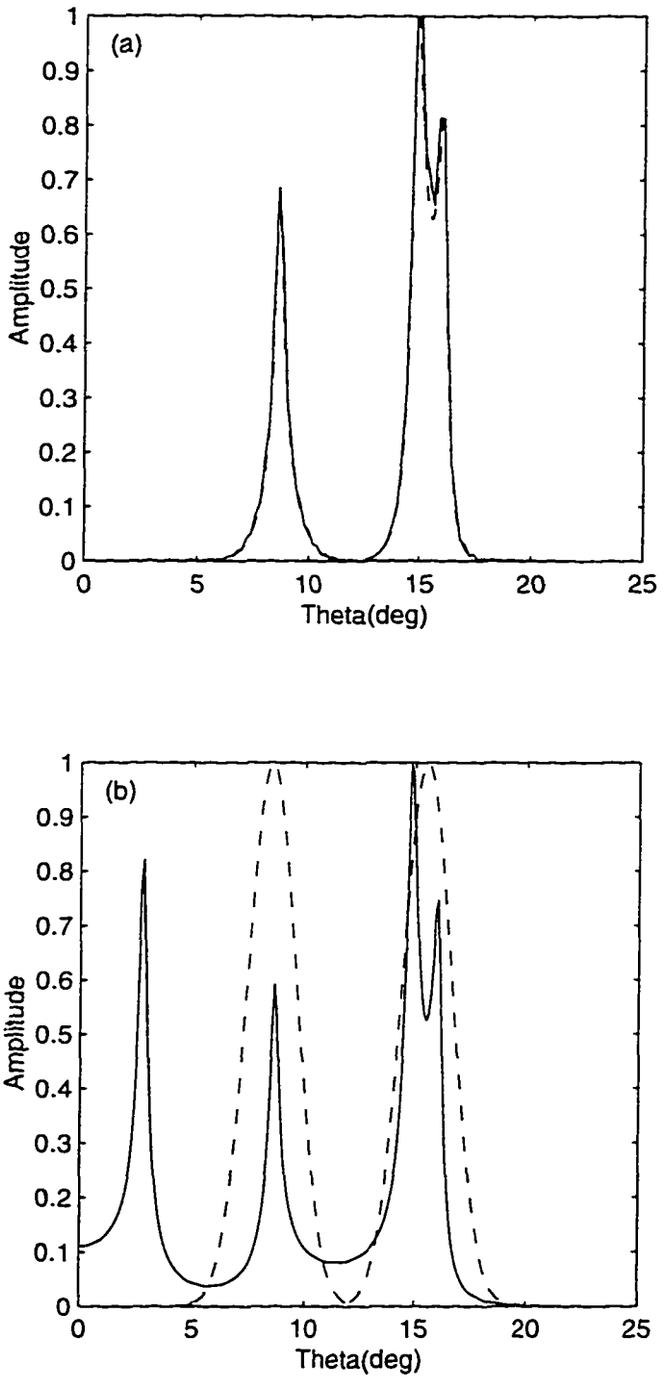

Figure 3.7 (a) Comparison of angular (spatial) spectra (solid curve) of the x-scan data at incident angles of 8.5°(first sharp peak) and 15.5°(second two peaks) in Fig. 3.6 and a direct calculation (dashed curve) using Eq. (3.15): (b) a physical illustration of Eq. (3.15).

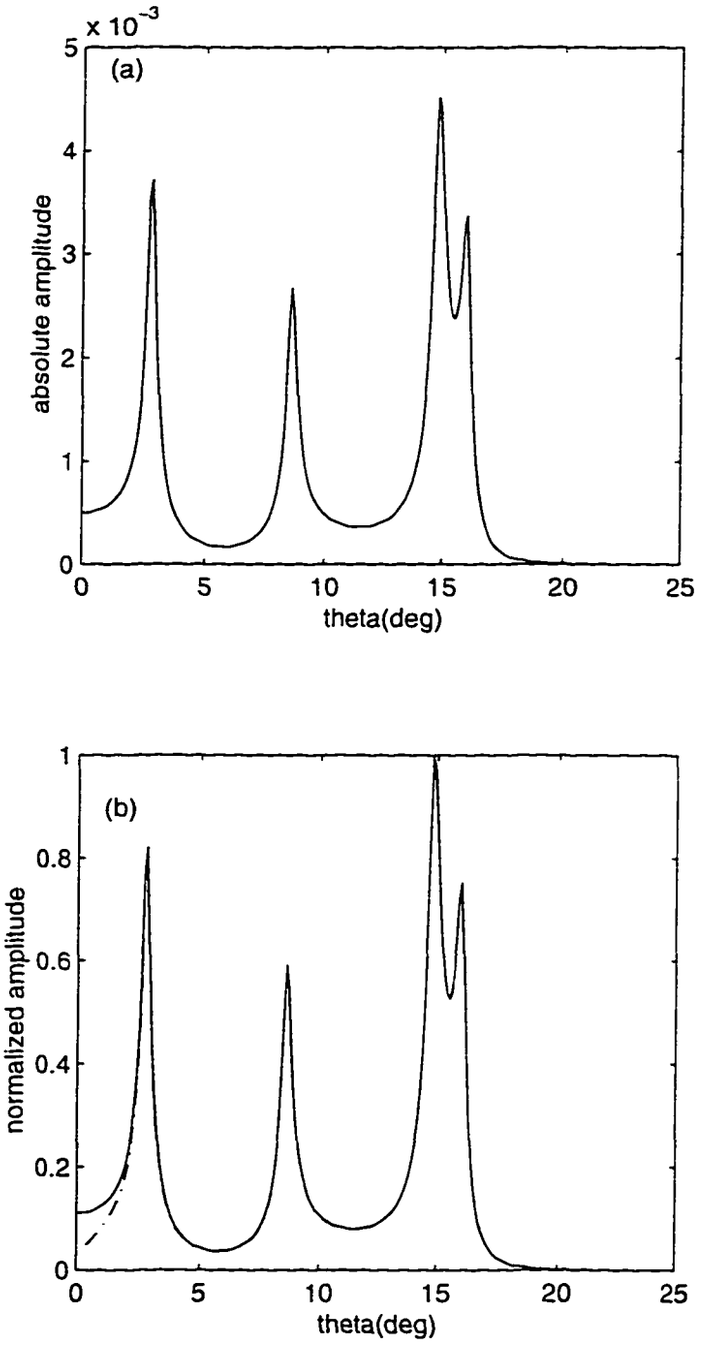

Figure 3.8 Comparison of the transmission function reconstructed from synthetic data and the plane wave transmission coefficient. (a) Plane wave transmission coefficient (solid curve) and 2-D synthetic transmitted signal normalized by the window (dashed curve): (b) Transmission coefficient (solid line) and the 2-D synthetic transmitted signal not normalized by the window in Fig. 3.5.

$\sin\theta_i = \sin\theta/\cos o_i$ that makes a contribution to the voltage: when θ is smaller, the range of o_i will be larger, and the effects of o_i will also be more significant. We also note that the difference is larger near Lamb mode phase matching angles. This fact can be attributed to the inverse dependence of the numerical distance $\tilde{S}_{p_j}$ on the disparity. As defined in Chapter 1 and earlier in this chapter, the numerical distance is a measure of the approach of the saddle point to the pole in the complex plane within the context of the asymptotic evaluation of the spectral reflection integrals.

We have

$$\begin{aligned}\tilde{S}_{p_j} &= \sqrt{k_a(\cos\theta - \cos\theta_{p_j})(z - z')} \\ &= \sqrt{ik_a 2\sin\left[\frac{\theta+\theta_{p_j}}{2}\right]\sin\left[\frac{\theta-\theta_{p_j}}{2}\right](z-z')}.\end{aligned}$$

where $\tilde{S}_{p_j}$ attains a minimum value when θ is close to θ_{p_j}. If we assume $\theta p_j = \Re(\theta_{p_j}) + i\Im(\theta_{p_j})$, then

$$\tilde{S}_{p_j} \approx \sqrt{ik_a \sin\Re(\theta_{p_j})\Im(\theta^I_{p_j})(z-z')}.$$

where $\tilde{S}_{p_j}$ is large for large Lamb mode phase matching angle ($\Re(\theta_{p_j})$) or for large mode leakage ($\Im(\theta_{p_j})$), and thus we find better agreement between the reconstructed transmission coefficient and the plane wave transmission coefficient. On the other hand, $\tilde{S}_{p_j}$ can also increase for large values of $z - z'$. In fact, as $\tilde{S}_{p_j}$ goes to infinity, from the asymptotic evaluation of the error function [26], we have

$$\mathrm{erfc}(\gamma) \approx \frac{\exp(-\gamma^2)}{\sqrt{\pi}\gamma}\left\{1 + \sum_{n=1}^{\infty}(-1)^n \frac{1\times 3\times\ldots\times(2n-1)}{(2\gamma^2)^n}\right\}. \; |\gamma| >> 1, |\arg\{\gamma\}| < \frac{3\pi}{4}. \tag{3.34}$$

When $\Im(\tilde{S}_{p_j}) > 0$, then

$$\begin{aligned}&1 + i\sqrt{\pi}\tilde{S}_{p_j}\Omega(\tilde{S}_{p_j}) \\ &= 1 + i\sqrt{\pi}\tilde{S}_{p_j}\exp(-\tilde{S}^2_{p_j})\mathrm{erfc}(-i\tilde{S}_{p_j})\end{aligned}$$

$$\approx 1 + i\sqrt{\pi}\tilde{S}_{p_j}\exp(-\tilde{S}_{p_j}^2)\frac{exp(\tilde{S}_{p_j}^2)}{\sqrt{\pi}(-i\tilde{S}_{p_j})}$$
$$= 0.$$

and when $Im(\tilde{S}_{p_j}) < 0$. then

$$1 + i\sqrt{\pi}\tilde{S}_{p_j}\Omega(\tilde{S}_{p_j})$$
$$= 1 + i\sqrt{\pi}\tilde{S}_{p_j}\exp(-\tilde{S}_{p_j}^2)(2 - \mathrm{erfc}(+i\tilde{S}_{p_j}))$$
$$\approx 1 + 2i\sqrt{\pi}\tilde{S}_{p_j}\exp(-\tilde{S}_{p_j}^2) - i\sqrt{\pi}\tilde{S}_{p_j}\exp(-\tilde{S}_{p_j}^2)\frac{\exp(\tilde{S}_{p_j}^2)}{\sqrt{\pi}(i\tilde{S}_{p_j})}$$
$$\rightarrow 0.$$

In either case. the second term in the parenthesis of Eq. (3.30) will vanish as the transducers are moved far away from the object. and the reconstructed transmission coefficient will be identical to the plane wave transmission coefficient. This conclusion can be reached by an extreme example shown in Fig. 3.10 where the comparison of a plane wave transmission coefficient (dashed line) and a 3-D voltage calculation (solid line) is shown. assuming that the distance from either transducer to the objects is 800 mm. The reconstructed transmission coefficient using the 3-D voltage method approaches the plane wave transmission coefficient.

Since the 2-D Gaussian beam used here can also be regarded as a 3-D Gaussian sheet beam. the previous claim that the transmission coefficients reconstructed using the 2-D voltage and 3-D voltage methods are different may not so accurate. The difference arises from a comparison between a Gaussian sheet beam and a rotationally symmetric Gaussian beam. For a Gaussian sheet beam. the rays that lie outside the incident plane are still parallel to the inplane rays. so their contributions at all incident angles are uniform. and the rays out of the incident plane contribute only a multiplicative factor. Recall that the spatial Fourier transform extracts a wavevector spectrum from the x-scan data. At any particular incident angle. only the rays in the incident beam whose projection along the x-axis match a certain wavevector make a contribution to that

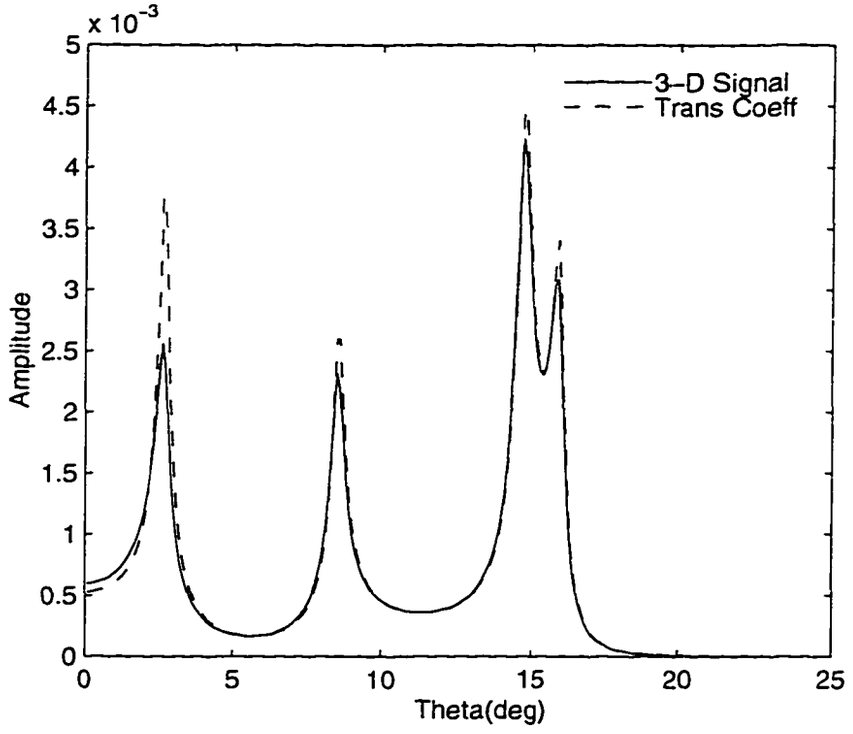

Figure 3.9 Comparison of plane wave transmission coefficient (dashed curve) and reconstructed transmission coefficient from 3-D voltage calculation when the distance from the transducers to the object is 30 mm.

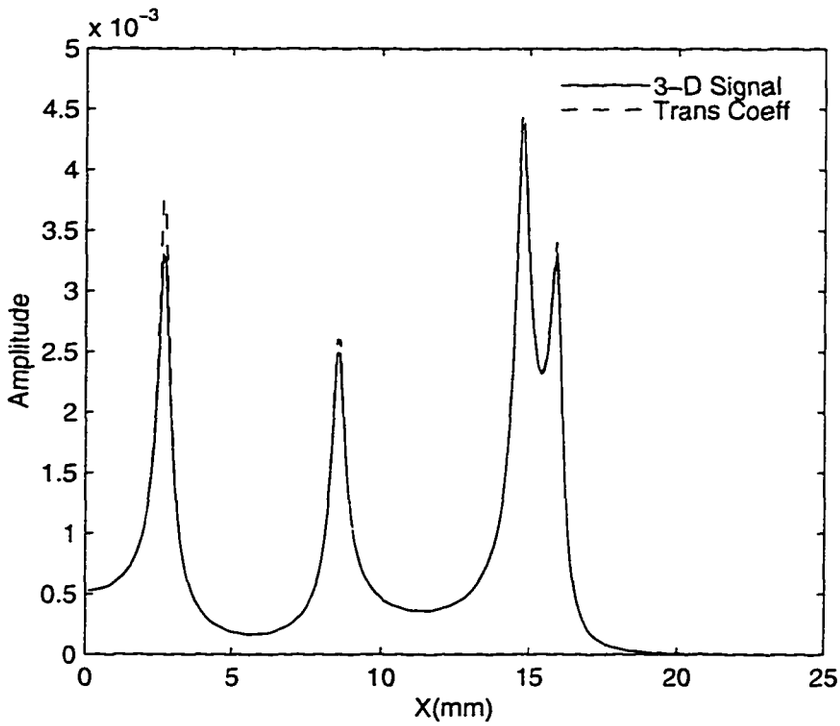

Figure 3.10 Comparison of plane-wave transmission coefficient (dashed curve) and reconstructed transmission coefficient from 3-D voltage calculation when the distance from the transducers to the object is 800 mm.

wavevector in the final reconstructed transmission coefficient. The projection of those rays out of the incident plane onto the x-axis for a rotationally symmetric Gaussian beam is certainly different from the inplane ray and this difference depends on the phase match angle. For the sheet beam, no ray has a nonzero projection out of the plane of incidence.

In summary, any differences between the plane-wave transmission coefficient and the reconstructed transmission function arise from two principal causes: one is the finite x-scan, and the other is diffraction of real 3-D beams. The finite scan has an effect similar to the finite window function discussed in digital signal processing. The error resulting from the finite scan is actually very small in most cases and is not our main focus. In the following experiments and the inversion procedure we will pay particular attention to the effects of beam diffraction on the transmission function.

All inversion procedures in essence are optimizations which infer the unknown parameters by minimizing some objective function F, which can be defined as the difference between the experimental data and an existing theoretical model. If the experimental data points in our experiments are represented by an array Y, then one useful and common definition of the objective function is simply the sum of the squared error,

$$F(C_{ij}^{*}, \theta) = \sum_{n} (T_r(\theta_n) - Y(n))^2. \tag{3.35}$$

where $T_r(\theta_n)$ is the reconstructed transmission function defined by Eq. (3.30) and evaluated at discrete angles θ_n. Note that $T_r(\theta_n)$ contains the material parameters C_{ij}^{*}. Many optimization procedures have been developed to perform the minimization of functions such as F defined here [29]. A complete review and a discussion of the merit of these algorithms is beyond the scope of this paper. Instead, we choose the Simplex, Powell, and Hooke & Jeeves method for our optimization solution.

We begin our experiments with an isotropic material, a plate of Plexiglas, or poly methyl methacrylate. As mentioned earlier, its low acoustic impedance make it ideal

for air-coupled experiments, and this fact can be seen from the low noise floor in the experimental data shown in Fig. 3.11 (solid curve). In frame (a) the experimental data are fitted with the reconstructed 3-D voltage transmission function which is represented as a dashed curve. The best fit gives $c_l = (2.74, -0.03)$ and $c_t = (1.38, -0.018)$ for the real and imaginary parts of the two velocities in km/sec. The same set of data can also be fitted with plane wave transmission by using the same algorithm, which gives $c_l = (2.74, -0.063)$ and $c_t = (1.38, -0.018)$ in km/sec, and is also represented by a dashed curve in frame (b). We see that the only difference is in the imaginary part of c_l. The reconstructed transmission functions have the same peak positions as the plane-wave transmission coefficient, since these are determined by the real parts of c_l and c_t.

We've already seen that beam diffraction can have a strong effect on the amplitude of the reconstructed transmission function at low phase matching angle. The amplitude of the transmitted signal at low phase matching angle is crucial for determining the imaginary part of c_l. This point is illustrated in Fig. 3.12. In frame (a) the solid curve is the transmission coefficient calculated by assuming $c_l = (2.74, -0.063)$ and $c_t = (1.38, -0.018)$. The dashed curve is the transmission coefficient after $\Im\{c_l\}$ is reduced by 50%. Large differences exist only in the A_1 mode, in contrast to frame (b), where a 50% reduction in $\Im\{c_t\}$ (dashed curve) causes huge differences at both the A_0 and S_0 modes. The amplitude of the transmission coefficient at low phase matching angles determines $\Im\{c_l\}$ and the amplitude at high phase matching angles determines $\Im\{c_t\}$. Since the reconstructed transmission function and plane-wave transmission coefficient agree well in the high phase matching angle region, the corresponding shear velocities inverted by using the voltage function or the plane-wave transmission coefficient are virtually the same.

The above method certainly is not limited to isotropic materials, and can extended to anisotropic materials, especially composites. The first composite material we have

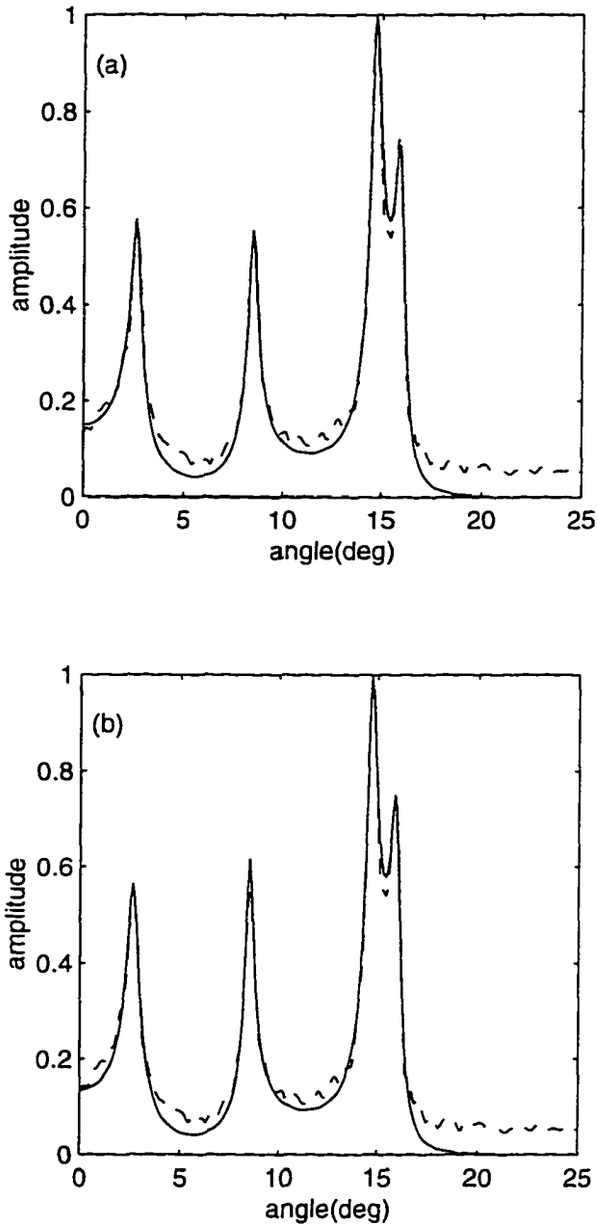

Figure 3.11 (a) Inversion of experimental data by reconstructed transmission coefficient T_r; (b) inversion of experimental data by the plane-wave transmission coefficient. Two approaches give different constants. The former gives $c_l = (2.74, -0.03\,i)$ and $c_t = (1.38, -0.018\,i)$ while the latter gives $c_l = (2.74, -0.063\,i)$ and $c_t = (1.38, -0.018\,i)$. In all figures dashed curves are experimental data and solid curves are calculated from the fitted constants.

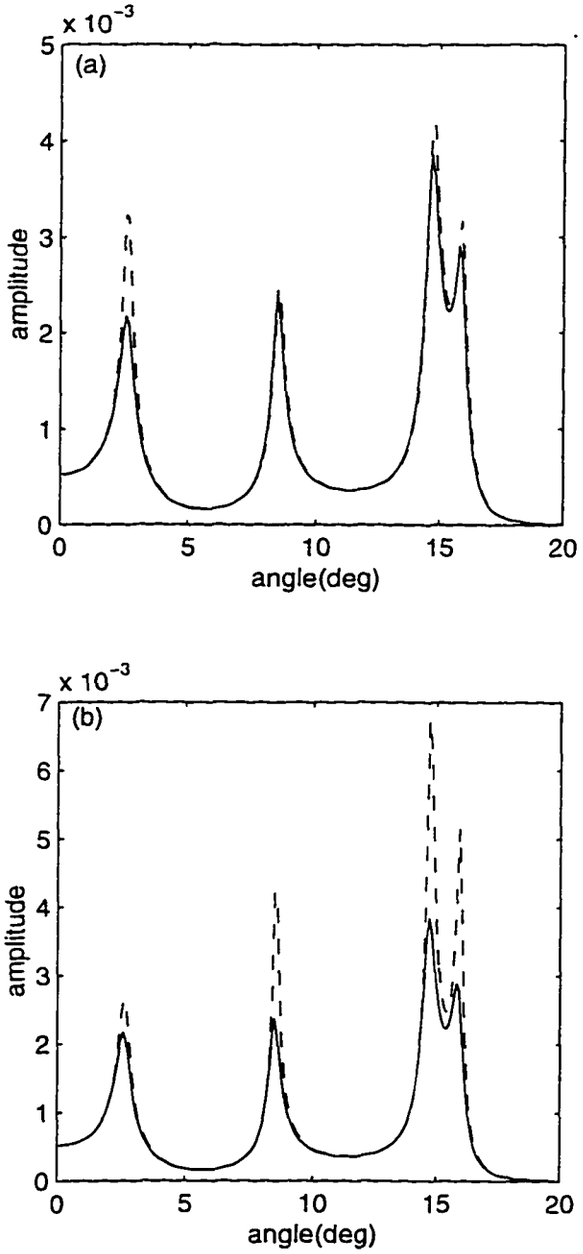

Figure 3.12 (a) The effect of 50% decrease of $\Im\{c_l\}$ (dashed curve) on the transmission coefficient, showing that the transmission coefficient amplitude at low phase matching angles determines $\Im\{c_l\}$. (b) The effect of a 50% reduction in $\Im\{c_t\}$ (dashed curve) on the transmission function, showing the amplitude at high phase matching angles determines $\Im\{c_t\}$. In both (a) and (b) the solid curves are the calculated transmission function obtained by assuming $c_l = 2.74 - 0.063\,i$ and $c_t = 1.38 - 0.018\,i$ km/sec.

tested is uniaxial graphite epoxy. We can regard uniaxial graphite epoxy as transversely isotropic, and there exist five independent stiffnesses, *ie*. C_{11}, C_{13}, C_{33}, C_{23}, C_{55}. Because of the limited frequency range, only some of these can be determined here. Shown is Fig. 3.13 is the reconstructed transmission function when the scan direction is normal to the fiber direction at 1.1 MHz. In the present scan the transmitted signal depends only on C_{33} and C_{23}. The optimization procedure yields $C_{22} = 16.25 - 0.305\,i$ and $C_{23} = 7.64 - 0.53\,i$ GPa. We find that the transmission coefficient also give almost the same results, as is shown by the dash-dot curve in Fig. 3.14. The reason for this outcome is that the imaginary parts of C_{33} and C_{23} have no dependence on the higher order modes which have a phase matching angle around 4°. In order to determine other elastic constants we must perform coordinate scans along the fiber direction. An example of data taken in a scan direction parallel to the fibers is shown in Fig. 3.14. For such a scan at a frequency of 1.1 MHz, only C_{11} and C_{55} influence the transmission coefficient (we note C_{12} and C_{22} also depend on parallel scan but that's at high frequency) . However as shown in Fig. 3.14, the high order Lamb mode around 2.5° can hardly be seen from the experiment which C_{11} strongly depends on. The reason is that the finite spacial scan limites the resolution of the peak in the wave vector space. Here, C_{11} is taken from independent measurements [27], then C_{55} can be effectively determined to be $C_{55} = 8.4 - 0.25\,i$ GPa.

We have also extended these measurements to biaxial graphite epoxy. The plates we work with here ($[0,90]_{3s}$) are of the class of so-called balanced orthotropic laminates. Since the number of plies in the two fiber directions is the equal, according to lamination theory [30] the following relations among the elastic properties obtain, $C_{11} = C_{22}$, $C_{13} = C_{23}$, and $C_{44} = C_{55}$. The assumption of lamination theory is justified by the relatively low frequencies employed in these air-coupled measurements. Thus, we have six independent stiffness constants, C_{11}, C_{12}, C_{13}, C_{33}, C_{44}, C_{66}. Earlier we found at 1.1 MHz that the transmission coefficient is sensitive to $\Re\{C_{11}\}$, $\Re\{C_{13}\}$, C_{33}, and C_{44}, and also slightly

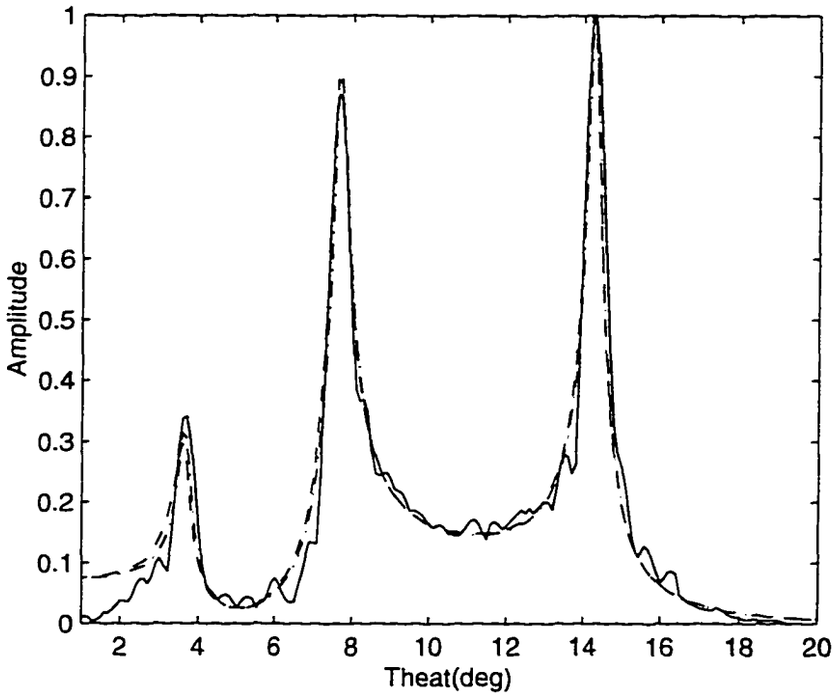

Figure 3.13 The experimental reconstructed transmission coefficient (solid curve) of a uniaxial graphite epoxy plate and a best fit with reconstructed transmission function (dashed curve) and with plane wave transmission coefficient at 1.1 MHz when the scan direction is normal to the fibers. The fitting procedure gives $C_{22} = 16.25 - 0.305\,i$ and $C_{23} = 7.64 - 0.53\,i$ GPa.

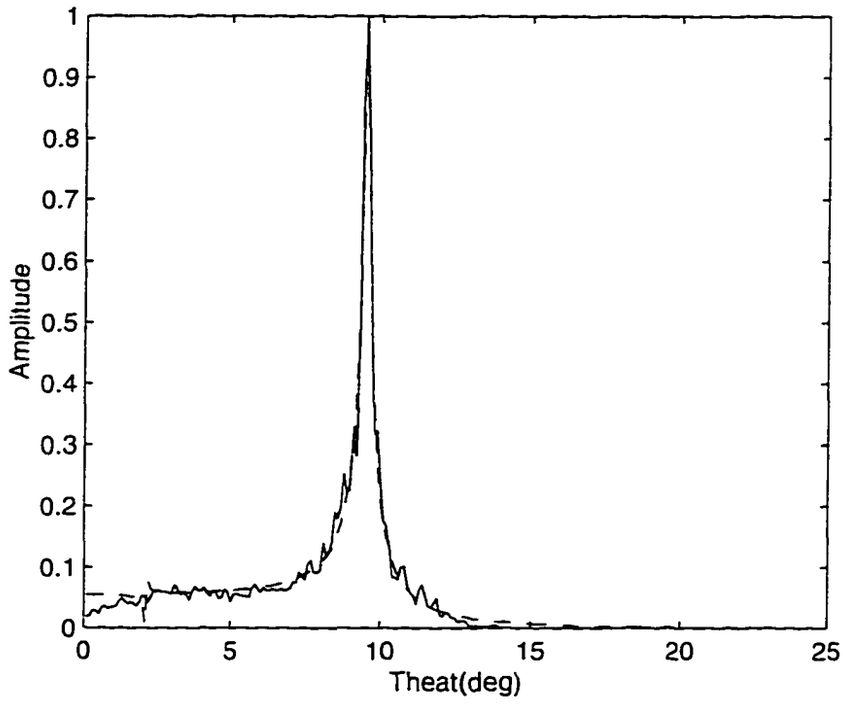

Figure 3.14 The reconstructed transmission coefficient (solid curve) of a uniaxial graphite epoxy plate and best fit results (dashed curve) at 1.1 MHz when the scan direction is parallel to the fibers. The fitting procedure gives $C_{55} = (8.4, -0.25\,i)$ GPa.

dependent on $\Im\{C_{11}\}$, $\Im\{C_{13}\}$. The transmission coefficient is almost independent of C_{12} and C_{66}. At 0.41 MHz, however, the transmission coefficient is almost completely dependent on $\Re\{C_{11}\}$ and C_{44}. So our approach is first to determine C_{11} and C_{44} by using the data at 0.41 MHz, and then to determine C_{13} and C_{33} by using data of 1.1 MHz. An experimental transmission function measured at 0.41 MHz is shown in Fig. 3.15 as a solid curve, where only the A_0 mode can be seen. A theoretical analysis indicates that the Lamb mode near 3° is determined by C_{11}. Fortunately this unseen mode in air-coupled experiments is quite obvious in fluid immersion testing [27] because of two factors, first we can perform a longer range of scan, second the higher velocity of water compared with air will widen the peak. This peak in immersion testing can be used to determine C_{11}, which we have found is 71.3 GPa. Knowing C_{11}, an inversion that determines two constants $\Re\{C_{44}\}$ and $\Im\{C_{44}\}$ can be easily performed and the result is $C_{44} = 5.24 - 0.43\,i$. The corresponding fitted curve is shown as a dashed trace in Fig. 3.15. With the knowledge of C_{11} and C_{44}, we can proceed to invert C_{13} and C_{33} from the experimental data of 1.1 MHz. The results are shown in Fig. 3.16, where the best fit gives $C_{13} = 3.45 - 0.085\,i$ and $C_{33} = 15.83 - 0.49\,i$.

As a last example of a complicated composite material, we have investigated the elastic behavior of a quasi-isotropic graphite-epoxy laminate, having the following layup sequence $[0, \pm 45, 90]_{2S}$. Now, not only are x_1 and x_2 directions the same elastically, but also C_{11}, C_{12}, and C_{66} satisfy the relation $C_{66} = (C_{11} - C_{12})/2$. The experiment is performed at 1.1 MHz, and the data are shown in Fig. 3.17 as a solid curve. A careful sensitivity analysis of this plate shows that at 1.1 MHz, the transmission coefficient is sensitive to $\Re\{C_{11}\}$, C_{13}, C_{33}, and C_{44}. C_{11} must still be determined by the immersion method cited earlier [27]. With these assumptions an inversion of experimental data to determine the six parameters is performed, where the fitted curves are shown in Fig. 3.17 as dashed. The fitted parameters are $C_{13} = -5.48 + 0.22\,i$, $C_{33} = 12.68 - 0.40\,i$ and $C_{44} = 5.54 - 0.14\,i$. Agreement with the experimental results is reasonably good, with

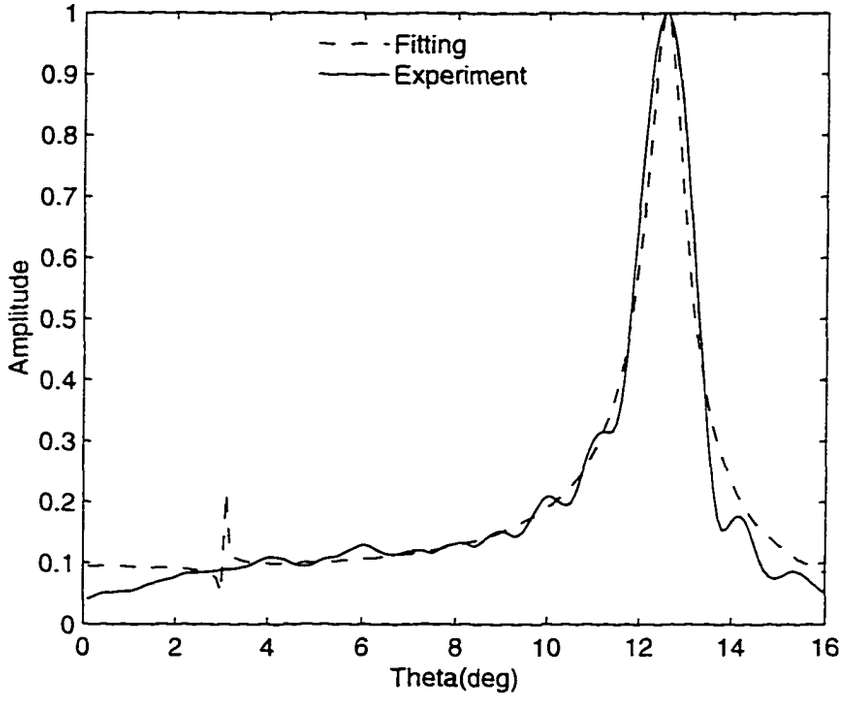

Figure 3.15 The reconstructed transmission coefficient (solid curve) of a biaxial graphite epoxy laminate and best fit results (dashed curve) at 0.41 MHz. The fitting procedure gives $C_{44} = (5.24, -0.43\,i)$.

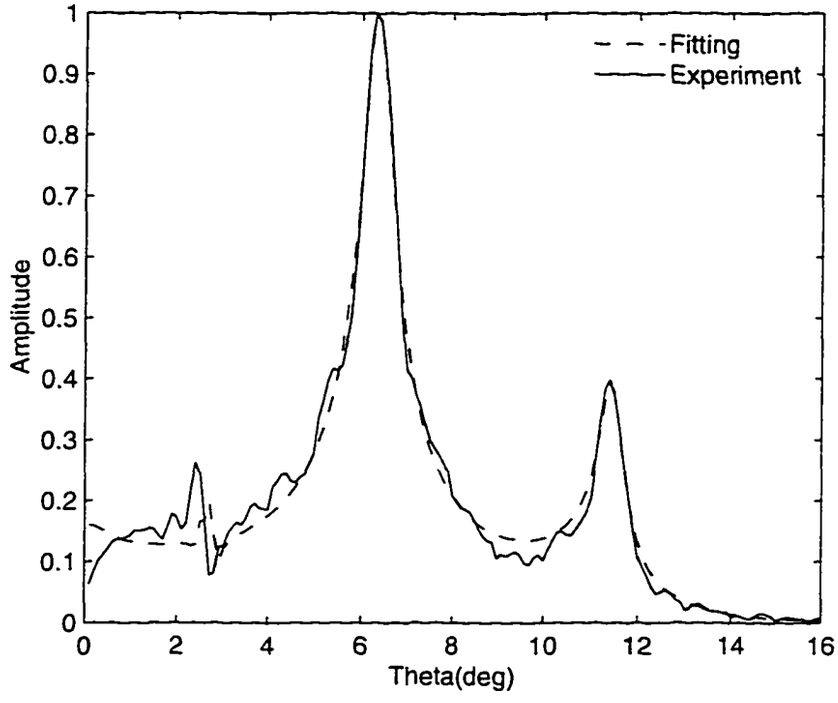

Figure 3.16 The reconstructed transmission coefficient (solid curve) of a biaxial AS/4 epoxy laminate and best fit results (dashed curve) at 1.1 MHz. The fitting procedure gives $C_{13} = (3.45, -0.085\,i)$ and $C_{33} = (15.83, -0.49\,i)$.

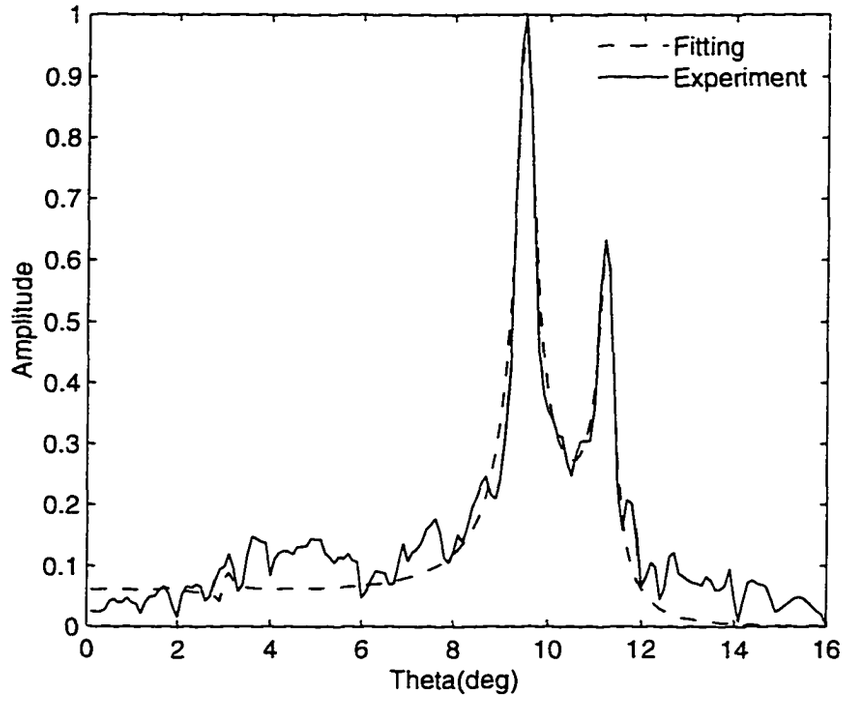

Figure 3.17 The reconstructed transmission coefficient (solid curve) of a quasi-isotropic graphite epoxy laminate and best-fit results (dashed curve) at 1.1 MHz. The fitting procedure gives $C_{13} = (5.48, 0.22\,i)$. $C_{33} = (12.68, 0.40\,i)$ and $C_{44} = (5.54, 0.14\,i)$.

the exception of some noise near the detection threshold. which may be structural rather than electronic in nature.

Conclusion

In this chapter, we have reformulated the problem of voltage calculations in two- and three-dimensional beam geometries in terms of the mathematically efficient complex transducer point. Moreover. we have studied the reconstruction of the transmission function by a wavenumber analysis method. consisting of summing the derived wavenumber spectra from different incident angles. We have analyzed. in particular. the influence

on the reconstructed transmission function of rays lying outside the incident plane .

The difference between the reconstructed transmission functions obtained by using the transducer voltage calculated from a Gaussian sheet beam and a rotationally symmetric 3-D Gaussian beam are not large, but may, under some conditions, be significant. The difference is especially large near normal incidence. The sheet beam reconstructs identically to the plane-wave transmission coefficient, while the 3-D beam gives a result that differs solely in the relative amplitudes of the transmission peaks and valleys.

We have also discussed from a quantitative perspective the influence of this transmission function difference on the inferred material parameters. As well, we have considered the effects of a finite coordinate scan on the data processing. Finally, we have performed experiments both on isotropic and anisotropic materials and have applied inversion algorithms based on well known schemes to deduce elastic material parameters of our samples.

Acknowledgment

The authors would like to thank Smaine Zeroug for helpful discussions. This work was performed with partial support from Air Force Office of Scientific Research through the UTEP-FAST Center at the University of Texas at El Paso.

References

[1] D. E. Chimenti, "Guided waves in plates and their use in materials characterization," Appl. Mech. Rev, **50**, 247–284 (1997).

[2] M. R. Karim and A. K. Mal, "Inversion of leaky Lamb wave by simplex algorithm", J. Acoust. Soc. Am. **88**, 482–491 (1990).

[3] S. I. Rokhlin and D. E. Chimenti. "Reconstruction of elastic constants from ultrasonic reflectivity data in a fluid coupled composite plate". *Review of Progress in Quantitative NDE.* Vol. 9. Eds. D. O. Thompson and D. E. Chimenti. (Plenum. New York. 1990). 1411-1418.

[4] S.I.Rokhlin. C.Y.Wu and L.Wang. "Application of coupled ultrasonic plate modes for elastic constant reconstruction of anisotropic composite". *ibid.* Vol. 9. 1403-1411 (1990).

[5] Y. Bar-Cohen and A.K.Mal. "Characterization of composiote laminate using combined LLW and PBS methods". *ibid.* Vol. 10. 1555-1560 (1991).

[6] K. Suzukim. K. Huguchi and H. Tanigawa."A silicon electrostatic ultrasonic transducer." IEEE Trans. Ultrason. Ferroelect. Freq. Contr. **36**. 620-627 (1989).

[7] D. W. Schindel. D. A. Hutchins. L. Zhou and M. Sayer. "The design and characteriazation of micoromachined air-coupled capaciatance transducers". IEEE Trans. Ultrason. Ferroelect. Freq. Contr. **42**. 42-50 (1995).

[8] D. W. Schindel and D. A. Hutchins. "The capacitance transducer as a standard ultrssonic source in solids." J. Acoust. Soc. Am. **97**. 1650-1659 (1995).

[9] A. Safaeinili. D. E. Chimenti. and O. Lobkis." Air-couple ultrasonic estimation of viscoelastic stiffnesses in Plates." IEEE Trans. Ultrason. Ferroelect. Freq. Contr. **43**. 1171-1180 (1996).

[10] B. Hosten. D. A. Hutchins and D. W. Schidel. "Measurement of elastic constants in composite material using air-coupled ultrasonic bulk waves." J. Acoust. Soc. Am. **99**. 2116-2123 (1996).

[11] O. I. Lobkis. A. Safaeinili. D. E. Chimenti. "Precision ultrasonic reflection studies in fluid-coupled plates". J. Acoust. Soc. Am. **99**. 2727-2736 (1996).

[12] B. A. Auld. "General electromechanical reciprocity relations applied to the calculation of elastic wave scattering coefficients." Wave Motion **1** 3-10 (1979).

[13] G. S. Kino. "The application of reciprocal theorey to scattering of acoustic waves by flews." J. Appl. Phys. **49**. 3190-99 (1978).

[14] G. A. Deschamps. "Gaussian beam as a bundle of complex rays." Electron. Lett. **7** 684-85 (1971).

[15] D. E. Chimenti. J. Zhang. S. Zeroug and L. B. Felsen. "Interaction of acoustic beams with fluid-loaded elastic structures". J. Acoust. Soc. Am. **95**. 45-59 (1994).

[16] T. J. Cloutier. A. Safaeinili. D. E. Chimenti. S. Zeroug. and L. B. Felsen. "An Experimental Study of Ultrasonic Beam Reflection From Fluids Loaded Cylindrical Shells." *Review of Progress in Quantitative NDE*. vol. 14. eds. D. O. Thompson and D. E. Chimenti. (Plenum. New York. 1995). pp. 131-138.

[17] S. Zeroug. L. B. Felsen. "Nonspecular reflection of two- and three-dimensional acoustic beams from fluid-immersed plane-layered elastic structures". J. Acoust. Soc. Am. **95**. 3075-3098 (1994).

[18] S. Zeroug and L. B. Felsen. "Nonspecular reflection of two- and three-dimensional acoustic beams from fluid-immersed cylindrically layered elastic structures". J. Acoust. Soc. Am. **98**. 584-598 (1995).

[19] S. Zeroug. F. E. Stanke. and R. Burridge. "A complex-transducer-point model for emitting and receiving ultrasonic tranducers." Wave Motion **24** 21-40 (1996).

[20] D. E. Chimenti and A. H. Nayfeh. "Ultrasonic reflection and guided waves in fluid-coupled composite laminates." J. Nondestruct. Eval. **9**. 51-69 (1990).

[21] W. Sachse and Y.-H. Pao. "On the determination of phase and group velocities of dispersive waves in solids." J. Appl. Phys. **49**. 4320-4327 (1978).

[22] D. Alleyne and P. Cawley. "A two-dimensional Fourier transform method for the measurement of propagating multimode signals." J. Acoust. Soc. Am. **89**, 1159-1168 (1991).

[23] L.M.Brekhovskikh. *Waves in Layered Media*(Academic. New York. 1960). Chapt 4.

[24] L. B. Felsen and N. Marcuvitz. *Radiation and Scattering of Waves* (Prentice Hall. Englewood Cliffs. 1973).

[25] Han Zhang. D. E. Chimenti. S. Zeroug. "Transducer misalignment effects on voltage amplitude in beam reflection from elastic structures." J. Acoust. Soc. Am.. under review.

[26] M. Abramovits and I. A. Stegun. *Handbook of Mathematical Function*. Dover. New York. Page 298. 1965.

[27] O. L. Lobkis and D. E. Chimenti. "In plane stiffness determination of composite materials." to appear in *Review of Progress in Quantitative NDE*. vol. 17. eds. D. O. Thompson and D. E. Chimenti. (Plenum. New York. 1998)

[28] O. L. Lobkis and D. E. Chimenti. "Anisotropic materials characterization using air-coupled ultrasound." *Review of Progress in Quantitative NDE*. vol. 16. eds. D. O. Thompson and D. E. Chimenti. (Plenum. New York. 1997). pp. 1375-1382.

[29] W. H. Press. S. A. Teukolsky. W. T. Vetterling and B. P. Flannery. *Numerical Recipes in FORTRAN*. Cambridge. Chapter 10. 1995.

[30] T. H. Hahn. W. Stephen. *Introduction to composite materials*. Lancaster. PA (1980).

CHAPTER 4 COMPLEX TRANSDUCER POINT ANALYSIS OF THE LAMB WAVE SPECTRUM: COMPARISON OF 2-D AND 3-D APPROACHES

A paper to be submitted to the Journal of Acoustical Society of America

Han Zhang and D. E. Chimenti

Abstract

In this chapter is presented a frequency analysis of the Lamb wave reflection spectrum based on the complex transducer point. By assuming a linear dependence of the Fresnel length on the frequency for flat piston transducer, the complex transducer point has been employed to model the wavenumber response of the transducers. With the aid of the reciprocal theorem, a rigorous 3-D receiver voltage spectrum in a pitch-catch setup has been derived by using two complex transducer points. The calculations are supported by the results of numerous experiments on both isotropic and anisotropic materials in various measurement geometries. The model calculation is also applied to illuminate several materials characterization issues.

Introduction

The complex source point (CSP) has been widely used to study Gaussian beams since its introduction by Deschamps [1]. As we saw in the previous chapter, real pis-

ton transducers. when used in pairs. can be well approximated by combined Gaussian beams. Therefore. the CSP has found wide used in acoustics. especially in the theoretical study [2]–[5] of nonspecular reflection. These calculations have then been successfully compared to experiments [6]–[7].

In all these studies the reflected field or receiver voltage as a function of coordinate scan distance. at an incident angle close to the Rayleigh or Lamb wave phase matching angle. is calculated or measured at a single frequency.

In that case. a 2-D calculated reflected field or receiver voltage in the incident plane is almost the same as a 3-D calculation. except for a scale factor (as we will show in this paper).

In retrospect. the rigorous calculation of nonspecular reflection undertaken first by Bertoni and Tamir [11] and most subsequent work has treated the transducer fields using a 2-D beam representation [12]–[13]. In these formulations the incident beam is taken to have no dependence in a direction normal to the incident plane. say the x_1x_3 plane. Equivalently. we may consider such a beam as a sheet beam. in which all dependence on the x_2 field variable vanishes. Only more recently have calculations appeared using a full 3-D formulation [2]–[5]. In other. quite recent. studies [14. 15] the computations are further extended to include the effect of the finite aperture of the receiver. In none of these works. is a careful comparison between the 2-D and 3-D analyses ever done.

A major objective of this present work is to perform such a detailed comparison. The results we have obtained show that the 2-D calculation is sufficient for the study of the spatial distribution of the receiver voltage. *e.g* when the receiver voltage is measured as a function of scan distance. This comparison also confirms the validity of our previous 2-D voltage calculation [16]–[17]. The plate reflection or transmission coefficient calculated as a function of frequency. however. is widely used to model the receiver voltage and to infer indirectly the plate materia, parameters [8]–[10]. Such an experiment can be performed easily and efficiently. It is necessary to verify the validity of the theoretical

model so that its use in the signal analysis and extraction of material properties is fully justified.

In this chapter we extend the complex transducer point (CTP) to this widely used ultrasonic Lamb wave technology. We show that, unlike the results of the previous chapter, in which the 2-D and 3-D calculation give nearly identical results, the reflection frequency spectrum requires a full 3-D voltage calculation to achieve the desired accuracy under all conditions. A 2-D voltage calculation will not yield accurate results, neither for the reflected voltage amplitude, nor for the position of reflection voltage minima. The 3-D receiver voltage frequency spectrum calculated here is compared to extensive experimental results on several materials and in different experimental configurations. The results show that the 3-D voltage spectrum calculation must be used under some conditions to deduce precise material parameters.

Theory

The derivation of receiver voltage as a function of frequency is similar to the development of the previous chapter where the coordinate is scanned, except that the Fresnel length b is not fixed, but is instead a function of frequency. We first construct the complex receiver and complex transmitter by displacing the real point source (x', y', z') and real point receiver (x, y, z) into the complex plane according to the geometry shown in Fig. 4.1.

$$\tilde{x} = x - ib\sin\alpha, \qquad \tilde{y} = y, \qquad \tilde{z} = z + ib\cos\alpha, \tag{4.1}$$

$$\tilde{x}' = x' + ib\sin\alpha, \qquad \tilde{y}' = y', \qquad \tilde{z}' = z' + ib\cos\alpha, \tag{4.2}$$

where α is the transmitter and receiver angle, and b is the Fresnel length, given by $b = k_f w_0^2/2$, with the fluid wavenumber $k_f = \omega/c_f$, c_f is fluid velocity, and w_0 is the beam width at its waist. An effective approximation of w_0 is $w_0 = 0.7512 r_0$ [18] with r_0

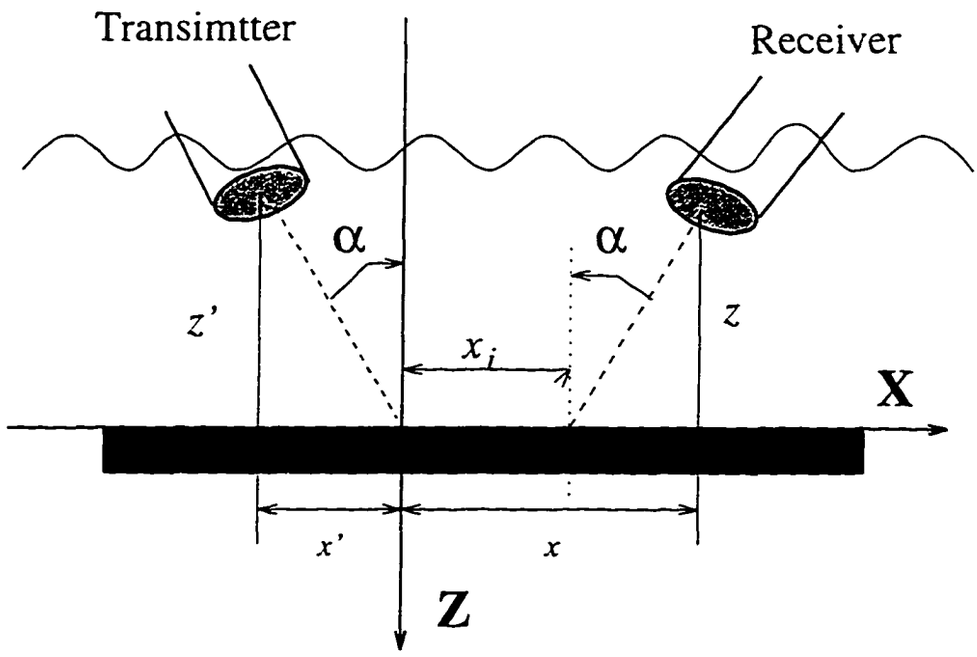

Figure 4.1 Geometric configuration used in the experiment and calculation.

the radius of the piston transducer. The receiver voltage can then be synthesized from the spectral decomposition of the complex Green's function weighted by the plane-wave reflection coefficient [15].

$$V_{\mathcal{R}}(a,x,f) = \frac{-1}{8\pi^2}\gamma(\omega)\omega\rho_f A_T A_{\mathcal{R}} \int_{-\infty}^{\infty}\int_{-\infty}^{\infty} R(k_x,k_y) \times \frac{\exp\{ik_x(\tilde{x}-\tilde{x}')+ik_y(\tilde{y}-\tilde{y}')-i\kappa_f(\tilde{z}+\tilde{z}')\}}{\kappa_f}\,dk_x\,dk_y\,. \quad (4.3)$$

where $\kappa_f = \sqrt{k_f^2 - k_x^2 - k_y^2}$ is the wavevector projection onto the z axis. As mentioned earlier, the calculated frequency spectrum is different for a 3-D beam and a 2-D beam. We separate our theoretical exposition into two parts: one for the 2-D beam, and the other for the 3-D beam.

2-D Calculation

For the 2-D case, the voltage has no dependence on y, so we let $k = k_x$ and $\kappa_f = \sqrt{k_f^2 - k^2}$. The voltage calculation Eq. (4.3) becomes

$$V_R(\alpha, x, f) = \frac{-1}{8\pi^2}\gamma(\omega)\omega\rho_f A_T A_R \int_{-\infty}^{\infty} R(k)\, \frac{\exp\{ik(\tilde{x} - \tilde{x}') + i\kappa_f(\tilde{z} - \tilde{z}')\}}{\kappa_f}\, dk. \quad (4.4)$$

The above integral can be evaluated directly by numerical integration or can be estimated asymptotically. The asymptotic formula is well detailed in [4] and can also be found in Appendix B.

3-D Calculation

For the 3-D voltage calculation, as in Eq. (4.3) above and similarly to the development in Chapter 3, we also use spherical coordinates because of convenience and because the calculation leads to explicit physical meaning. In a spherical coordinate system,

$$k_x = k_f \sin\theta\, \cos o. \qquad k_y = k_f \sin\theta\, \sin o. \qquad k_z = \kappa_f = k_f \cos\theta. \quad (4.5)$$

and

$$\frac{dk_x\, dk_y}{\kappa_f} = k_f \sin\theta\, d\theta\, do. \quad (4.6)$$

Also, we limit our study to sources located in the incident plane, so $\tilde{y} = \tilde{y}' = 0$, then Eq. (4.3) becomes

$$\begin{aligned} V_R(\alpha, x) \;=\; & \frac{-1}{8\pi^2}\gamma(\omega)\omega\rho_f A_T A_R \int_0^{2\pi} \int_0^{\pi/2 - i\infty} R(\theta, o) \\ & \times \exp\{ik_f(\sin\theta\, \cos o(\tilde{x} - \tilde{x}') - \cos\theta(\tilde{z} + \tilde{z}'))\}\; k_f \sin\theta\, d\theta\, do. \quad (4.7) \end{aligned}$$

We assume the reflection coefficient is independent of o, so the integral over o can be evaluated at saddle point. Two saddle points exist for o. One is $o_s = 0$, representing a forward propagating wave, and the other is $o_s = \pi$, representing a backward propagating

wave. We, therefore, take $o_s = 0$, and the above integral reduces to

$$V_R(\alpha, x) = \frac{\gamma(\omega)\omega\rho_f A_T A_R \exp(-i\pi/4)\sqrt{k_f}}{8\pi^2\sqrt{\tilde{x}-\tilde{x}'}} \int_0^{\pi/2-i\infty} R(\theta) \times \exp\{ik_f(\sin\theta(\tilde{x}-\tilde{x}') - \cos\theta(\tilde{z}+\tilde{z}'))\}\sqrt{\sin\theta}\, d\theta . \quad (4.8)$$

The above integral can again be evaluated asymptotically by changing the integration contour to a steepest descent path, where particular attention must be given to the pole that is crossed during the path change. The contribution of this pole must be properly accounted for when the pole is close to the saddle point. This problem has been solved by Felson and Marcuvitz [19] and has been widely used to solve both acoustic and electromagnetic wave problems [4, 5, 14]. The same approach can be applied here. First, the saddle point can be obtained by setting the first derivative of phase with respect to θ to zero.

$$\theta_s = \arctan\frac{\tilde{x}-\tilde{x}'}{\tilde{z}+\tilde{z}'} . \quad (4.9)$$

Then we calculate the contribution of the saddle point and pole, whose sum forms the total receiver voltage.

$$V_R(\alpha, x) = \frac{\gamma(\omega)\omega\rho_f A_T A_R \exp(-i\pi/4)\sqrt{k_f}}{8\pi^2\sqrt{\tilde{x}-\tilde{x}'}} \exp(ip(\theta_s)) \times \left\{ \{R(\theta_s)\sqrt{\frac{-2\pi\sin\theta_s}{ik_f\tilde{L}}} + \sum_{j=1}^{M} 2\pi i\sqrt{\sin\theta_{p_j}} \times \mathrm{Res}\{R(\theta_{p_j})\}[\frac{1}{2\sqrt{\pi}i\tilde{S}_{p_j}} + \frac{1}{2}\exp(-\tilde{S}_{p_j}^2)\mathrm{erfc}(-i\tilde{S}_{p_j})] \right\} . \quad (4.10)$$

where $\tilde{L} = \sqrt{(\tilde{x}-\tilde{x}')^2 + (\tilde{z}+\tilde{z}')^2}$ is the complex distance from an image source to the receiver, and $p^r(\theta_s)$ is the phase

$$p(\theta) = k_f(\sin\theta(\tilde{x}-\tilde{x}') - \cos\theta(\tilde{z}+\tilde{z}')) . \quad (4.11)$$

The phase is evaluated at the saddle point $\theta = \theta_s$, and $\tilde{S}_{p_j}$ is the so-called "numerical distance" between the saddle point θ_s and jth pole of the reflection coefficient θ_{p_j}. Then,

Table 4.1 Geometry and acoustic properties of composite plate

Material	C_{11} GPa	C_{12} Gpa	C_{22} Gpa	C_{23} Gpa	C_{55} Gpa	d mm	ρ g/cm^3
Unidirectional	143.0	3.7	16.5	7.6	8.3	0.92	1.60
Biaxial	133.0	3.7	15.5	7.6	6.3	1.52	1.62

the numerical distance is

$$\tilde{S}_{p_j} = \sqrt{ip(\theta_s) - ip(\theta_{p_j})}\,. \tag{4.12}$$

where erfc is the complex complementary error function. and its definition can be found in Appendix B.

Experimental Technique

In this section we describe the materials and apparatus used in the experiments. describe the experimental procedures. and discuss data acquisition and processing. We have performed experiments on both isotropic and anisotropic materials. For the isotropic samples we have used a 3-mm thick stainless steel plate. with a longitudinal wavespeed $c_l = 5.64km/s$. shear velocity $c_t = 3.07$ km/s and density $\rho = 7.9$ kg/m^{-3}. Three anisotropic plates have been used in our experiments: these are a uniaxial graphite epoxy plate. a $[0.90]_{3s}$ biaxial graphite epoxy plate. and a quasi-isotropic laminate. These are some of the same samples used in Chapter 3 for the air-coupled ultrasound experiments. Their material properties will not be repeated here. Instead. we list the elastic constants in Table 4.1 obtained by fitting the data of extensive experiments performed in this paper.

Two identical piezoelectric transducers with a center frequency of 5 MHz and an effective diameter of 4.95 mm are employed to perform all measurement reported here. The two transducers are fastened to a rotation stage which establishes the incident

angle with a resolution of 0.01° in a pitch catch setup. The positioning of the transducer normal to the plate surface is identified ultrasonically by carefully observing the largest reflection.

The transducer is excited with the radio-frequency (rf) tone bursts of 30–50 μs duration, produced by a HP 3314A function generator and a HP 8116A modulator (see Fig. 4.2) repeated at 1 KHz. The tone burst frequency is stepped through the frequency range of 0.5–12 MHz. After interaction with the elastic plate, the reflected acoustic beam is detected by a receiver. The received signal is amplified from 20 to 40 dB in a low-noise, wideband amplifier and is video detected to reveal the rf envelope of the tone burst. The amplitude of the video signal is synchronously measured using a gated, integrating amplifier, further improving the signal/noise ratio. The resulting dc amplitude is then sampled by a 13-bit A–D converter in a HP 3458A digital voltmeter and sent over a IEEE-488 bus line to a DEC workstation for further offline processing. To acquire the reflected frequency spectrum, a frequency sweep of the tone burst is performed under computer control with a step size of 0.2 KHz. At each step, it halts long enough to allow the boxcar integrator to settle before sampling its output.

We have also developed a pulse compression technique to speed up the data acquisition and processing by using a chirp signal. An arbitrary function generator DS345 manufactured by Stanford Research Systems is used to generate the chirp signal. The DS345 function generator allows the downloading of arbitrary waveforms in discrete format and has a maximum digitization rate of 40 MHz. It is, therefore, capable of reproducing the frequency in the range 0.5-12.5 MHz. The 100 μs chirp signal is sampled by a Lecroy digitizing oscilloscope and sent to the DEC workstation after reflection from the plate and detection by the receiver. We then perform a FFT on the digitized chirp signal and plot the frequency spectrum.

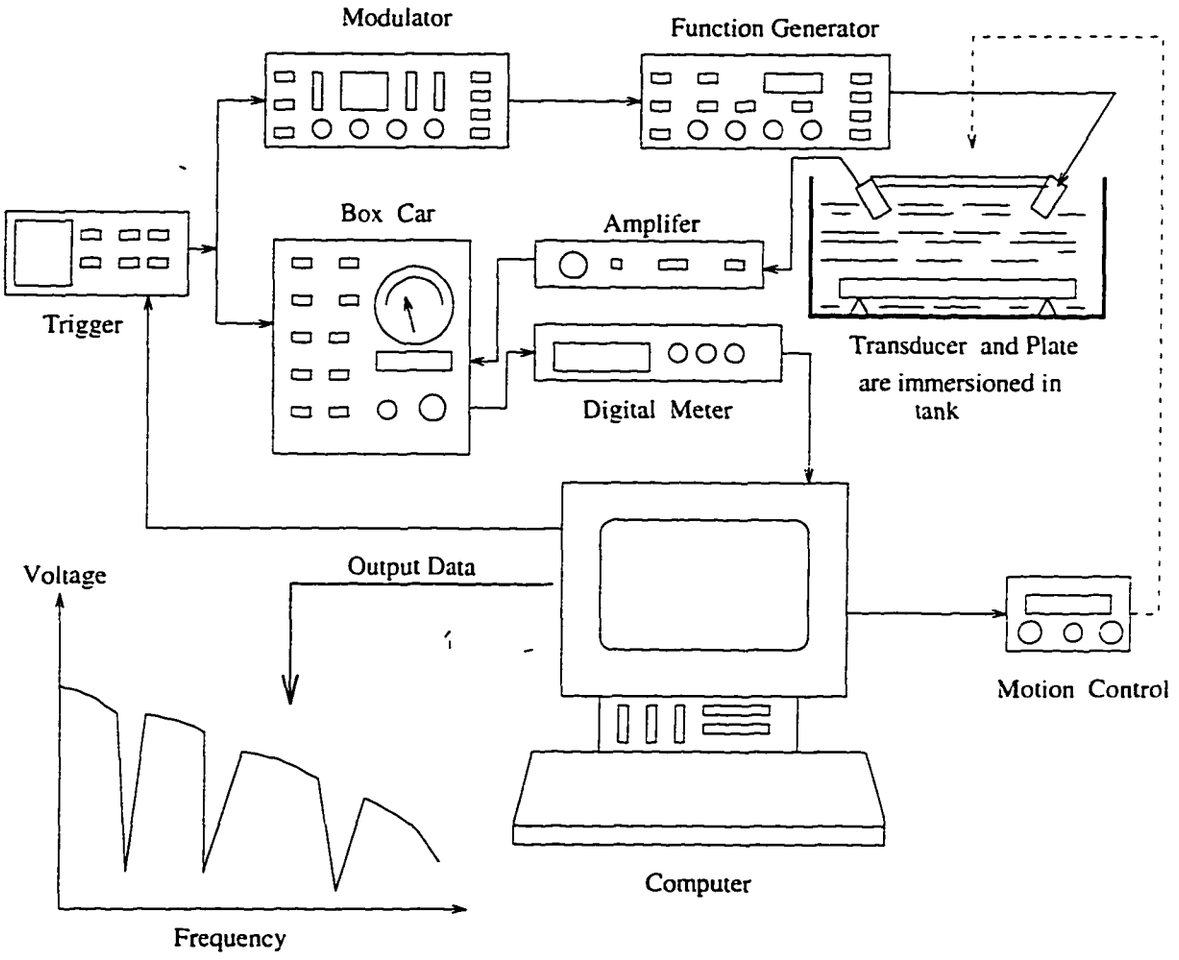

Figure 4.2 Schematic showing a block diagram with all components of experiment.

Results and Discussion

Our theoretical calculation of acoustic beam interaction with elastic structures is built on how accurately the complex transducer point can model real transducers. Since we are going to study the reflection frequency spectrum, we must verify that the CTP can model the corresponding beam variation as the frequency varies. We first discuss some transducer characteristics and then present the experimental results and theoretical calculations on beam interaction with elastic plates.

Transducer Characteristics

It is already known that for a piston transducer the beam will narrow as the frequency increases. This diffraction effect is modeled by the CTP, as seen in Fig. 4.3, showing receiver coordinate scans at several frequencies. The experiment is performed on a thick aluminum block at an incident angle of 20°, and the transducer is excited with a tone burst of 2 MHz, 5 MHz and 8 MHz. After a Fourier transform is performed on the received rf signal, 1.9 MHz, 4.9 MHz and 7.9 MHz components are extracted and plotted as a function of scan distance in Fig. 4.3. The experimental results show that a pair of CTPs can account well for the spatial characteristics of the transducers as the frequency varies. This additional result complements the points made earlier concerning the close comparison between the combined piston directivity function and that for combined Gaussian beams, as generated by the CTP formalism. No sidelobes are observed, as expected for Gaussian beams. The beam diffraction effects of the transducers, that is, their divergence properties well reproduced by the CTP.

Beam Interaction with Plates

Our confidence in using the complex transducer point to model the reflected frequency spectrum is based on the excellent agreement seen above in the transducer

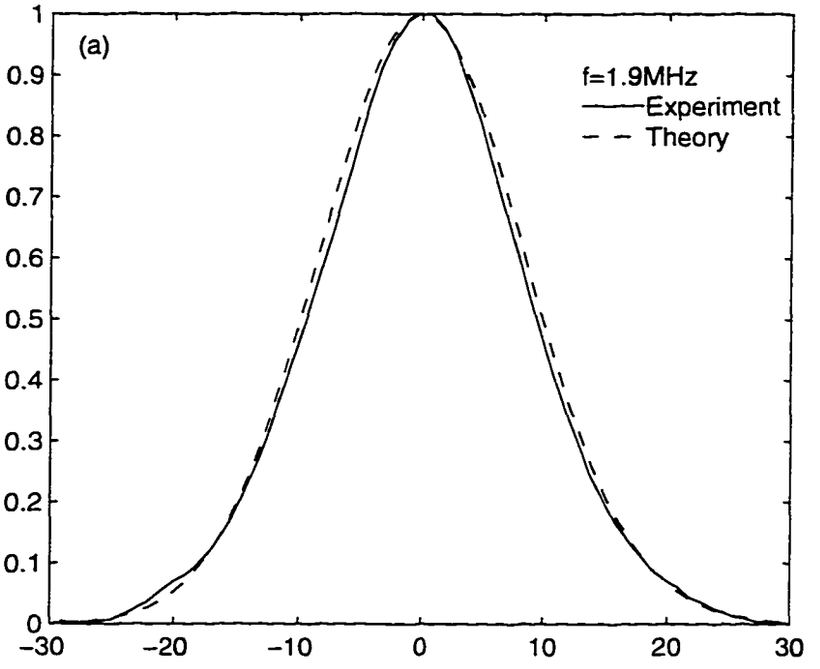

Figure 4.3 Spatial characterization of piston transducers with frequency from (a) 1.9 MHz, (b) 4.9 MHz to (c) 7.9 MHz. All experimental data are fitted by one pair of CTPs with a beam width of $w_0 = 3.56$ mm at the beam waist.

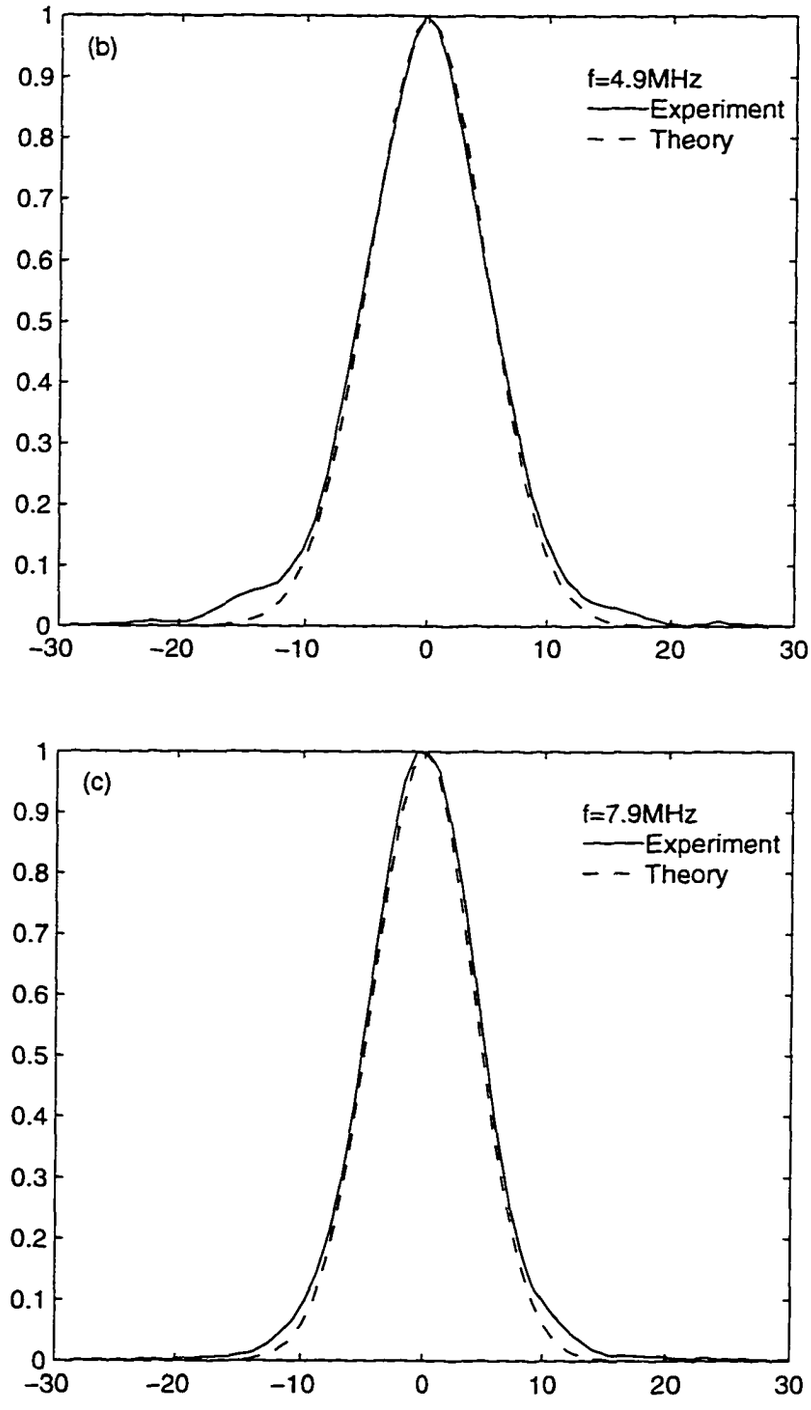

Figure 4.3 (Continued)

characteristics comparison. Now, we proceed to calculate the frequency spectrum of the reflected beam from an elastic plate. Before we present any experimental result, we show a comparison of the 2-D voltage calculation using Eq. (4.4) and 3-D voltage calculation using Eq. (4.8) in Fig. 4.4. The calculation is performed on a 1.5-mm thick steel plate at an incident angle 20°. The distance from the transducer surface to the plate is 120 mm. We see substantial differences, in the depth of the minima, although the minima location have not changed appreciably. Since the 2-D Gaussian beam can also be regarded as 3-D Gaussian sheet beam, the difference in Fig. 4.4 results from the different diffraction effects of the two beams, a complex line source and point source, with varying frequency. Similar results have been noted in Chapter 3.

This phenomena is less easily discerned in a simple x-scan, however. In Fig. 4.5 the same expressions (Eq. (4.4) and Eq. (4.8)) are used to calculate the receiver voltage as a function of scan distance at 20° and $f = 3$ MHz. After normalization by their maximum value, the two curves are almost identical. The results are very reasonable because the contribution of the rays outside of the incident plane is uniform throughout the whole scan range and therefore provides a nearly constant factor in the total receiver voltage contribution. In this case, that is a coordinate scan, the 2-D voltage calculation is sufficiently accurate.

We begin the presentation of experimental results with isotropic materials. Shown in Fig. 4.6(a) is the receiver voltage spectrum from a 3.00-mm steel plate with x offset of $x_i = 6$ mm. The overall features are well predicted by the theory, both the spectral minima positions and the general shape. The depth of the minima is also well fitted by the theory. The amplitude difference at high and low frequency results from noise introduced by the transducer response normalization. Since the 20° incident angle is greater than longitudinal critical angle of the steel, the change of longitudinal velocity has little influence on the spectrum, as we find from a separate calculation. The spectrum is very sensitive, however, to changes in the shear velocity, as shown in Fig. 4.6(b). Here,

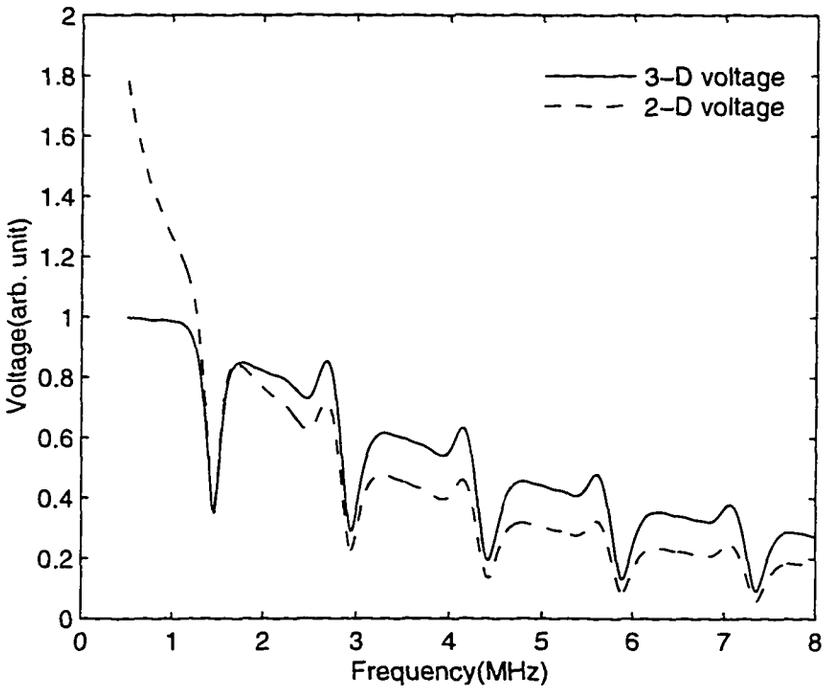

Figure 4.4 Comparison of 2-D and 3-D calculated receiver voltage frequency spectra. Calculations are performed on a 1.5-mm steel plate at 20° incident angle and x coordinate offset of $x_i = 5$ mm. The distance from the transducer surface to the plate surface is 120 mm.

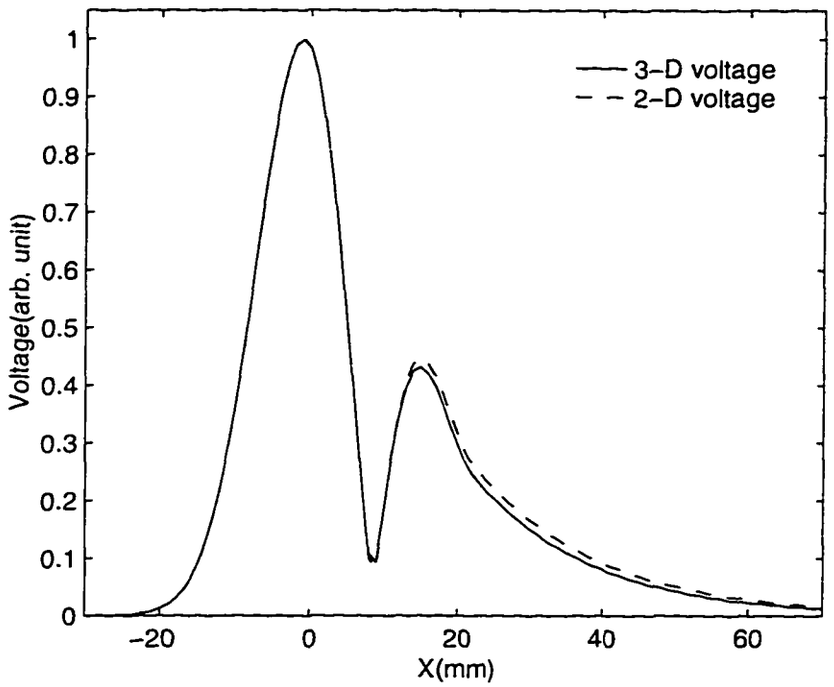

Figure 4.5 Comparison of a 2-D and 3-D x-scan voltage calculation. The calculation is performed on a 1.5-mm steel plate at 20° incident angle and $f = 3$ MHz. The distance from the transducer surface to the plate surface is 120mm.

a 2% change in the shear velocity results a totally different reflection spectrum. The phenomena observed here is clearly important for quantitative material characterization.

The characteristics in Fig. 4.6(a) can not be well explained with numerical integration. which motivates us to make an asymptotic analysis of the integral. While the numerical techniques speed the calculation. they provides little meaningful physical insight. The asymptotic expression given in Eq. (4.10) indicates that the total receiver voltage consists of a specular reflection and a leaky wave. Such an asymptotic analysis is performed here and is employed to explain the frequency spectrum characteristics shown in Fig. 4.6(a). The correctness of this analysis is confirmed by the comparison with the direct numerical integration results. as shown in Fig. 4.7(a). The two curves almost overlap. except at the sharp peak near 2 MHz and at the small variation around 11 MHz. This difference can be attributed to the singularity resulting from the vanishingly small numerical distance between the saddle and the pole. When the saddle point and the pole are very close. both the specular reflection and the leaky wave are very large. Their sum. however. remains bounded because of their different phases. In a numerical calculation some truncation error may result that causes the two parts to be not well matched. and some anomalous points may appear. The most difficult part in performing the asymptotic calculation in the present case is that there are multiple poles. and their positions vary with frequency.

We have developed an algorithm that keeps track of the poles that are within $\pm 7.5^\circ$ of the incident angles. In such a 15° range either side of the central ray we have two or three poles at low frequency and ten or eleven poles at high frequency. The poles lying outside this angular range have negligible effects on the leaky wave. Shown in Fig. 4.7(b) are the separate contributions of the leaky wave and the specular reflection of such a calculation. The sum of them is also plotted as a solid curve. The total receiver voltage level is influenced by the specular reflection. because the receiver is located within the specular reflection region. The phase difference between the specular

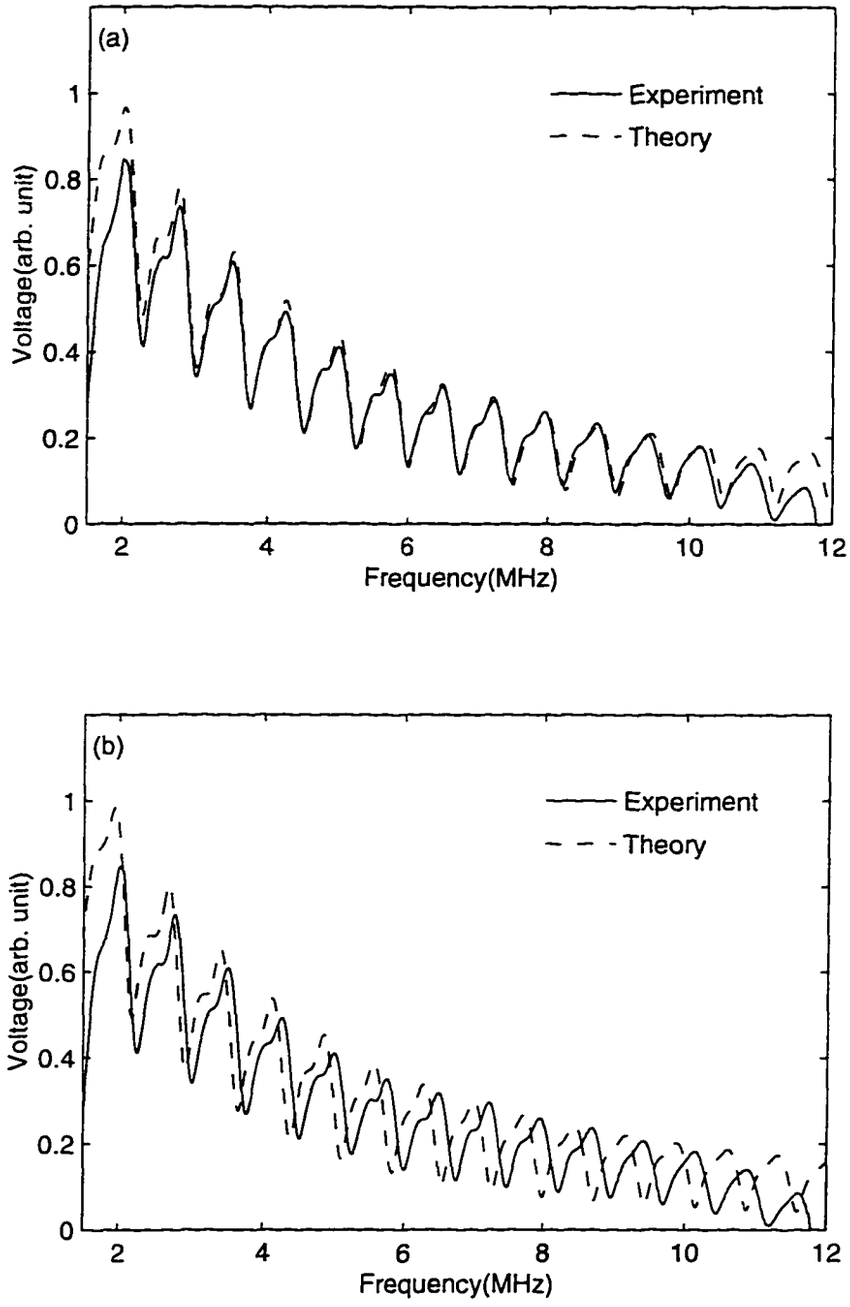

Figure 4.6 (a) Receiver voltage spectrum of a steel plate at 20° incidence, with x coordinate offset of $x_i = 6$ mm; (b) receiver voltage spectrum sensitivity to shear velocity at 20°, with 2% change of shear wavespeed resulting in a large disparity with the experimental results.

reflection and leaky wave is shown by the fact that the total receiver voltage minima occur at the maximum of the leaky wave. The reinforcement of the leaky wave minima and the specular reflection results a sharp peak on the top of every cycle of the receiver voltage. The sharp peak becomes less obvious because of the decrease in the strength of the specular reflection as frequency increases. The decrease, as we know, is due to beam diffraction effects shown in Fig. 4.3.

If the transducer is moved outside of the specular reflection region, we will observe different characteristics. Such a case is shown in Fig. 4.8(a), where the receiver voltage spectrum is recorded at an incident angle of 20° but with a coordinate offset of $x_i = 11$ mm and is compared with the theoretical prediction. The theoretical modeling and experiment result agree well in a very broad frequency range, except at very low frequencies, where poor transducer response results in some noise and the corresponding normalization variations. Again the spectrum observed in frame (a) can be well explained by the asymptotic analysis shown in frame (b). Although the receiver offset is larger than the transducer diameter in this case, the specular reflection still dominates the receiver voltage at low frequency. Because of the beam diffraction effects at low frequency, the leaky wave maximum results a minimum in the total receiver voltage. The total receiver voltage spectrum shows a periodic small peak followed by a large peak. The small peak aligns with the minimum of the leaky wave at first, and gradually degenerates. Finally, the receiver voltage spectrum minima align with the minima of the leaky wave. Above 7MHz the leaky wave is almost the sole contribution to the total receiver voltage.

The receiver voltage spectrum at 10° incidence, below the longitudinal critical angle, and at a coordinate offset of $x_i = 6$ mm is recorded in Fig. 4.9(a). As before, the receiver voltage spectrum also shows periodic cycles but also many small variations. Nonetheless, all fine features are still well modeled by the theory. All these small variations in fact come from the leaky wave, as confirmed by the separate leaky wave calculations in frame

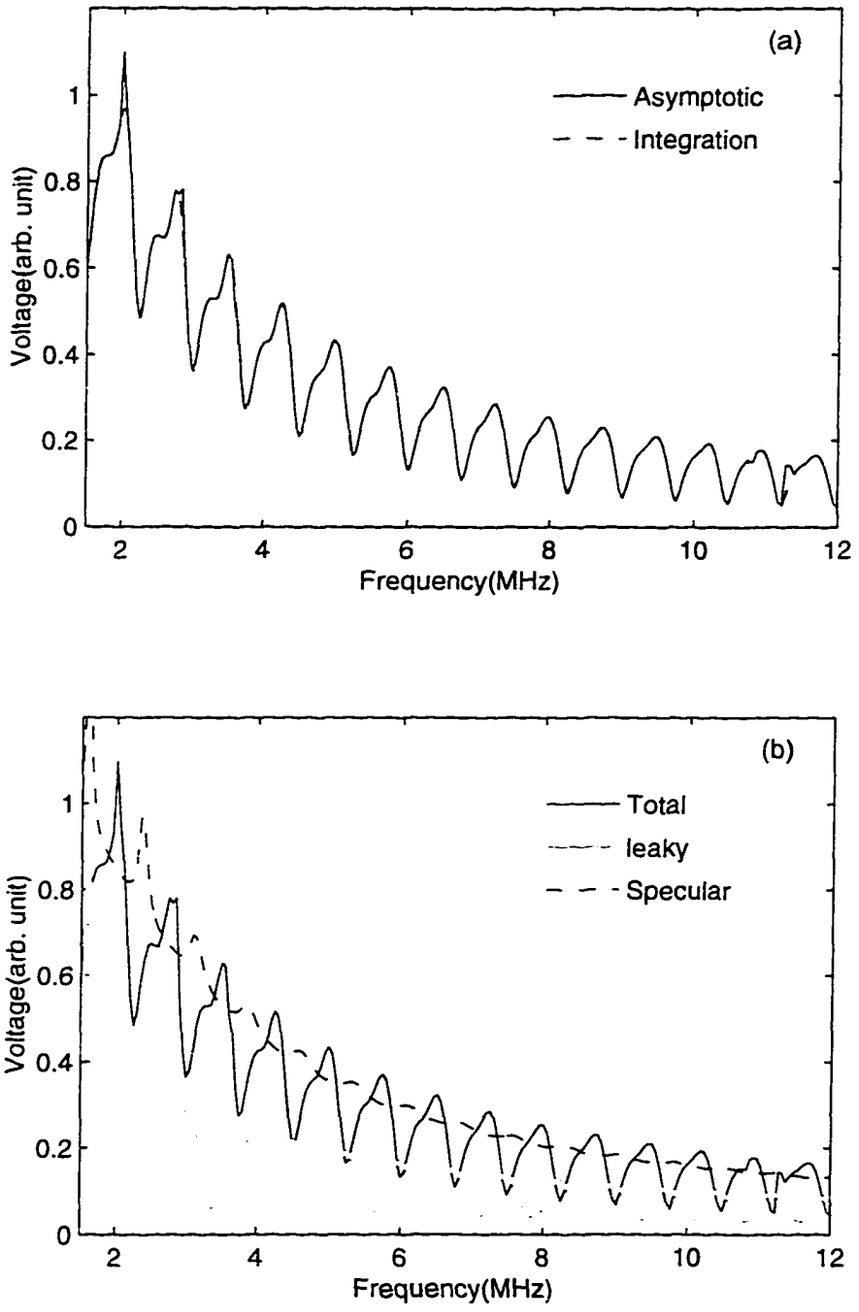

Figure 4.7 (a) Comparison of an asymptotic receiver voltage spectrum and a direct numerical integration calculation: (b) separate contributions of the leaky wave and specular reflection in the total receiver voltage spectrum.

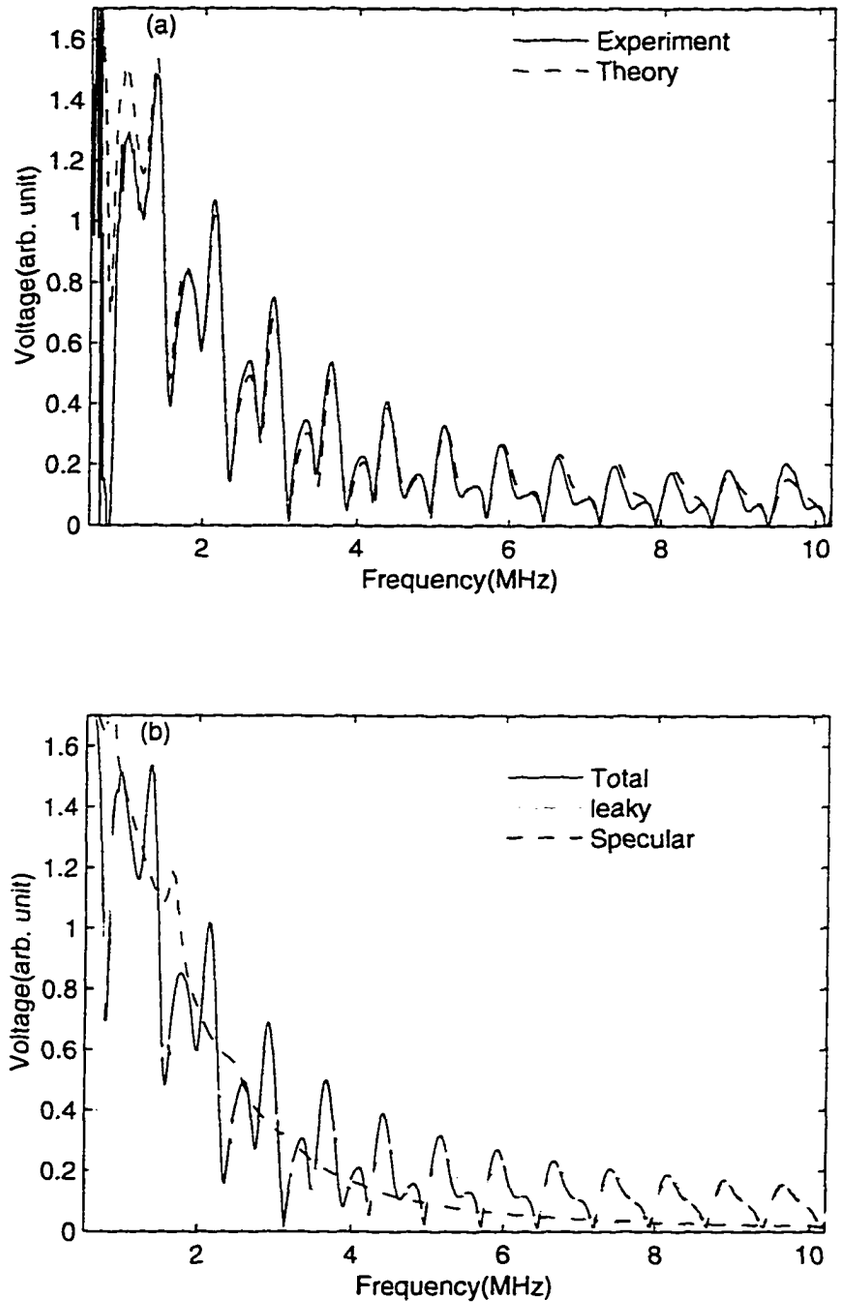

Figure 4.8 (a) Comparison of experimental receiver voltage spectrum of a steel plate at 20° incidence and coordinate offset of 6 mm with the theoretical prediction: (b) separate contributions of leaky wave and specular reflection in the total receiver voltage.

(b). Physically, at 10° the poles are closer, and they give the same order of contribution to the total receiver voltage, so their interference produces the small variations. Again, in frame (b) we observe that the sharp peak at the upper right of each cycle of the total receiver voltage spectrum results from interference of the specular reflection and leaky wave.

Since 10° is less than longitudinal critical angle, the receiver voltage spectrum is sensitive to both shear velocity and longitudinal velocity, as shown in Fig. 4.10. In frames (a) and (b) the calculated receiver voltage spectra with a 2% decrease in longitudinal velocity and shear velocity, while maintaining the other unchanged, are compared with the same experimental data shown in Fig. 4.9. Both the spectrum minima and and the shape are sensitive to even a variation as small as 2% in shear and longitudinal constants. The above analysis leads to a very straightforward material inversion procedure. We can first find shear velocity by using data at incident angles above longitudinal critical angle but below shear critical angle, then find longitudinal constants by using data obtained at incident angles below the longitudinal critical angle.

The above voltage spectrum calculation can be easily extended to anisotropic media and can be employed to characterize composite materials. we need only to use the plane-wave reflection coefficient from an anisotropic plate. The first composite material we study is a unidirectional graphite epoxy laminate. The reflection coefficient for this material is well documented in [21]. The unidirectional graphite epoxy can be regarded as transversely isotropic, so five elastic constants C_{11}, C_{12}, C_{22}, C_{23}, C_{44}, C_{55} determine the elastic behavior of the composite plate, where $C_{44} = (C_{22} - C_{23})/2$. The choice of incident angle is critical to the determination of certain elastic constants. Shown in Fig. 4.11 is the receiver voltage spectrum at an incident angle 10° and an offset $x_i = 6\,\text{mm}$ when the fiber direction is in the incident plane. All features of the receiver voltage spectrum are well reproduced by the theory. The minima are well aligned and the amplitude is well fitted. The spectrum at this incident angle can be used to deduce

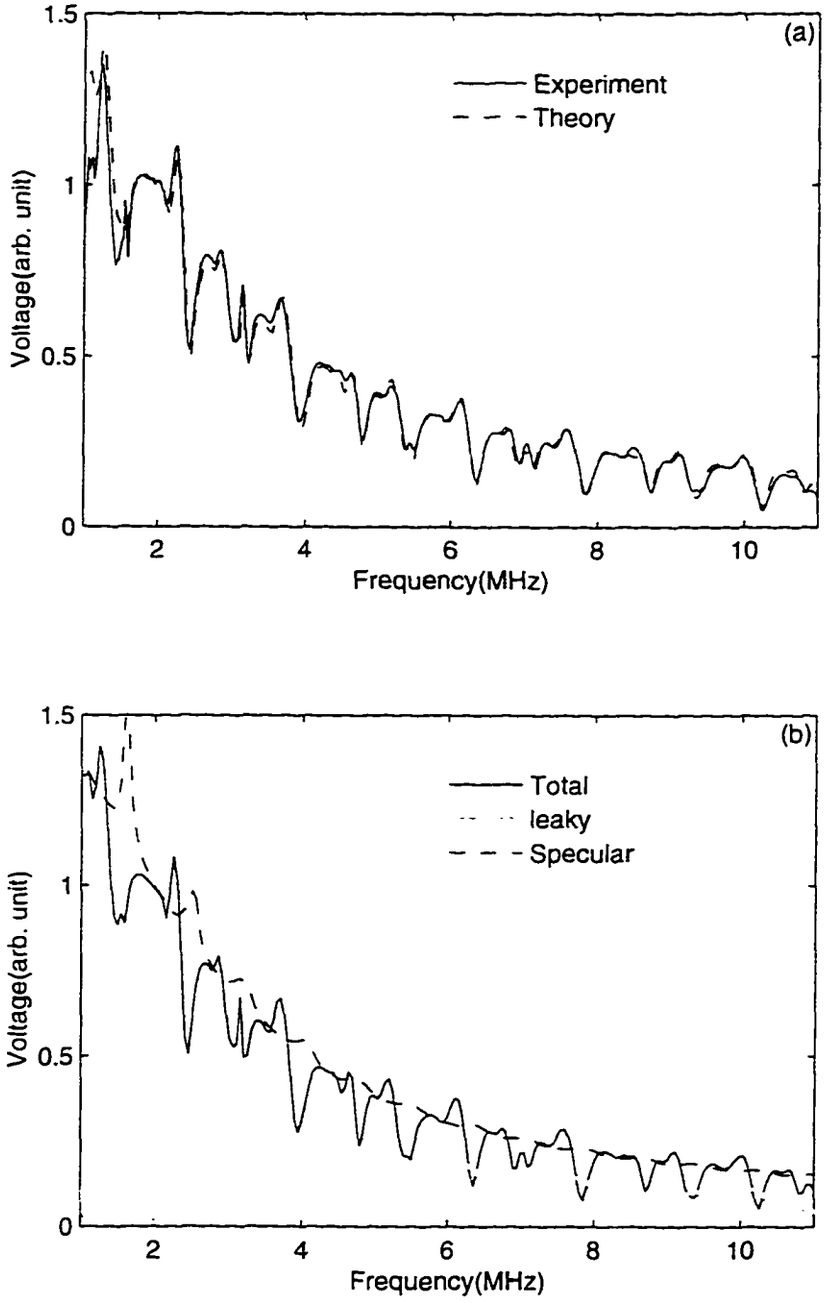

Figure 4.9 (a) Receiver voltage spectrum of a steel plate at 10° incidence and at a coordinate offset $x_i = 6$ mm; (b) separate contributions of leaky wave and specular reflection in the total receiver voltage spectrum.

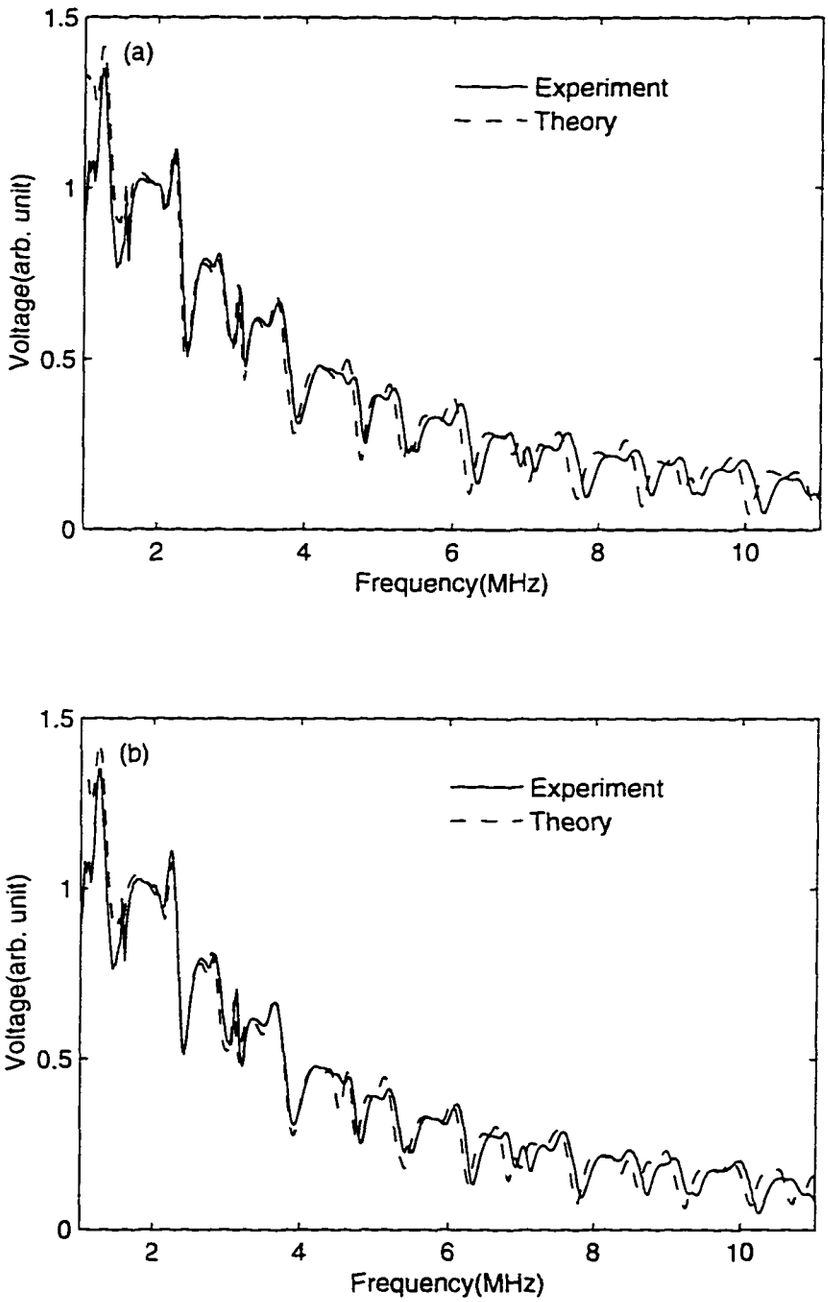

Figure 4.10 (a) Comparison of receiver voltage spectrum and theoretical calculation with a 2% decrease in the longitudinal velocity: (b) same comparison with a 2% decrease in the shear velocity.

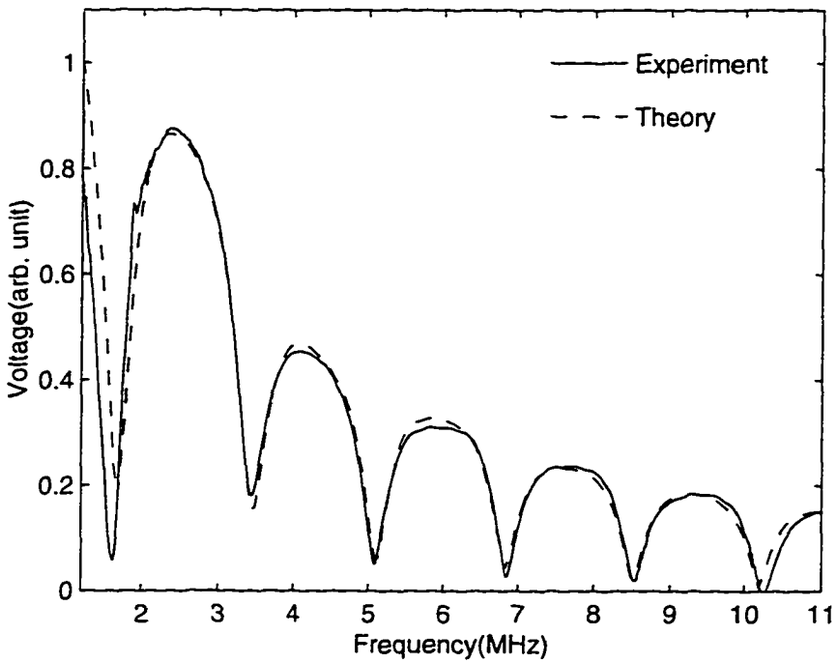

Figure 4.11 Receiver voltage spectrum from a unidirectional graphite epoxy at an incident angle 10°and a coordinate offset of 6 mm with the fiber direction in the incident plane.

C_{12} [22].

The receiver voltage spectrum at 20° incidence is strongly influenced by C_{33}, and this fact is verified by the experimental results shown in Fig. 4.12. Here, the offset is also 6 mm and the fiber direction is in the incident plane. The minimum and the amplitude of the receiver voltage spectrum is perfectly modeled by the theory. Some minor discrepancy above 10 MHz may result from the transducer response normalization.

The elastic constant C_{23} has no influence on the receiver voltage when the fiber direction is in the incident plane, but has pronounced effects on it when the fiber direction is normal to the incident plane. Such an example is shown in Fig. 4.13, where the incident angle is 20° and the offset is 6 mm, but fiber direction is normal to the incident plane. Although the receiver voltage spectrum is a bit complicated here, all features are well fitted by the theoretical calculation, even some very fine variations.

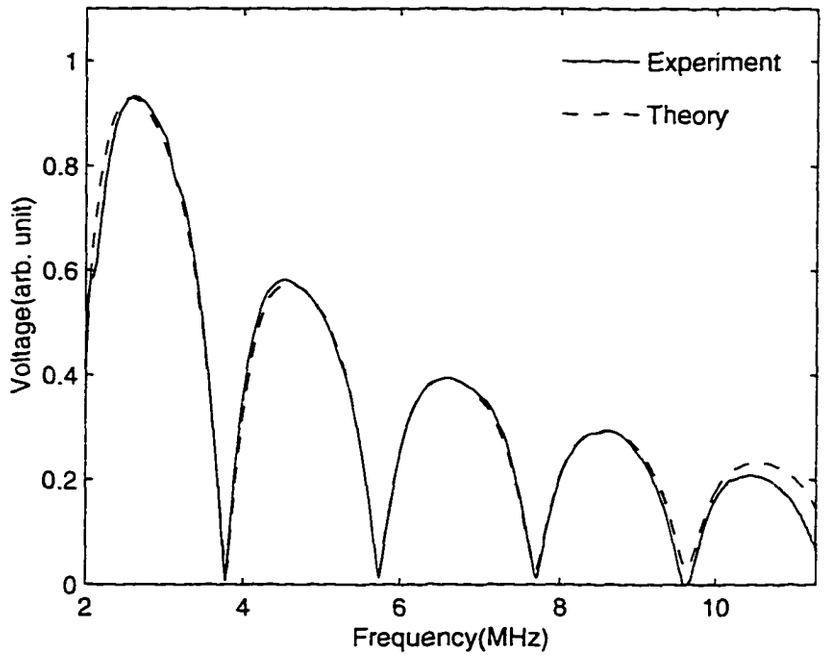

Figure 4.12 Receiver voltage spectrum from a unidirectional graphite epoxy plate at 20° incidence and at an offset of $x_i = 6$ mm with the fiber direction in the incident plane.

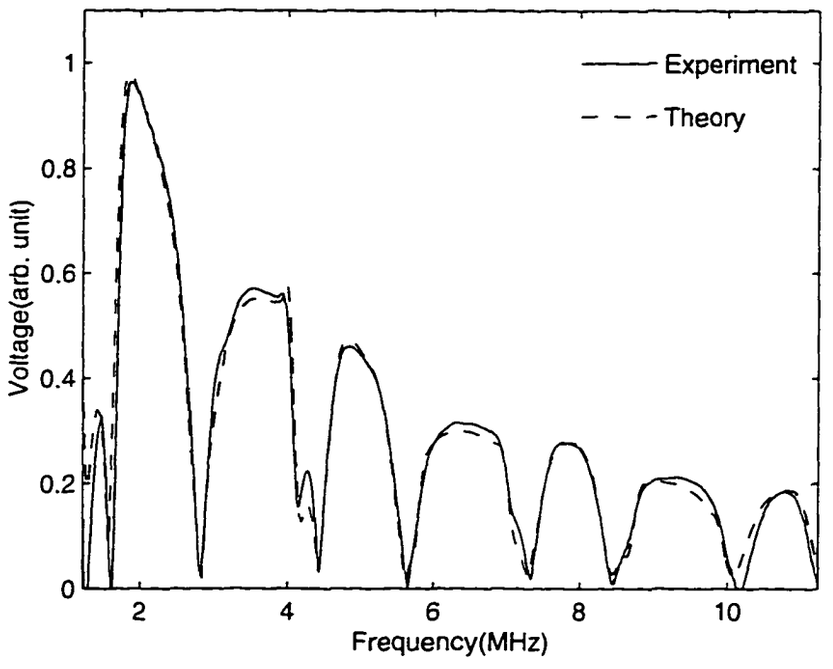

Figure 4.13 Receiver voltage spectrum from a unidirectional graphite epoxy plate at 20° incidence and at an offset of $x_i = 6$ mm with the fiber direction normal to the incident plane.

An even more complicated composite sample is represented by a 12-ply biaxial graphite epoxy plate. The ply configuration used in our experiments is $[0.90]_{3s}$. The elastic behavior of such a laminate can not be simply regarded as an orthotropic plate, especially at high ultrasonic frequencies. The stacking sequence of the lamina is important for the reflected voltage spectrum, so the simple reflection coefficient of a unidirectional graphite epoxy plate, mentioned above, can not be applied here. Instead, a reflection coefficient [8] derived using the transfer matrix will be incorporated into our voltage spectrum calculation.

Shown in Fig. 4.14 is the receiver voltage spectrum from the $[0.90]_{3s}$ biaxial composite laminate at 20° incidence and offset of 6 mm. The fiber direction in the top layer lies in the incident plane. The unusual characteristics shown here demonstrate the complexity resulting from the multilayer media. Even so, the results are also in good agreement with the theoretical receiver voltage spectrum calculation.

As in the case of the isotropic case, the receiver voltage spectrum calculation can also be applied to model the situation when the receiver is moved out of the specular region. Such an example is shown in Fig. 4.15, where the experimental conditions are the same as in Fig. 4.14, except that the receiver offset is 11 mm. The specular reflection still has a strong effect below 2 MHz because of the lower beam diffraction. Above that frequency, the leaky wave dominates the total voltage.

The fact that the theoretical receiver voltage spectrum can model the effects of the stacking sequence is presented in Fig. 4.16, where the experimental setup is the same as in Fig. 4.14, except that the top-layer fiber direction is normal to the incident plane. The spectral difference below 2 MHz between Fig. 4.16 and Fig. 4.14 is not significant, indicating that the laminate can be treated as an orthotropic plate at low frequency, but where completely different behavior exists above 2 MHz.

To further test our theoretical model calculations, we have performed experiments at a larger incident angle of 30°. The results are shown in Fig. 4.17 with the top-layer

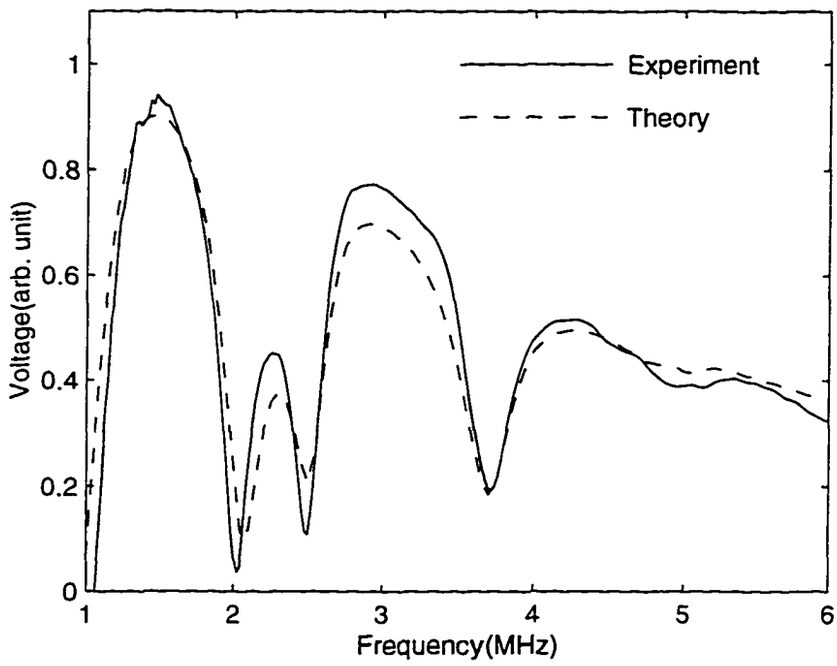

Figure 4.14 Receiver voltage spectrum from a biaxial graphite epoxy plate at 20° incidence and at an offset of $x_i = 6$ mm with the fiber direction in the top layer lying in the incident plane.

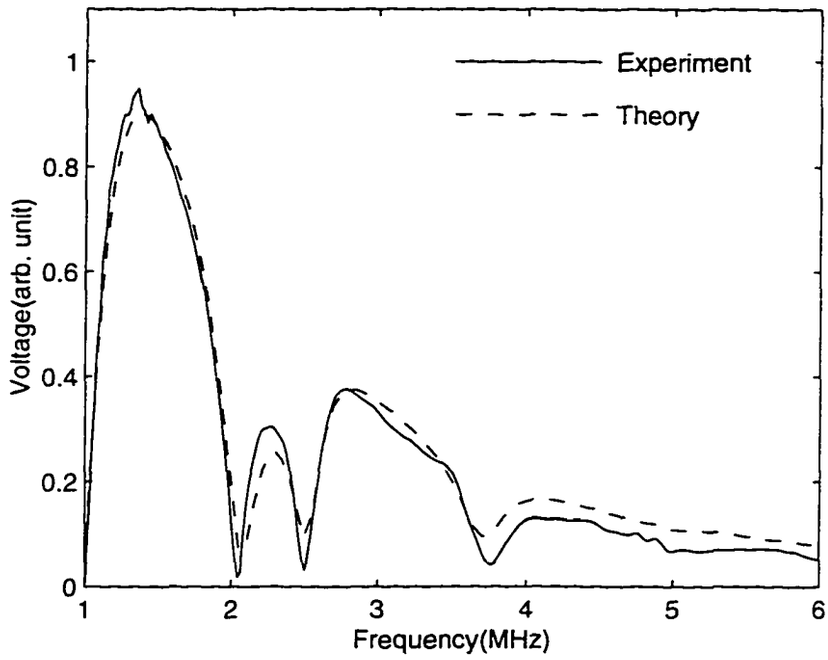

Figure 4.15 Receiver voltage spectrum from a biaxial graphite epoxy plate at 20° incidence and at an offset of $x_i = 11$ mm with the fiber direction in th top layer lying in the incident plane.

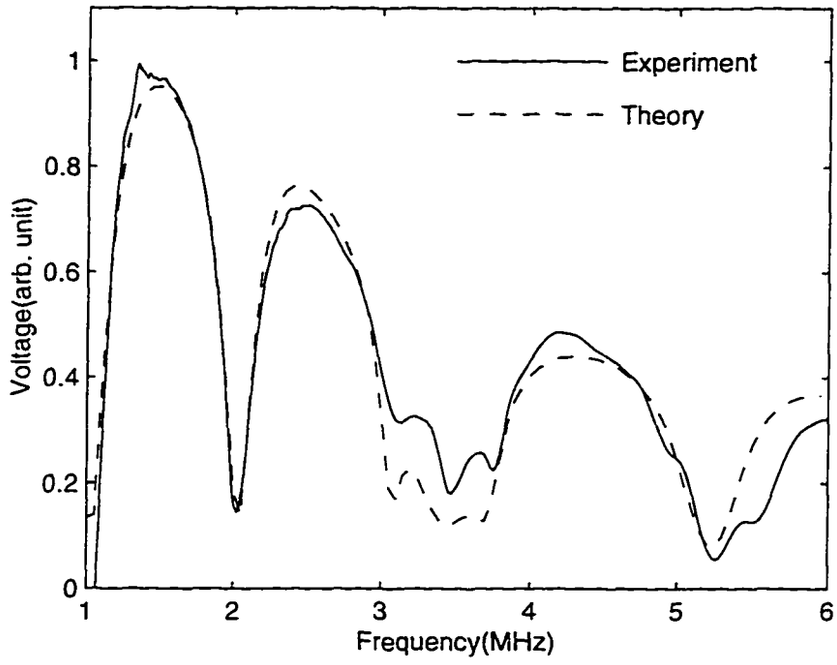

Figure 4.16 Receiver voltage spectrum from a biaxial graphite epoxy plate at 20° incidence and at an offset of $x_i = 6$ mm with the top-layer fiber direction lying normal to the incident plane.

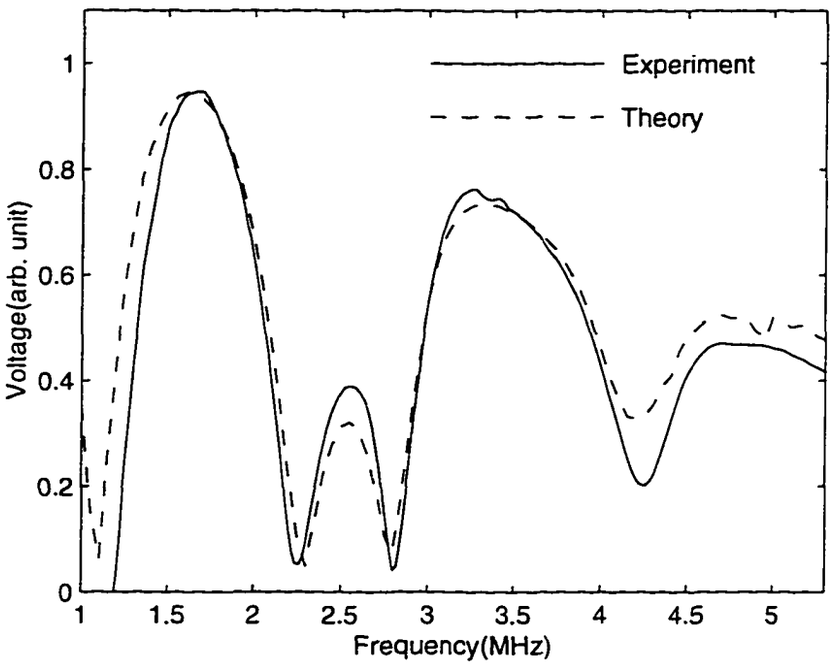

Figure 4.17 Receiver voltage spectrum from a biaxial graphite epoxy plate at 30° incidence and at an offset of $x_i = 6$ mm with the top-layer fiber direction in the incident plane.

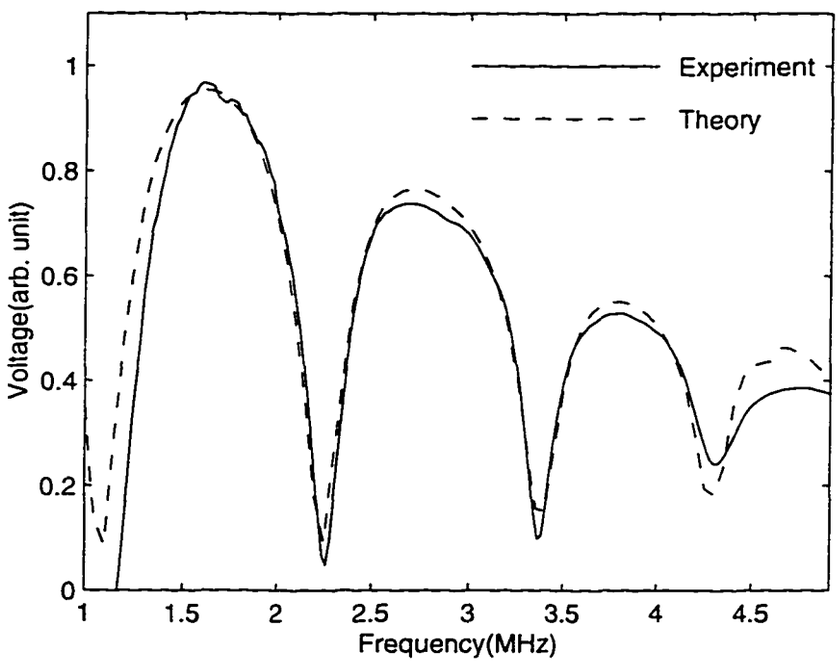

Figure 4.18 Receiver voltage spectrum from a biaxial graphite epoxy plate at 30° incidence and at an offset of $x_i = 6$ mm with the top-layer fiber direction normal to the incident plane.

fiber direction in the incident plane. In Fig. 4.18 the top-layer fiber direction is normal to the fibers, and for both figures the transducer offset is 6 mm. The risk of increasing the incident angle is that the reflection coefficient may not be stable because the large incident angle may put some wave components beyond the critical angle and evanescent waves result. The agreement between the experiments and theoretical calculations shown in Fig. 4.17 and Fig. 4.18 indicates that the instability of reflection coefficient does not occur here even at 30°. Compared with Fig. 4.14, Fig. 4.17 shows similar characteristics, except that the minima of the reflection spectrum move to the right, which is can be seen from a general knowledge of dispersion characteristics of Lamb waves. However, Fig. 4.18 is completely different from Fig. 4.16, even though in both cases the top-layer fiber direction is normal to the incident plane. The results in Fig. 4.17 and Fig. 4.18 indicate again that the reflection spectrum is sensitive to the stacking sequence of the laminate, which is very important for materials characterization.

Conclusion

In this chapter is presented a receiver voltage spectrum calculation, based on the complex transducer point (CTP) and supported by extensive experimental results. We have verified that a 3-D beam is generally necessary for the spectral calculation, while a 2-D beam is not accurate enough to model all features of the receiver voltage. The 3-D beam calculation can model the reflection spectrum measurement in all experimental configurations. We have discussed various materials characterization issues based on the model calculation as a potential application. In most cases the spectrum is sensitive to one or more elastic constants, and this fact enables precise materials characterization. We have also developed an algorithm for the asymptotic analysis of the reflection spectrum of isotropic plates, and this method will be extended to anisotropic materials in a future work.

References

[1] G. A. Deschamps. "Gaussian beam as a bundle of complex rays." Electron. Lett. **7**. 684–85 (1971).

[2] J. Pott and J. G. Harris. "Scattering of an acoustic Gaussian beam from a fluid-solid interface." J. Acoust. Soc. Am. **76**. 1829–38(1984).

[3] J. G. Harris and J. Pott. "Further studies of the scattering of an acoustic Gaussian beam from a fluid-solid interface." J. Acoust. Soc. Am. **78**. 1072–80 (1985).

[4] S. Zeroug. L. B. Felsen. "Nonspecular reflection of two- and three-dimensional acoustic beams from fluid-immersed plane-layered elastic structures." J. Acoust. Soc. Am. **95**. 3075–3098 (1994).

[5] S. Zeroug. L. B. Felsen. "Nonspecular reflection of two- and three-dimensional acoustic beams from fluid-immersed cylindrically layered elastic structures. " J. Acoust. Soc. Am. **98**. 584–598 (1995).

[6] D. E. Chimenti. J. Zhang. S. Zeroug and L. B. Felsen. "Interaction of acoustic beams with fluid-loaded elastic structures." J. Acoust. Soc. Am. **95**. 45–59 (1994).

[7] T. J. Cloutier. A. Safaeinili. D. E. Chimenti. S. Zeroug. and L. B. Felsen. "An experimental study of ultrasonic beam reflection from fluids loaded cylindrical shells." *Review of Progress in Quantitative NDE*. Vol. 14. eds. D. O. Thompson and D. E. Chimenti. (Plenum. New York). pp131–pp138 (1995).

[8] D. E. Chimenti. A. H. Nayfeh. "Ultrasonic reflection and guided wave propagation in biaxially laminated composite plates." J. Acoust. Soc. Am. **87**. 1409–1415 (1990).

[9] A. H. Nayfeh. D. E. Chimenti. "Propagation of guided waves in fluid-coupled plates of fiber-reinforced composite." J. Acoust. Soc. Am. **83**. 1736–43 (1983).

[10] D. E. Chimenti. A. H. Nayfeh. "Leaky Lamb waves in fibrous composite laminates." J. Appl. Phys.. **58**. 4531-8 (1985).

[11] H. L. Bertoni and T. Tamir. "Unified theory of Rayleigh-angle phenomena for acoustic beams at liquid-solid interfaces." Appl. Phys. (1973) **2** 157-172.

[12] L. E. Pitts. T. J. Plona. and W. G. Mayer."Theory of Nonspecular Reflection Effects for an Ultrasonic Beam Incident on a Solid Plate in a Liquid." IEEE Trans. Sonics. Ultrason. **SU-24**. 101-09 (1977).

[13] T. J. Plona. L. E. Pitts. and W. G. Mayer." Ultrasonic bounded beam reflection and transmission effects at liquid/solid-plate/liquid interface." J. Acoust. Soc. Am. **6**. 1324-1328 (1976).

[14] O. I. Lobkis. A. Safaeinili. D. E. Chimenti. "Precision ultrasonic reflection studies in fluid-coupled plates." J. Acoust. Soc. Am. **99**. 2727-2736 (1996).

[15] S. Zeroug. F. E. Stanke. and R. Burridge. "A complex-transducer-point model for emitting and receiving ultrasonic transducers." Wave Motion **24**. 21-40 (1996).

[16] Han Zhang. D. E. Chimenti. "Ultrasonic beam reflection from lossy layered cylindrical shells." to appear in Ultrasonics.

[17] Han Zhang. D. E. Chimenti. S. Zeroug. "Transducer misalignment effects on voltage amplitude in beam reflection from elastic structures." submitted to J. Acoust. Soc. Am..

[18] R. B. Thompson and E. F. Lopes. "The effects of focusing and refraction on Gaussian ultrasonic beams". J. Nondestruct. Eval. (1984) **4** 107-23.

[19] L. B. Felsen and N. Marcuvitz. *Radiation and Scattering of Waves* (Prentice Hall. Englewood Cliffs. 1973).

[20] Han Zhang. D. E. Chimenti. "Transmission coefficient reconstruction by using air couple ultrasound".

[21] D. E. Chimenti and A. H. Nayfeh. "Ultrasonic reflection and guided waves in fluid-coupled composite laminates." J. Nondetruct. Eval**9**. 51-69 (1990).

[22] S. I. Rokhlin and D. E. Chimenti. "Reconstruction of elastic constants from ultrasonic reflectivity data in a fluid coupled composite plate." *Review of Progress in Quantitative NDE.* vol. 9. Eds. D. O. Thompson and D. E. Chimenti. (Plenum. New York). 1411-1418 (1990).

GENERAL CONCLUSION

General Discussion

In this dissertation we have presented analysis and experiments on ultrasonic waves and their interaction with elastic structures. We have also seen how Gaussian beams can be constructed by displacing a real point source into the complex plane, where the beam properties are determined by the Fresnel length, which contains information on the characteristics of the transmitter, aperture size and frequency *et al.*. The same concept is applied to the receiver according to the reciprocal theorem. Thus, the Green's function in real space is analytically continued into the complex plane, which models the interaction two Gaussian beams. With the proper consideration of the transducer electronics, which can be measured by calibration, we obtain the predicted receiver voltage. For the problems of beam interaction with objects, the analytically continued Green's function is first decomposed into plane wave spectral components, and each component is multiplied by the plane-wave reflection or transmission coefficient. The solution is synthesized by weighting each spectral component by the appropriate value of the scattering coefficient.

Through high-frequency asymptotic reduction, we have obtained an analytical formula that can be implemented very easily. Such a general approach has been applied to solve four real ultrasonics problems of practical significance. The most important advantage of the complex source and receiver points is their mathematical elegance and the

ability to avoid integration over the transmitter and receiver aperture, while still giving accurate results. They also represent an example of how to extend known solutions to new problems in an economical way.

The theoretical development discussed here has been applied to the evaluation of numerous experiments. When a procedure alters the contribution of the Gaussian beam (such as performing a spatial Fourier transform on the scanned signal in Chapter 3 or changing the frequency of the incident beam in Chapter 4), the two-dimensional Gaussian sheet beam and three-dimensional rotationally symmetric Gaussian beam show differences, in some cases large ones. The theory developed in this work has assisted us in interpreting the experimental results and serves as a model for the inversion of material parameters.

In chapter 1, with the incorporation of the spring model to describe the boundary condition, a closed form of analytical solution has been obtained to analyze the signal. In Chapter 2 the CTP solution provides us a powerful tool to analyze the contribution of different signal components. Using only direct numerical calculation we might have missed important physics exposed by the analysis. In chapter 3 the theory provides an accurate model on which to base precise material elastic property inversion. In chapter 4 the asymptotic analytical model also gives a clear picture how the wave components of the detected signal vary as the frequency changes.

There are also some limitations of complex source points. The CSP behaves as a Gaussian beam only in the paraxial region, although this may not pose a serious problem for the results reported here because most of our experiments are performed in far field region of the transducer, and this beam condition is therefore always satisfied. All four of the problems discussed in this dissertation fall within the same theoretical framework, which demonstrates the versatility of the complex transducer point. The good agreement between experiment and theory indicates the accuracy of the total analytical picture, of which the CTP is an important part.

While the complex transducer point models a Gaussian beam having no sidelobes. it would be possible to combine several pairs of CTPs and thus describe model a beam with sidelobes. For the problems discussed here. one pair of CTPs provides enough accuracy for our purposes. This conclusion is based on a well proven observation that sidelobes are weakened. not strengthened. as a result of two identical beams interacting with each other.

Recommendations for Future Research

Our present study is limited to the beams reflected from plates. shells. and solid cylinders or to the transmitted beam through plates. In other words. we study the field external to the objects. That is certainly sufficient for our present study of guided wave mode conversion at fluid-solid interfaces. The complex transducer point could be extended. however. to calculate the field inside the solid material and analyze the stresses or displacements created internally by the incident acoustic waves. thereby enhancing material inspection.

Complex transducer points can also be used to model focused transducers. In that case the location of beam waist will depart from the transducer aperture. One would need to modify all the analysis by first translating the real position of focused beam to an imaginary location. the distance moved depending on the transducer curvature: next. one displaces the imaginary source into the complex plane.

We are also currently engaged in developing a computer algorithm to calculate the receiver voltage. considering the dependence of the reflection or transmission coefficient on angular coordinate. This development would facilitate the inspection of composite materials in any orientation.

On the experimental side. we have already employed pulse compression technology to speed the data acquisition while acquiring information over a broad frequency range.

We also propose to extend this technology to air-coupled ultrasound to extract as much information as rapidly as possible.

APPENDIX A TRANSFER MATRIX AND MORE RESULTS OF CHAPTER 1

Transfer Matrix

Here, we derive the transfer matrix used in Chapter 1 of the thesis. For a single plate of thickness d, as shown in Fig. A.1, there exist longitudinal waves propagating along positive z with amplitude A_l^+ and propagating along $-z$ with amplitude A_l^-, and transverse waves propagating along $+z$ with amplitude A_t^+ and propagating along $-z$ with amplitude A_t^-. They can be described by displacement potentials.

$$o = A_l^+ e^{i(kx+\kappa_l z)} + A_l^- e^{i(kx-\kappa_l z)} \tag{A.1}$$

$$v = A_t^+ e^{i(kx+\kappa_t z)} + A_t^- e^{i(kx-\kappa_t z)}. \tag{A.2}$$

where the displacement is readily obtained from the gradient of the potential o and v by

$$u = ike^{i\kappa_l z} A_l^+ + ike^{-i\kappa_l z} A_l^- - i\kappa_t e^{i\kappa_t z} A_t^+ + i\kappa_t e^{-i\kappa_t z} A_t^- \tag{A.3}$$

$$w = i\kappa_l e^{i\kappa_l z} A_l^+ - i\kappa_l e^{-i\kappa_l z} A_l^- + ike^{i\kappa_t z} A_t^+ + ike^{-i\kappa_t z} A_t^- . \tag{A.4}$$

In the above equation, a common term e^{ikx} is omitted. The stress components σ_{xz} and σ_{zz} can be calculated from the constitutive relation, $\sigma_{ij} = \lambda\epsilon_{kk}\delta_{ij} + 2\mu\epsilon_{ij}$. Let $z = 0$ and $z = -d$ in the Eq. (A.4) and the derived σ_{xz} and σ_{zz}, and we get the displacement and stress at the lower and upper interfaces.

$$z = 0 \quad \{b_i^-\} = [D_{ij}^{(-)}]\{A_j\} \tag{A.5}$$

$$z = -d \quad \{b_i^+\} = [D_{ij}^{(+)}]\{A_j\}. \tag{A.6}$$

where $\{b_i^-\} = [u^-, w^-, \sigma_{zz}^-, \sigma_{xz}^-]^T$ is the displacement-stress vector in the lower interface of the layer. $\{b_i^+\} = [u^+, w^+, \sigma_{zz}^+, \sigma_{xz}^+]^T$ is the displacement-stress vector in the upper interface of the layer. $\{A_j\} = [A_l^+, A_t^+, A_l^-, A_t^-]^T$ is the amplitude vector of displacement potential, and $[D_{ij}^{(-)}]$ and $[D_{ij}^{(+)}]$ are given by

$$[D_{ij}^{(-)}] = \begin{bmatrix} ike^{-L} & -i\kappa_t e^{-T} & ike^{L} & i\kappa_t e^{T} \\ i\kappa_l e^{-L} & ike^{-T} & -i\kappa_l e^{L} & ike^{T} \\ -2Ak\kappa_l e^{-L} & A(\kappa_t^2 - k^2)e^{-T} & 2Ak\kappa_l e^{L} & A(\kappa_t^2 - k^2)e^{T} \\ Be^{-L} & -2A\kappa_t k e^{-T} & Be^{L} & 2A\kappa_t k e^{T} \end{bmatrix}. \tag{A.7}$$

$$[D_{ij}^{(+)}] = \begin{bmatrix} ik & -i\kappa_t & ik & i\kappa_t \\ i\kappa_l & ik & -i\kappa_l & ik \\ -2Ak\kappa_l & A(\kappa_t^2 - k^2) & 2Ak\kappa_l & A(\kappa_t^2 - k^2) \\ B & -2A\kappa_t k & B & 2A\kappa_t k \end{bmatrix}. \tag{A.8}$$

Here, $A = \rho c_t^2$, $B = -\rho\omega^2 + 2\rho c_t^2 k^2$, $L = i\kappa_l d$ and $T = i\kappa_t d$. Eliminating $\{A_j\}$ from Eq. (A.5) and Eq. (A.6), we obtain the transfer equation.

$$\{b_i^+\} = [C_{ij}]\{b_j^-\}. \tag{A.9}$$

where

$$[C_{ij}] = [D_{ij}^{(+)}][D_{ij}^{(-)}]^{-1}. \tag{A.10}$$

This is the expression we use in Chapter 1.

More Experimental Results

We also present some experimental results and theoretical calculation that not included in the paper. These results certainly help us better understand the various issues

behind the phenomena discussed in the paper. Although we have shown two time-domain waveforms, one from the well-bonded region, the other from the debond region, they can not describe the whole wave propagation procedure. In order to record the whole wave propagation procedure, we stack all time-domain waveforms vertically by observation angle, and the results are shown in Fig. A.2. In the figure, the horizontal axis is time, the vertical axis is the observation angle, and the gray scale is the amplitude of the waveform. In the bond region (Fig. A.2(a)) the specular reflection and leaky wave are gradually separated with increasing observation angle, owing to velocity differences between the specular reflection and leaky wave. In a debond region (Fig. A.2(b)) no such separation appears, since only the specular reflection exists.

We prove that the damping in the rubber only plays the role of a scale factor in the receiver voltage signal, and we have mentioned the effect of the rubber damping loss on the zeros and poles of the two-layer structure. The results can be seen in Fig. A.3. Here, the imaginary part of A_0 pole, zero, and their difference are plotted as a function of rubber damping. Three curves that parallel the horizontal axis indicate that the imaginary part of the pole and zero are independent of rubber damping.

Besides the signal voltage distribution presented in the paper, the signal voltage distribution at some other incident angles is also measured and calculated. An example at an incident angle of 38°, 3° grater that the A_0 mode phase matching angle, is shown in Fig. A.4. Both the receiver voltage of the bare shell and that of the layered shell are well predicted by the theory. The disappearance of the first peak in the main lobe for the bare shell results from the interference cancellation of the excited leaky wave, while the leaky wave in layered shell is not strong enough to make such a cancellation apparent.

Another receiver signal voltage distribution we have measured and calculated is at 31° incidence, shown in Fig. A.5. Although 31° is far from the A_0 mode phase matching angle, the leaky wave can still be discerned in the experiment. The feature resulting

from the deviation of incident angle from the phase matching angle is the dip that moves to the right and the decrease in the second peak. The weaker leaky wave in the layered shell than in the bare shell is much more obvious here.

As a general comparison of leaky waves at incident angles near the A_0 mode phase angle, we plot the calculated leaky wave at incident angles of 35°, 33°, 38°, and 31° in one graph, which is shown in Fig. A.6. The calculation done here takes advantage of the asymptotic reduction of the spectral integrals. Frame (a) is the bare shell, and frame (b) is the layered shell. The figure shows the relative position and amplitude of leaky waves excited at the different experimental incident angles. The sharp peak of the leaky wave at 35° incidence (solid curve) is at the observation angle of 0°, indicating a strong phase matching with the A_0 leaky mode. When the incident angle deviates from the phase matching angle, the amplitude decreases and the position of the peak shifts. Above this incident angle at 38° (dashed curve), the leaky wave shifts to the left. Below the phase matching angle, 33° (dash-dot curve) and 31° (dotted curve), the leaky wave shifts to the right. This effect results from the movement of the saddle point with different incident angles. If we compare frames (a) and (b), we can see that the relative proportion of the leaky wave in the total reflected signal for the layered shell is smaller than that in the bare shell.

As a last issue we apply what we have found through our investigations on the phenomenology to practical NDE. Since there is no leaky wave in the debond region, we can put a signal gate at the leaky wave position when the receiver is at the observation angle where the specular and leaky waves are well separated. By summing the absolute value of the waveform in the gate and moving transmitter and receiver simultaneously, we obtain the C-scan image shown in Fig. A.7. This image is obtained at an observation angle of 25° and an incident angle of 38°, where the time gate is 11μs in length. The debond region is quite apparent.

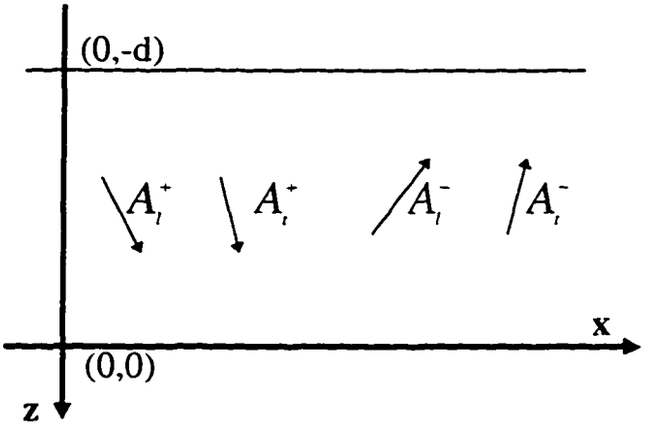

Figure A.1 Plate used in the derivation of transfer matrices, showing longitudinal and transverse waves propagating in the negative and positive directions.

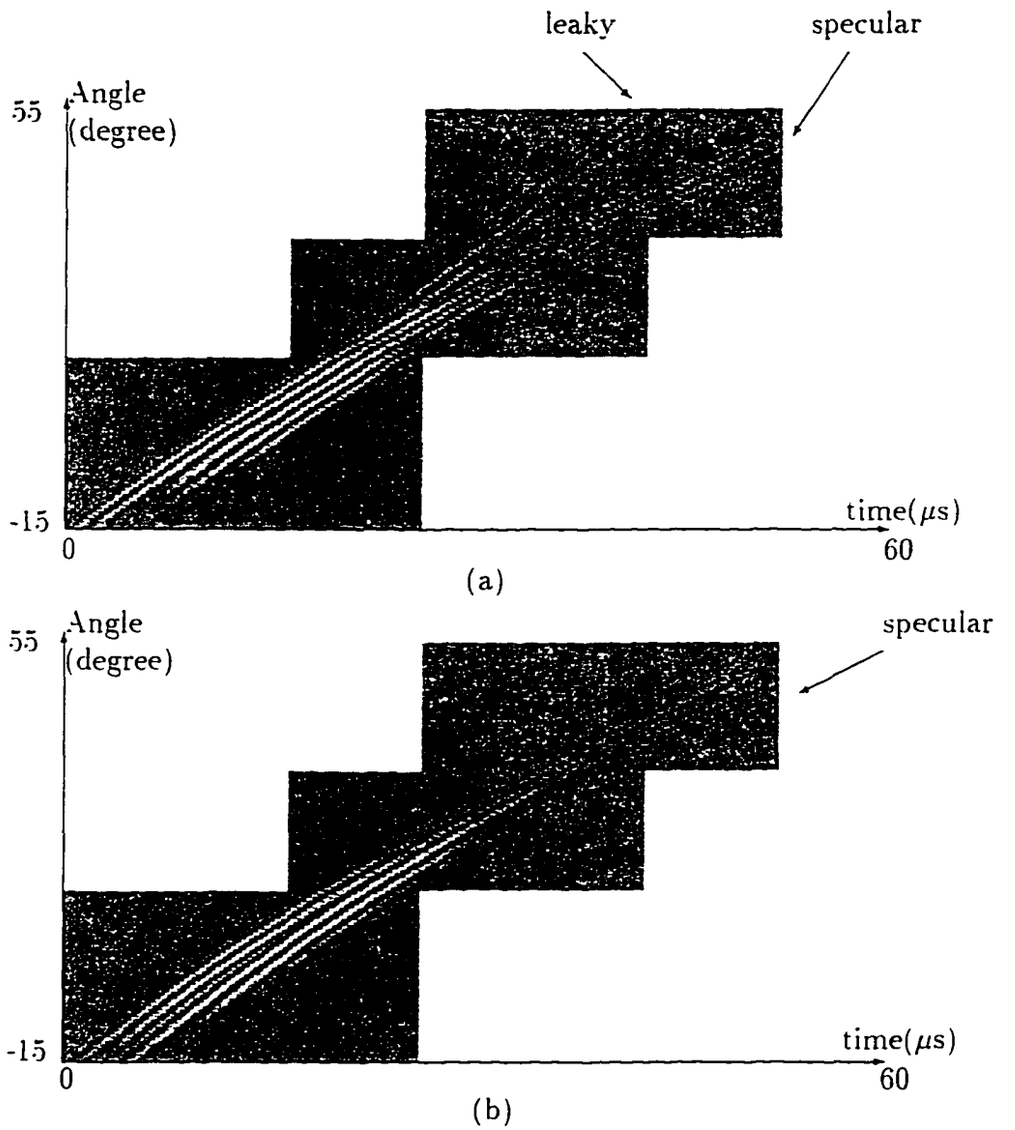

Figure A.2 Stack of time-domain waveforms by observation angle in the bond region (a), and in the debond region (b).

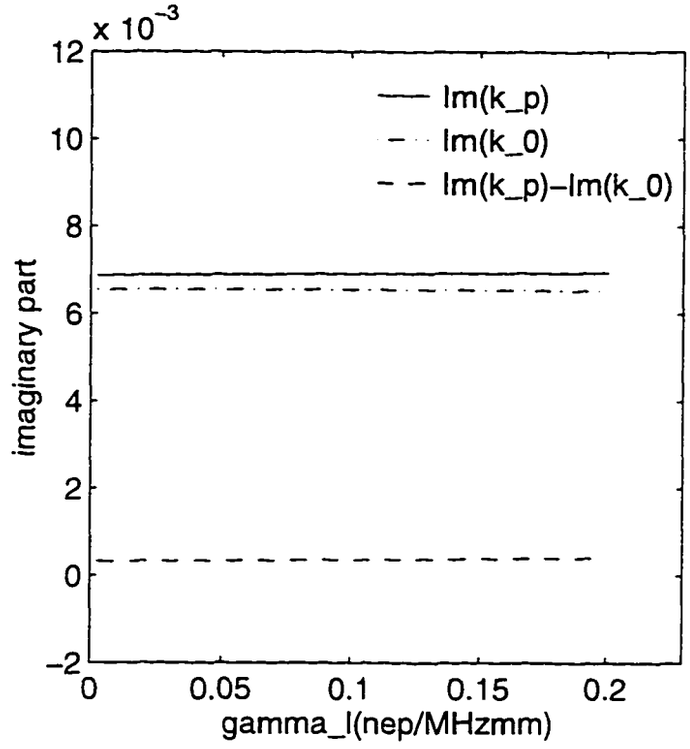

Figure A.3 Imaginary part of A_0 pole k_p (solid curve), zero k_0 (dashed curve) and their difference $\Im(k_p) - \Im(k_0)$ as a function of rubber damping γ_l ($\gamma_t = \gamma_l/2$, $kkt = 10^{12}$ N/m^3, $kkn = 20^{12}$ N/m^3.)

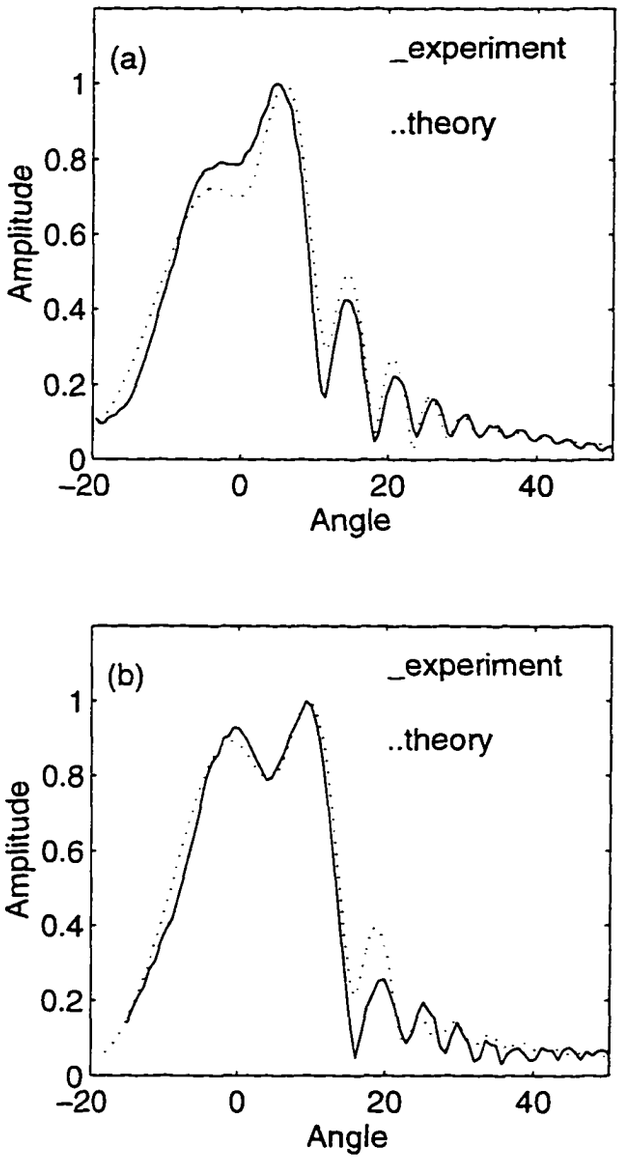

Figure A.4 Receiver voltage from a) bare steel shell; b) bonded region of rubber-steel at an incident angle 38°.

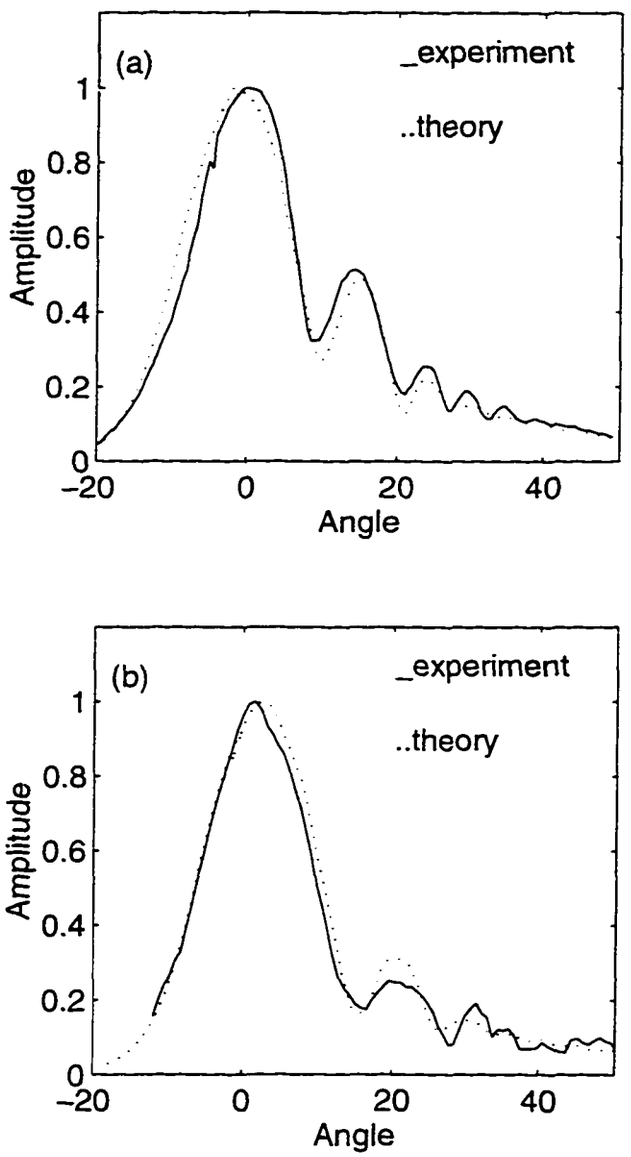

Figure A.5 Receiver voltage from a) bare steel shell: b) bond region of rubber-steel at an incident angle 31°.

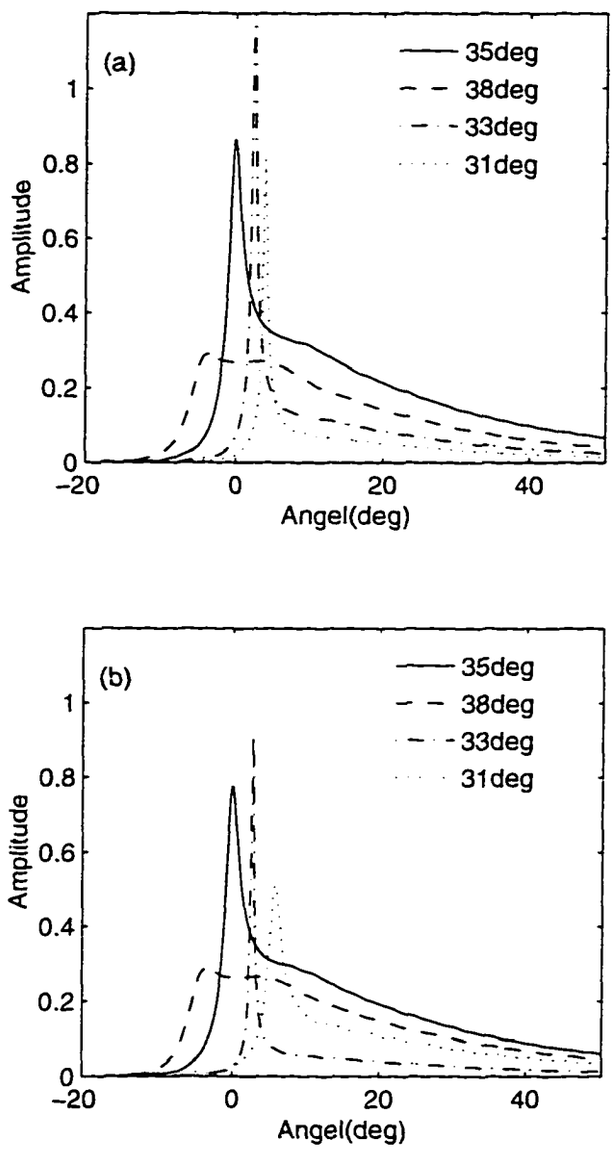

Figure A.6 Comparison of leaky waves at different incident angles:(a) bare steel shell; (b) bonded region of rubber-steel shell, showing the relative amplitude and position of leaky waves.

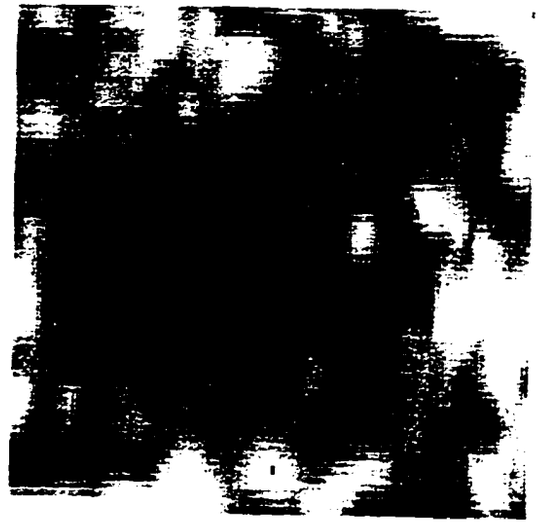

Figure A.7 C-scan image obtained at 38° incidence and at an observation angle of 25°.

APPENDIX B THEORETICAL VOLTAGE FORMULA WITH POLE AND SADDLE POINT PATH OF CHAPTER 2

In this section we will present for convenience and completeness the complete theoretical voltage formula used in the calculation of Chapter 2. This development may also be found in the references cited in Chapter 2. We also present some results that are not included in the paper (Chapter 2). These results facilitate understanding of the misalignment effects.

Theoretical Voltage Formula

The spectral integral of the receiving transducer voltage in reflection from a planar structure is

$$V_{\mathcal{R}} = \frac{-\gamma(\omega)\omega\rho_f A_{\mathcal{T}} A_{\mathcal{R}}}{8\pi^2} \int_{-\infty}^{\infty} R(k_x) \frac{\exp\left\{i\tilde{P}^r(k)\right\}}{\kappa_f} dk_x . \tag{B.1}$$

where

$$\kappa_f = \sqrt{k_f^2 - k_x^2}. \qquad k_f = \omega/c_f . \tag{B.2}$$

Here, c_f and ρ_f are the fluid velocity and density, and ω is the angular frequency. $A_{\mathcal{T}}$ and $A_{\mathcal{R}}$ specify the strength of transmitter and receiver, $\gamma(\omega)$ is temporal spectrum of transducer devices, and R is plane-wave reflection coefficient (RC). The phase function $\tilde{P}^r$ is defined as,

$$\tilde{P}^r(k) = k(x_{\mathcal{R}} - x_{\mathcal{T}}) - \kappa_f(y_{\mathcal{R}} - y_{\mathcal{T}}) . \tag{B.3}$$

The integral in Eq. (B.1) can be evaluated asymptotically by noting that the integrand is stationary only in the vicinity of the saddle point. We can, therefore, deform the integration from the real k_x axis into a steepest descent path in the complex plane and evaluate the integral at the saddle point. Because the saddle point and the singularities of the reflection coefficient can occur in close proximity, we must be careful in our application of the saddle point method. As pointed out in Chapter 4, this problem has been solved by Felsen and Marcuvitz. Accounting for the contribution from the RC poles, Felsen and Marcuvitz obtain a uniform asymptotic expression.

$$\begin{aligned} V_{\mathcal{R}}(\underline{r};\underline{r}') \sim\ & \frac{-i}{4\pi}\gamma(\omega)\omega\rho_f A_{\mathcal{T}} A_{\mathcal{R}} \times \\ & \frac{\exp\{i\pi/4\}}{2\sqrt{2\pi}} R(\tilde{k}_s)\frac{\exp\{ik_f(\tilde{L}'+\tilde{L})\}}{\sqrt{k_f(\tilde{L}'+\tilde{L})}} \\ & -\frac{1}{2}\sum_{j=1}^{M}\frac{Res\{R(k)\}_{k_{p_j}}}{\kappa_f|_{k_{p_j}}}\exp\left\{i\tilde{P}^r(k_{p_j})\right\}\tau(-i\tilde{s}_{p_j}). \end{aligned} \tag{B.4}$$

where $\tilde{k}_s$ is the saddle point and $\tilde{k}_{p_j}$ is the jth pole of the reflection coefficient. Then,

$$\tilde{k}_s = k_f \sin\left(\tilde{\theta}_s\right). \quad \tilde{\theta}_s = \tan^{-1}[-(x_{\mathcal{R}} - x_{\mathcal{T}})/(y_{\mathcal{R}} - y_{\mathcal{T}})]. \tag{B.5}$$

The complex distance functions $\tilde{L}'$ and $\tilde{L}$ (from the source/receiver to the interface) are defined in terms of the complex saddle point angles and the positions of the source and receiver, respectively,

$$\tilde{L}' \equiv -\tilde{y}'/\cos\tilde{\theta}_s, \quad \tilde{L} \equiv -y/\cos\tilde{\theta}_s. \tag{B.6}$$

The quantity $\tilde{s}_{p_j}$ is a measure of the distance between the jth complex pole and the saddle point, called the "numerical distance".

$$\tilde{s}_{p_j} = \sqrt{i\left[\tilde{P}^r(\tilde{k}_s) - \tilde{P}^r(k_{p_j})\right]}. \tag{B.7}$$

The transition function is defined as,

$$\tau(-i\tilde{s}_{p_j}) = -\frac{\exp\left\{-(-i\tilde{s}_{p_j})^2\right\}}{2\sqrt{\pi}(-i\tilde{s}_{p_j})} + \frac{1}{2}\mathrm{erfc}(-i\tilde{s}_{p_j}). \tag{B.8}$$

and accounts for the interaction between the specular and nonspecular components in the reflected signal. The complex complementary error function is defined by.

$$\mathrm{erfc}(x) = \frac{2}{\sqrt{\pi}} \int_x^\infty \exp(-t^2)\, dt. \tag{B.9}$$

By contrast. for a cylindrical surface the spectral integral of the receiving transducer voltage is given by

$$\begin{aligned} V_R(\underline{\tilde{r}}:\underline{\tilde{r}}') &= \frac{-1}{16\pi}\gamma(\omega)\omega\rho_f A_T A_R \int_{-\infty}^{+\infty} R(\nu)\frac{H_\nu^{(2)}(k_f a)}{H_\nu^{(1)}(k_f a)} \\ &\quad \times H_\nu^{(1)}(k_f \tilde{r}') H_\nu^{(1)}(k_f \tilde{r}) \exp\left\{ i\nu\left[\tilde{o} - \tilde{o}'\right]\right\} d\nu. \end{aligned} \tag{B.10}$$

where a is the radius of the cylinder. $H_\nu^{(n)}$ is the nth-order Hankel function. All other quantities follow the same definition as given for planar structures. Similarly. this integral can be evaluated by uniform asymptotics. except that the Hankel functions must first be approximated by their Debye decompositions. The resulting expression in this case is

$$\begin{aligned} V_R(\underline{\tilde{r}}:\underline{\tilde{r}}') \sim\ & \frac{i}{2\pi}\gamma(\omega)\omega\rho_f A_T A_R \times \\ & \left[R(\nu_s)\frac{\exp\{i\pi/4\}}{2\sqrt{2\pi}} \frac{\exp\left\{ik_f\left(\tilde{L}' + \tilde{L}\right)\right\}}{\sqrt{k_f\left(\tilde{L}' + \tilde{L}\right)}} \sqrt{\left.\frac{a\left(\tilde{L}' + \tilde{L}\right)\sin\gamma_a}{2\tilde{L}'\tilde{L} + a\left(\tilde{L}' + \tilde{L}\right)\sin\gamma_a}\right|_{\tilde{\nu}_s}} \right. \\ & \left. -\frac{1}{2}\sum_{j=1}^{M} \frac{\mathrm{Res}\left\{R(\nu_{p_j})\right\}}{k_f(r\tilde{r}'\sin\gamma\sin\tilde{\gamma}'|_{\nu_{p_j}})^{1/2}} \exp\left\{i\tilde{P}^r(\nu_{p_j})\right\}\tau(-i\tilde{s}_{p_j}) \right]. \end{aligned} \tag{B.11}$$

where

$$\tilde{P}^r(\nu) = k_f\left(\tilde{r}\sin\gamma + \tilde{r}'\sin\tilde{\gamma}' - 2a\sin\gamma_a\right) - \nu\left(\gamma + \tilde{\gamma}' - 2\gamma_a - \left[\tilde{o} - \tilde{o}'\right]\right) \tag{B.12}$$

$$\tilde{L}' = \tilde{r}'\sin\tilde{\gamma}' - a\sin\gamma_a|_{\tilde{\nu}_s} \qquad \tilde{L} = \tilde{r}\sin\gamma - a\sin\gamma_a|_{\tilde{\nu}_s}. \tag{B.13}$$

$$\gamma = \cos^{-1}\left(\frac{\nu}{k_f\tilde{r}}\right). \quad \tilde{\gamma}' = \cos^{-1}\left(\frac{\nu}{k_f\tilde{r}'}\right). \quad \gamma_a = \cos^{-1}\left(\frac{\nu}{k_f a}\right). \tag{B.14}$$

Here. ν_s is the saddle point. determined by the following equation.

$$\cos^{-1}\left(\frac{\tilde{\nu}_s}{\tilde{r}}\right) + \cos^{-1}\left(\frac{\tilde{\nu}_s}{k_f\tilde{r}'}\right) - 2\cos^{-1}\left(\frac{\tilde{\nu}_s}{k_f a}\right) = \left[o - \tilde{o}'\right]. \tag{B.15}$$

and where $\tau(-is_{p_j})$ is the transition function and dependent on the numerical distance, following the same definition as with planar structures, and ν_{p_j} is jth reflection coefficient pole.

Pole and Loci of Saddle Points

As mentioned earlier, the asymptotic evaluation allows the evaluation of the separate contributions of the leaky wave and specular reflection. The strength of the leaky wave pole increases with its proximity to the saddle point, so it would be helpful to plot the saddle point and RC poles on a graph and make direct comparisons. Before we present these results, however, we plot the reflection coefficient of the stainless steel plate used in the experiment at 1 MHz: this result is shown in Fig. B.1. There exist four modes, A_0, S_0, A_1 and S_1 mode, corresponding to a phase matching angle of 32.8°, 27.9°, 14.98°, and 14.15°, respectively.

The saddle point loci (as a function of scan distance) at different receiver angles from 30.8°to 34.8°for an incident angle of 32.8° are plotted in Fig. B.2(b). The saddle point moves because at different scan distances, the experimental geometry changes. Here, the A_0 pole (plus sign) and the S_0 pole (open circle) are also shown. As the receiver angle increases, the saddle point loci move close to the A_0 pole and eventually pass the A_0 pole at a receiver angle of 30.8°. The leaky wave is most efficiently detected by the receiver when it is placed at an angle of 31.8°and a scan distance of ?? mm. The reason is because the saddle point locus corresponding to 31.8° and ?? mm almost intercepts the A_0 pole. When the receiver is at an angle of 30.8°, the leaky wave is weaker, as is the case for all other angles different from the incident angle. This strength ranking is confirmed in the amplitude plot in Fig. B.2(a).

A similar plot for the leaky wave amplitude distribution and saddle point loci for incident angles of 30° and 28° are shown in Fig. B.3 and Fig. B.4. Comparing the loci

of saddle points in Fig. B.3(b) and Fig. B.4(b), we see that the former lie close to the A_0 pole (plus sign), and the latter lie close to the S_0 pole (open circle). We also find that the two cases show remarkable symmetry about a single curve of saddle point loci that lies directly between the two RC poles, the A_0 pole and the S_0 pole. This curve can be the result of incidence at 30° and reception at 28° (as it is for the A_0 mode) or vice-versa. In Fig. B.3(b) and Fig. B.4(b), we see that changing the receiver angle in either case displaces the curve of saddle point loci to one or the other side of the central curve.

The corresponding leaky wave amplitude distributions also show similar characteristics, since in either case they lie exactly between the A_0 and S_0 poles. Along this curve of saddle point loci both modes are detected by the receiver and show strong interference. At the two extremes of the receiver angle, the leaky wave amplitude distributions for 32° (A_0 mode) and that for 26° (S_0 mode) show a monotonic decrease, because one strongly favors detection of the A_0 and the other favors detection of the S_0 mode. The amplitude distributions at other receiver angles can be similarly paired, *i.e.* 31° to 27° 30° to 28°, and so forth. We have already presented the effect of misalignment on the specular reflection by measuring at an incident angle far from any phase matching angle. These results can be generalized to an incident angle close to any phase matching angle. Although the generalization is very reasonable, it is confirmed in Fig. B.5. Here, the specular reflections of different receiver angles at an incident angle of 28° are plotted, clearly showing that the specular reflection decreases as the receiver angles are misaligned from the incident angles.

A different leaky wave distribution occurs with misalignment from an incident angle of 16°. The saddle point loci and the leaky wave distribution at different receiver angles are shown in Fig. B.6. From frame (b) we see that the two poles, A_1 and S_1, are very close to each other. The saddle point loci lie on one side of the poles. The decrease of receiver angle favors both two modes simultaneously and results in an increase of

the amplitude distribution of leaky waves in frame (a). These two figures provide a straightforward explanation of these phenomena observed in Fig. 2.7 of Chapter 2.

The above scenario can be easily extended to cylinders and shells. The leaky wave amplitude distribution and the saddle point loci of different receiver angles at an incident angle 20° are shown in Fig. B.7. Although the saddle point loci in this case are far from the Rayleigh pole, the leaky wave can still be discerned, as noted in Chapter 2. The increase in receiver angle moves the saddle point loci closer to the Rayleigh pole and results in a more efficiently received leaky Rayleigh wave, as shown in frame (a).

Leaky wave distributions and saddle point loci for incidence at the Rayleigh angle on a fluid-loaded steel cylinder are shown in Fig. B.8. The Rayleigh pole lies on the curve of saddle point loci for a receiver angle of 27°, indicating an efficiently received Rayleigh wave, seen as a deep minimum in the receiver voltage shown in the figure in Chapter 2. The ordering of the strength of leaky wave amplitude distributions at different receiver angles in frame (a) of the figure follows the relative distances from the curves of saddle point loci to the Rayleigh pole.

As an example of misalignment in the case of the steel shell, Fig. B.9 shows the leaky wave amplitude distributions for different receiver angles when the incident angle is 35°, as seen in frame (a). The corresponding curves of saddle point loci are shown in frame (b). The overall appearance is similar to the cylinder case, except that here we have a Lamb A_0 pole instead of the Rayleigh pole.

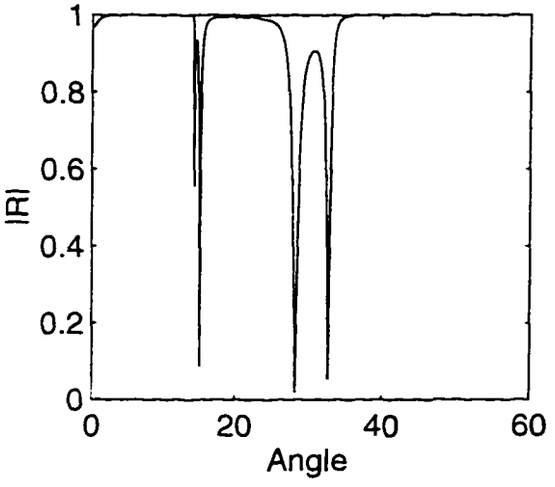

Figure B.1 Magnitude of the reflection coefficient of the 3 mm stainless steel plate at 1 MHz.

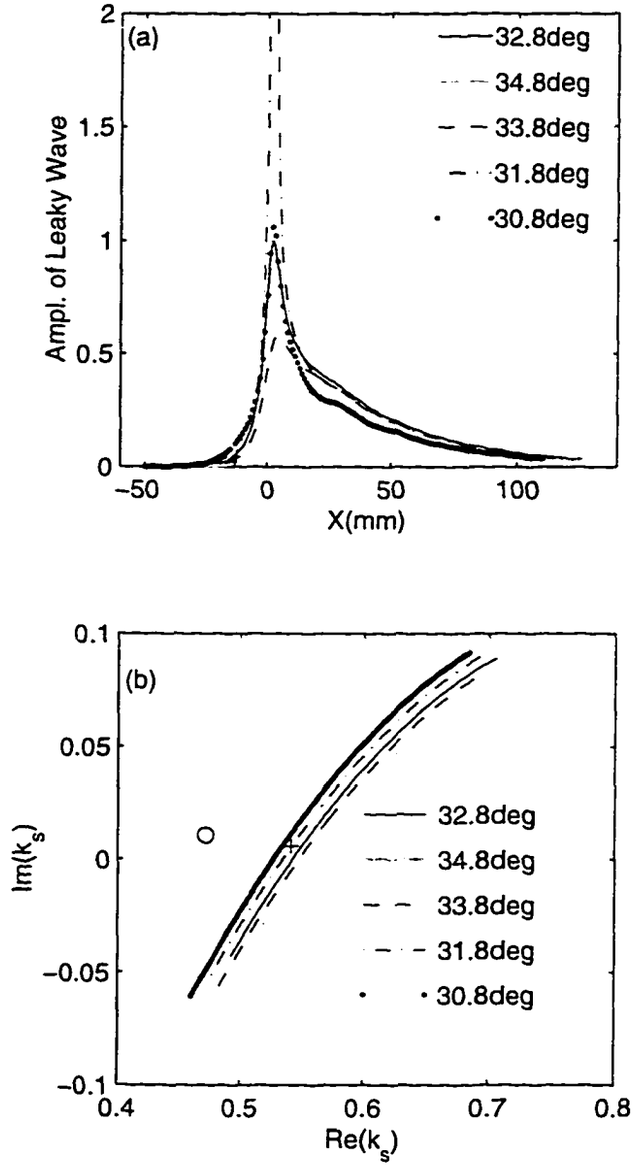

Figure B.2 (a) The calculated amplitude of leaky wave part of the receiver voltage as a function of scan distance on a steel plate when $\mathcal{R}$ is aligned: $\theta_{\mathcal{R}} = \theta_{\mathcal{T}} = 32.8°$, and when it is misaligned: $32.8° \pm 1°$, and $32.8° \pm 2°$. For all plots, $\theta_{\mathcal{T}} = 32.8°$. (b) The corresponding saddle point loci of different cases in (a) and the relative position of A_0 pole (plus sign) and S_0 pole (open circle).

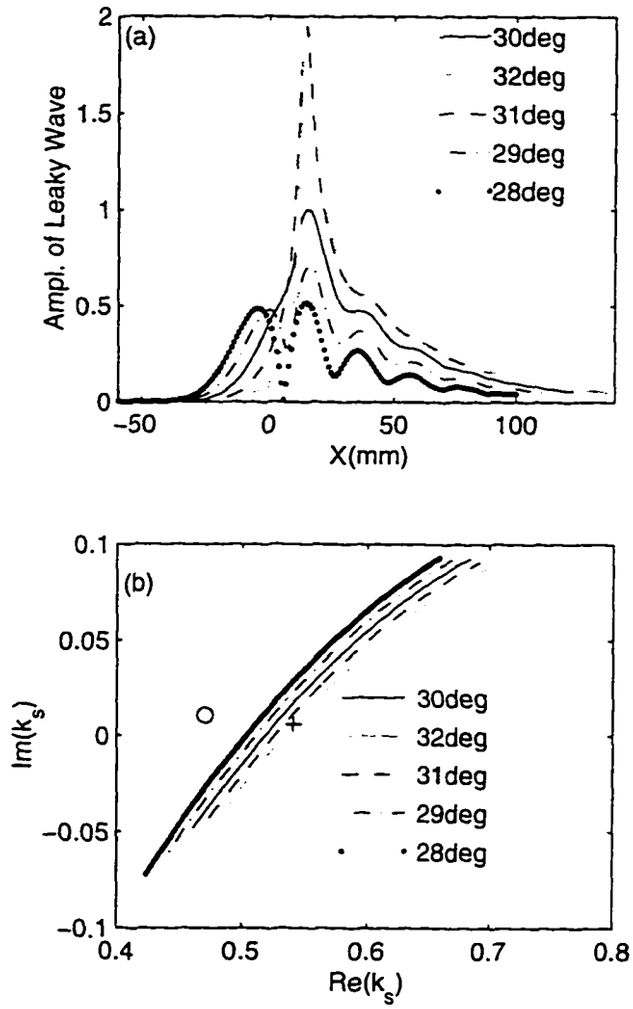

Figure B.3 (a)The calculated amplitude of leaky wave part of the receiver voltage as a function of scan distance on a steel plate when $\mathcal{R}$ is aligned: $\theta_{\mathcal{R}} = \theta_{\mathcal{T}} = 30°$, and when it is misaligned: $30° \pm 1°$, and $30° \pm 2°$. For all plots, $\theta_{\mathcal{T}} = 30°$.(b) the corresponding saddle point path of different cases in (a) and the relative position of A_0 pole (plus sign) and S_0 pole (open circle).

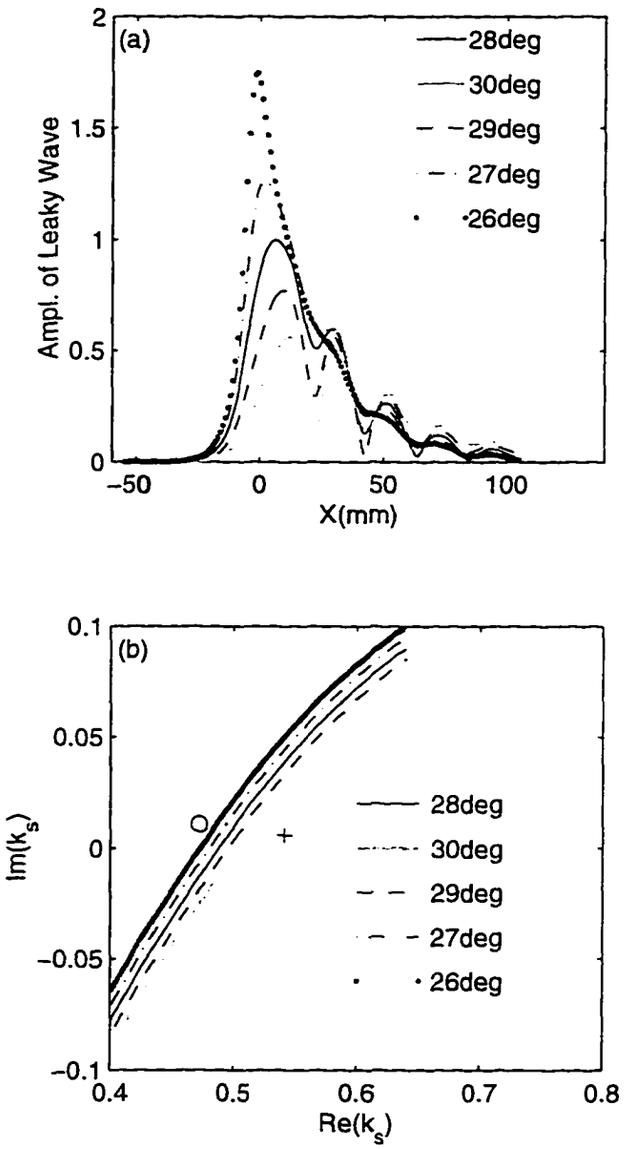

Figure B.4 (a)The calculated amplitude of leaky wave part of the receiver voltage as a function of scan distance on a steel plate when $\mathcal{R}$ is aligned: $\theta_{\mathcal{R}} = \theta_{\mathcal{T}} = 28°$, and when it is misaligned: $28° \pm 1°$, and $28° \pm 2°$. For all plots, $\theta_{\mathcal{T}} = 28°$. (b) the corresponding saddle point path of different cases in (a) and the relative position of A_0 pole (plus sign) and S_0 pole (open circle).

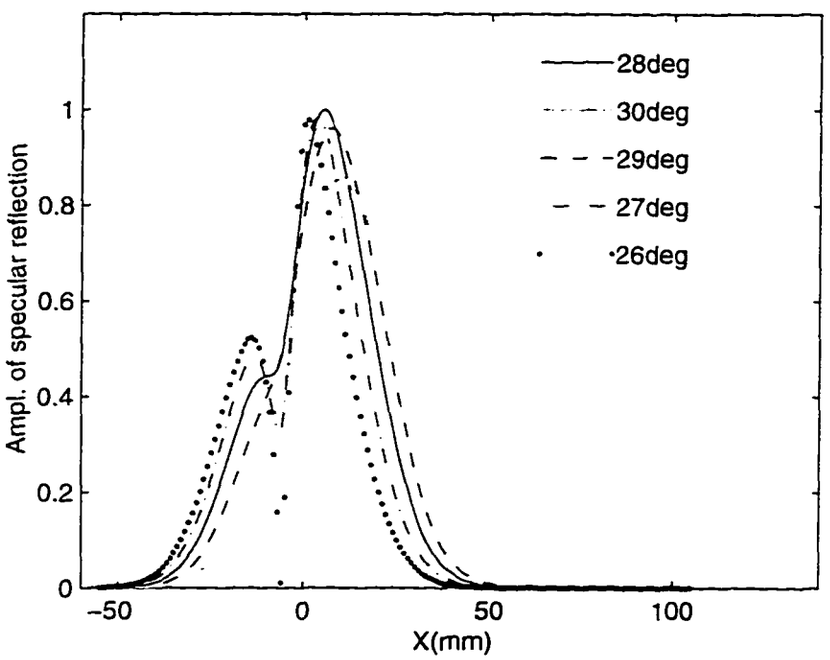

Figure B.5 The calculated amplitude of the specular part of the receiver voltage as a function of scan distance on a steel plate when $\mathcal{R}$ is aligned: $\theta_{\mathcal{R}} = \theta_{\mathcal{T}} = 28°$, and when it is misaligned: $28° \pm 1°$, and $28° \pm 2°$. For all plots, $\theta_{\mathcal{T}} = 28°$.

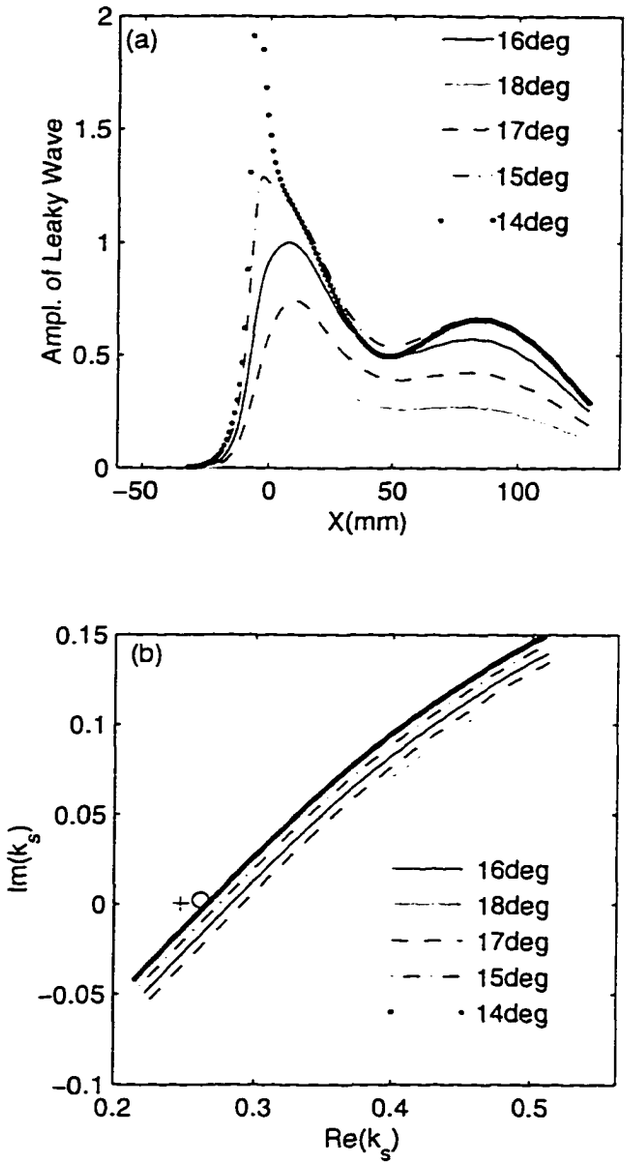

Figure B.6 (a)The calculated amplitude of leaky wave part of the receiver voltage as a function of scan distance on steel plate when $\mathcal{R}$ is aligned: $\theta_{\mathcal{R}} = \theta_{\mathcal{T}} = 16°$, and when it is misaligned: $16° \pm 1°$, and $16° \pm 2°$. For all plots, $\theta_{\mathcal{T}} = 16°$.(b) The corresponding saddle point path of different cases in (a) and the S_1 pole (plus sign) and A_1 pole (open circle).

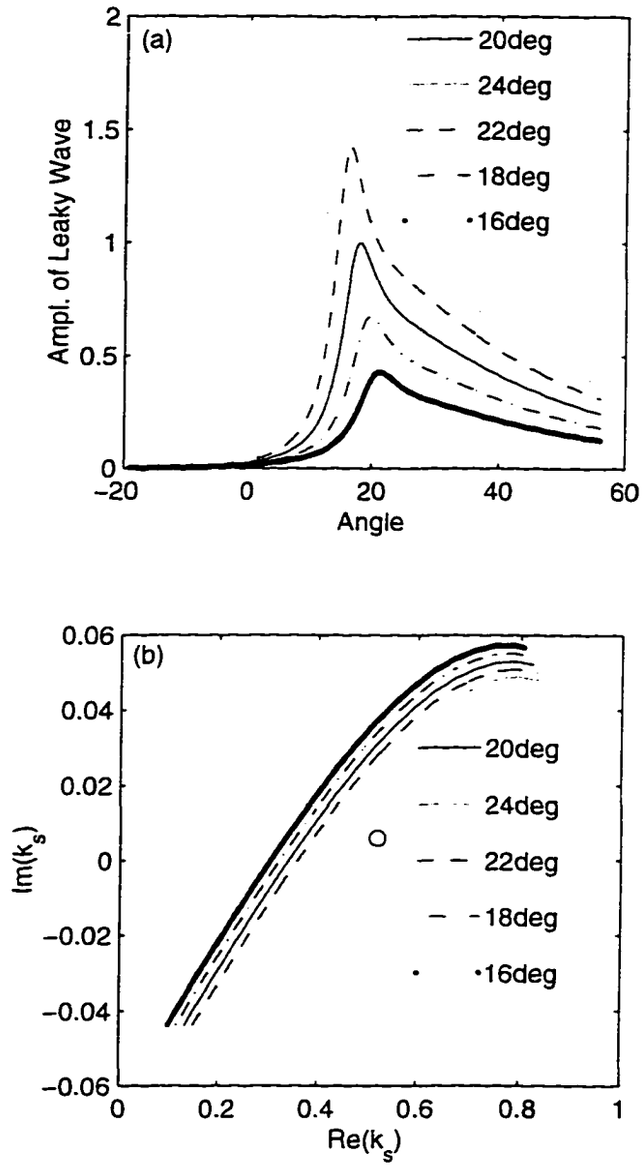

Figure B.7 (a)The calculated amplitude of leaky wave as a function of scan angle on steel cylinder when $\mathcal{R}$ is aligned: $\theta_{\mathcal{R}} = \theta_{\mathcal{T}} = 20°$. and when it is misaligned: $20° \pm 2°$. and $20° \pm 4°$. For all plots. $\theta_{\mathcal{T}} = 20°$. (b) the corresponding saddle point path of different cases in (a) and the relative position of Rayleigh pole (open circle).

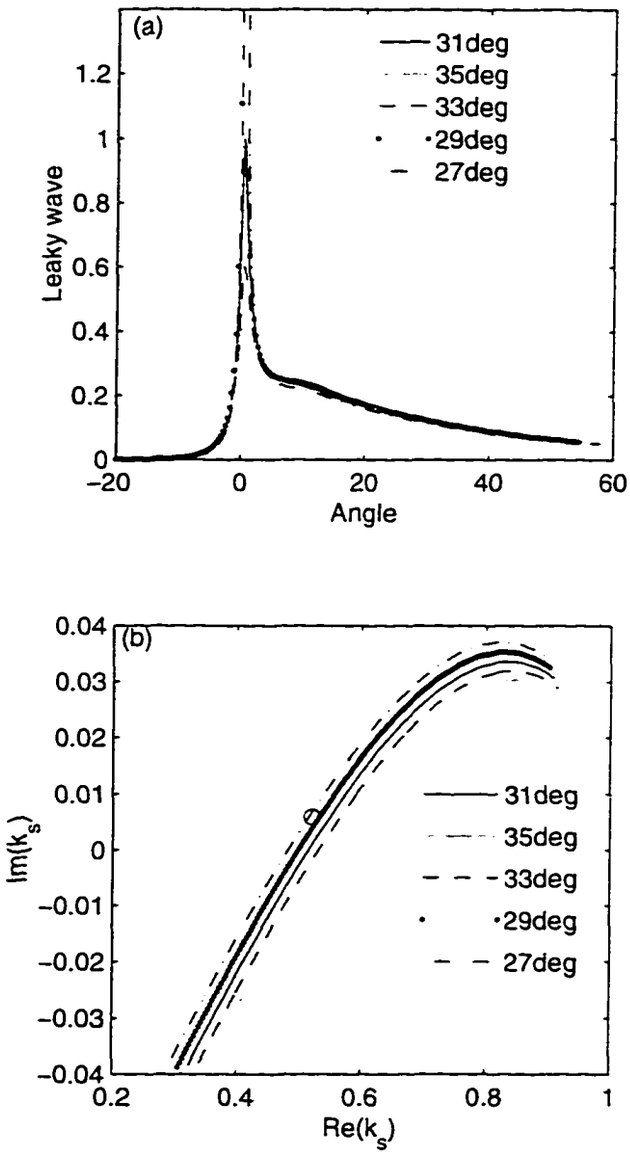

Figure B.8 (a)The calculated amplitude of leaky wave as a function of scan angle on steel cylinder when $\mathcal{R}$ is aligned: $\theta_{\mathcal{R}} = \theta_{\mathcal{T}} = 31°$, and when it is misaligned: $31° \pm 2°$, and $31° \pm 4°$. For all plots, $\theta_{\mathcal{T}} = 31°$. (b) the corresponding saddle point path of different cases in (a) and the relative position of Rayleigh pole (open circle).

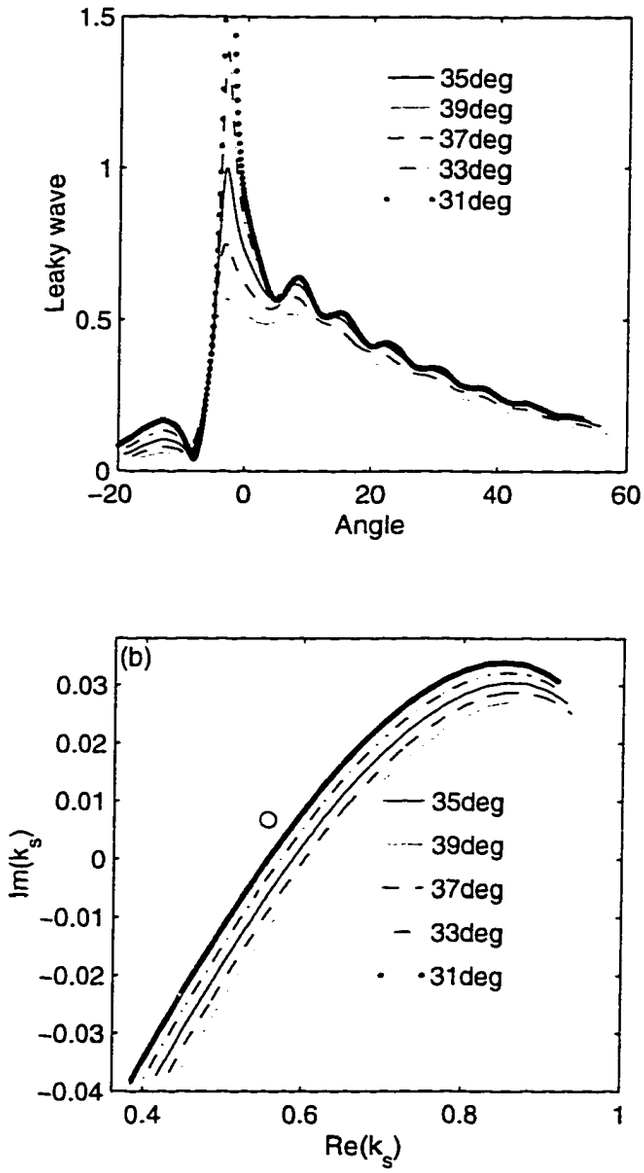

Figure B.9 (a)The calculated amplitude of leaky wave part of the receiver voltage as a function of scan angle on steel shell when $\mathcal{R}$ is aligned: $\theta_{\mathcal{R}} = \theta_{\mathcal{T}} = 35°$. and when it is misaligned: $35° \pm 2°$. and $35° \pm 4°$. For all plots. $\theta_{\mathcal{T}} = 35°$. (b) the corresponding saddle point path of different cases in (a) and the relative position of A_0 pole (open circle).

ACKNOWLEDGMENTS

First I would like to express my most sincere appreciation to my advisor, Dr. Chimenti for his continuous support during my Ph.D. his guidance, encouragement, patience and broad knowledge in this field are the most significant factor for the completion of the dissertation. Without him, this work would be impossible. He leads me to my professional career from a student.

I would like to thank Dr. Rizzo, Dr. Schmerr and Dr. Lord and Dr. Udpa for serving as my committee member and for supporting and advising me on my research.

Special thanks go to Dr. Zeroug for his willingness to share with me his knowledge and a lot of stimulating discussion on complex transducer point Special thanks also go to Dr. Lobkis for his offering help on wave theory and experiment implementation. In the early stage of my Ph.D study Mr. Kettenacker and Mr. Cloutier gave me a good introduction about the experiments in the ultrasonics labs of Center for Nondestructive Evaluation.

I would like to extend my thank to the faculty and staff in AEEM department and CNDE who have frequently and freely offered their help, especially Dr. D. Hsu. For the use of Panametrics scan system, I would like to thank Mr. S. Swormly, Dr. Ron Roberts and his students.

At this memont I remember all my teachers from elementary school to graduate college, I want to thank them for passing their knowledge and wisdom to me while expecting nothing in return.

At last I would like to tha my parents, who support and encourage me to attain

my academic goal for decades . and my wife. xiaoqiong. who sacrificed a lot of time to support me while pursuing her own study.